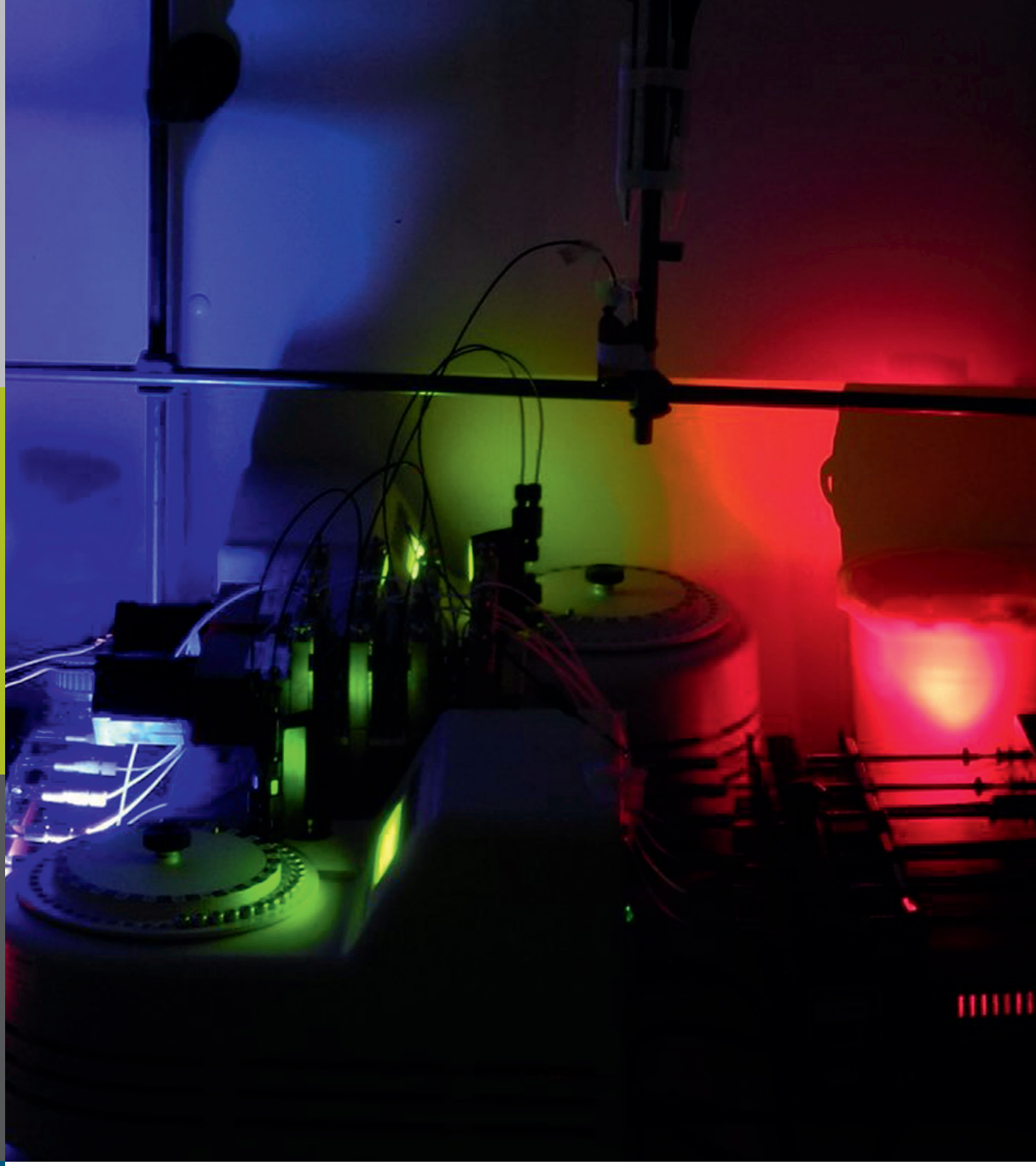

# Development and Characterization of a Microfluidic Magnetic Oscillation Reactor for Enzymes

Daniel Jussen

JÜLICH
FORSCHUNGSZENTRUM

Member of the Helmholtz Association

Schriften des Forschungszentrums Jülich
Reihe Schlüsseltechnologien / Key Technologies Band / Volume 86

Forschungszentrum Jülich GmbH
Institut für Bio- und Geowissenschaften
Biotechnologie (IBG-1)

# Development and Characterization of a Microfluidic Magnetic Oscillation Reactor for Enzymes

Daniel Jussen

Schriften des Forschungszentrums Jülich
Reihe Schlüsseltechnologien / Key Technologies Band / Volume 86

ISSN 1866-1807 ISBN 978-3-89336-974-4

Bibliographic information published by the Deutsche Nationalbibliothek.
The Deutsche Nationalbibliothek lists this publication in the Deutsche Nationalbibliografie; detailed bibliographic data are available in the Internet at http://dnb.d-nb.de.

| | |
|---|---|
| Publisher and Distributor: | Forschungszentrum Jülich GmbH<br>Zentralbibliothek<br>52425 Jülich<br>Tel: +49 2461 61-5368<br>Fax: +49 2461 61-6103<br>Email: zb-publikation@fz-juelich.de<br>www.fz-juelich.de/zb |
| Cover Design: | Grafische Medien, Forschungszentrum Jülich GmbH |
| Printer: | Grafische Medien, Forschungszentrum Jülich GmbH |
| Copyright: | Forschungszentrum Jülich 2014 |

Schriften des Forschungszentrums Jülich
Reihe Schlüsseltechnologien / Key Technologies, Band / Volume 86

D 82 (Diss. RWTH Aachen University, 2014)

ISSN 1866-1807
ISBN 978-3-89336-974-4

The complete volume is freely available on the Internet on the Jülicher Open Access Server (JUWEL) at www.fz-juelich.de/zb/juwel

“*A live donkey is better than a dead lion, isn't it?"*

Sir Ernest Shackleton (1874 - 1922) after turning back from his South Pole expedition at 88° 23′ S even though he was only 112 miles (180 km) away from the Pole.

## Abstract

Process development poses one of the main bottlenecks during development of biocatalytic processes for fine and bulk chemicals. Therefore novel tools to decrease the cost of process development have come into the focus of interest. While modelling and small scale liquid handling in multi well based platforms are already employed, there is still a lack of continuous microfluidic reaction systems for enzyme process development. In this thesis the magnetic oscillation reactor for enzymes (μMORE), a novel continuous microfluidic reactor concept for process optimization has been developed. The system is mixed by magnetic beads, on which the enzyme is immobilized, by utilization of an oscillating magnetic field. The concept has been designed to allow for simple parallelization of multiple reactors. A six-fold enzyme microreactor system was constructed. The novel reactor system was developed, characterized and finally tested with benzoylformate decarboxylase from *Pseudomonas putida.* This enzyme catalyzes the carboligation of benzaldehyde and acetaldehyde to (*S*)-2-hydroxypropiophenone. The results indicate that the system provides a useful tool for enzyme process optimization, generating process parameters that are useful for scale up of the process from micro- to bench scale.

## Kurzfassung

Die Prozessentwicklung stellt einen der Hauptengpässe bei der Entwicklung von biokatalytischen Prozessen zur Erzeugung von Bulk- und Feinchemikalien dar. Aus diesem Grund sind neue Werkzeuge zur Beschleunigung der Prozessentwicklung und zur Reduzierung der Kosten in den Blickpunkt des Interesses gerückt. Während rechnergestützte Simulationen und das Handling von Kleinstvolumina in Mikrotiterplatten-basierten Plattformen bereits verwendet werden, besteht weiterhin ein Mangel an kontinuierlichen mikrofluidischen Reaktionssystemen für die Prozessentwicklung. In dieser Arbeit wurde der Mikrofluidische Magnetische Oszillationsreaktor (μMORE), ein neues mikrofluidisches Reaktionssystem für die Prozessoptimierung, entwickelt. Der Reaktionsraum wird durch magnetische Partikel, auf denen das Enzym immobilisiert ist, durch Verwendung eines oszillierenden magnetischen Feldes durchmischt. Das Konzept wurde so entwickelt, dass es eine einfache Parallelisierung von mehreren Reaktoren erlaubt. Ein sechsfach Reaktionssystem wurde konstruiert. Das neue Reaktorsystem wurde entwickelt, charakterisiert und abschließend mit der Benzoylformiatdecarboxylase aus *Pseudomonas putida* getestet. Dieses Enzym katalysiert die Carboligation von Benzaldehyd und Acetaldehyd zu (*S*)-2-Hydroxypropiophenon. Die Resultate weisen darauf hin, dass das System ein nützliches Werkzeug für die Enzymprozessoptimierung darstellt und dass die gewonnenen Prozessparameter die Maßstabsvergrößerung vom Mikro- in den Labormaßstab ermöglichen..

# List of Publications

## Patents

Jussen D., Pohl M. Mikro-Makroverbindungen für mikrofluidische Systeme sowie Verwendung einer elektrischen Leckdetektionsvorrichtung. Aktenzeichen 10 2013 009 970.6. Deutsches Patent und Markenamt (angemeldet).

Jussen D., Pohl M. Vorrichtung zum Mischen von Flüssigkeiten in einem Mikrokanal. Aktenzeichen 10 2013 006 235.7. Deutsches Patent und Markenamt (angemeldet).

## Conference contributions

Jussen D., Wiechert W., Pohl. M. Development of a novel microbioreactor concept for enzymatic carboligation. EMBL Conference on Microfluidics, Heidelberg 25.-27.7.2012.

Jussen D., Valinger D. Wiechert W., Pohl. M. Entwicklung eines neuen Mikroreaktor-Konzepts für die enzymatische Carboligation. DECHEMA-Jahrestagung der Biotechnologen und ProcessNet-Jahrestagung 2012, Kongresszentrum, Karlsruhe 10. - 13.09.2012.

Jussen D., Wiechert W., Pohl. M. Establishing a novel microbioreactor concept for enzymatic carboligation. IMTB 2013; Cavtat, Croatia; 05.08.05.2013

Jussen D., Wiechert W., Pohl. M. Micro magnetic oscillation reactor for enzymes (µMORE) Biotrans 2013; Manchester, United Kingdom; 21.-25 .07.2013

## Acknowledgements

First of all I would like to thank Prof. Dr. Wolfgang Wiechert for the great opportunity to do my doctoral thesis in his institute as well as for supervising my thesis and providing an amazing degree of freedom for me to shape the project. Furthermore my special thanks goes to Prof. Dr. Martina Pohl, not only for the supervision of my thesis but also for her amazing encouragement, her great advice, and many fruitful discussions as well as for her support while adapting the project according to my own ideas and providing the freedom necessary to do so. I also thank Prof. Dr. Antje Spieß being my coreferent and for her crucial input from an engineering point of view and Dr. Dörte Rother for many interesting ideas and providing great input and motivation.

My thanks go to Ursula Mackfeld for her great help while doing the carboligation experiments. I especially appreciated her creativity and many good ideas while working together and her dedication of continuing the last experiments while I had already started writing this thesis. Heike Offermann also deserves a huge thank you, especially for getting all the unusual items I ordered; all except one. I additionally thank Anke Kaiser, who carried out the immobilization experiments in her master thesis.

I thank Dr. Helmut Soltner form ZEA at the Forschungszentrum Jülich for his aid in designing the magnetic agitation setup and providing the magnetic field simulations as well as a great deal of input concerning magnetic field theory. Furthermore I thank Eric van Lieres and Birgit Stute for carrying out the CFD simulations as well as Eric von Lieres and Lars Freier for their input on Kriging-based process optimization (data not presented).

Furthermore, my thanks goes to Mario Fricke and Hubert Ruhrig of the IBG-1 workshop for their patience with my endless series of optimizations and for doing an amazing job building the reactor I had envisioned in my mind. As far as reactor building and implementation goes, I additionally thank Andra Rübsteck and Andreas Franz for the Labview controls of the reactor system, and Jürgen Paulzen for the electronics setup. My thanks also go to Christian Munier from University Bielefeld for his help to debug my python scripts.

I also would like to thank my amazing colleagues, Daniel Minör, Roland Moussa, Daniel Okrob, Tina Gerhards, Justyna Kulig, Alvaro Baraibar, Robert Westphal, Torsten Sehl, Victoria Steffen, Ashaira Brahma, Vanessa Erdmann, and Anna Baierl as well as our numerous students! Without them and the great working environment as well as uncountable fruitful scientific and non-scientific discussion this thesis would have been impossible! Without them the "Jülich, it has everything… Once!"[1] would not have been endurable. I especially thank office 305 for enduring my countless coffee stops to keep my caffeine level constant and Roland Moussa for getting our first decent workgroup coffee maker. My distinguished thanks also go to Torsten Sehl for always asking the most interesting questions possible and pointing out any flaw of my designs, thus driving me forward at all times! Furthermore, I thank our micro scale engineering workgroup Alexander Grünberger, Christopher Probst, Christina Krämer, and Dr. Dietrich Kohlheyer for getting me started on microfluidics and helping me numerous times with advice and input. Additionally I thank Prof Dr. Durda Vasic Racki, Dr. Zvezdana Frindik, Davor Valinger, Anita Salic, Anna Tuzek, and Martina Sudar of my "second workgroup" from the Faculty of Chemical Engineering (FKIT), University Zagreb, for their great help getting acquainted with enzymes in microfluidics as well as their amazing hospitality during my two months at their laboratories.

Last but not least I thank my family for their constant support during 24 years of education, as well as my friends in and from Bielefeld for their great hospitality whenever Jülich "It has everything… once!" drove me away and the amazing holidays I spend with them whenever I had to refuel my batteries during the last three years!

[1] Original citation of one colleague during my job interview in Jülich

## Table of content

## List of abbreviations

| | |
|---|---|
| ABS | acrylnitrile-butadien-styrene-copolymerisate |
| ACS | American Chemical Society |
| BAL | benzaldehyde lyase from *Pseudomonas fluorescence* |
| BFD | benzoylformate decarboxylase from *Pseudomonas putida* |
| BSA | bovine serum albumin |
| BSTR | batch stirred tank reactor |
| CFD | computational flow dynamics |
| CFPR | continuous Plug flow reactor |
| CLEA | cross-linked enzyme aggregate |
| CLEC | cross-linked enzyme crystal |
| CSTR | continuous stirred tank reactor |
| FEB | fluorethylenepropylene |
| FFKM | Perflourelastomer |
| GCI | Green Chemistry Institute |
| HI-ADH | horse liver alcohol dehydrogenase |
| HPLC | High performance liquid chromatography |
| HPP | 2-hydroxypropiophenon |
| IER | immobilized enzyme reactor |
| IMAC | immobilized metal ion affinity chromatography |
| Kpi | potassium phosphate |
| NADH | nicotinamide adenine dinucleotide |
| NTA | nitrilotriacetic acid |

| | |
|---|---|
| PDC | pyruvate decarboxylase from *Acetobacter pasteurianus* |
| PAC | phenylacetylcarbinol |
| Re | Reynolds number |
| RGB | red green blue |
| SEC | size exclusion chromatography |
| SIBC | Swiss Industrial Biocatalysis Consortium |
| PTFE | polytetrafluoroethylene |
| PEEK | polyether ether ketone |
| STY | space time yield |
| ThDP | thiamine diphosphate |
| µMORE | mircrofluidic magnetic oscillation reactor for enzymes |

# List of units and prefixes

## Units

| | |
|---|---|
| A | ampere |
| h | hours |
| g | gram |
| M | molar (mol $L^{-1}$) |
| m | meter |
| mol | mole |
| N | newton (kg m $^{s-2}$) |
| s | seconds |
| T | tesla ($kg \cdot s^{-2} \cdot A^{-1}$) |
| U | Units of enzyme activity (µM $min^{-1}$) |

## Prefixes

| | |
|---|---|
| k | kilo ($10^3$) |
| d | deci ($10^{-1}$) |
| c | centi ($10^{-2}$) |
| m | milli ($10^{-3}$) |
| µ | micro ($10^{-6}$) |
| n | nano ($10^{-9}$) |

## List of symbols

| | | |
|---|---|---|
| $A_0$ | U | initial activity |
| $A_t$ | U | activity at a defined time point, |
| $(\vec{B})$ | T | magnetic flux density |
| *c* | M $L^{-1}$/g $L^{-1}$ | solute concentration |
| *D* | $m^2$ $s^{-1}$ | diffusion coefficient |
| *ee* | % | enantiomeric excess |
| F | N | force |
| $F_w$ | N | flow resistance |
| $k_{des}$ | $h^{-1}$ | inactivation constant |
| *l* | m | characteristic length, |
| M | kg $M^{-1}$ | molar mass |
| $(\vec{M})$ | A $m^{-1}$ | magnetization |
| m | kg | mass |
| $(\vec{m})$ | A $m^2$ | magnetic moment |
| n | M | amount of solute |
| $n_0$ | M | initial amount of solute |
| *r* | m | radius of the sphere |
| Re | | Reynolds number |
| t | h | time |
| $t_{1/2}$ | h | half-life |
| τ | h | residence time |
| *u* | m $h^{-1}$ | flow velocity |

| | | |
|---|---|---|
| $v$ | $M\ h^{-1}$ | reaction rate |
| $\eta$ | $m^2\ s^{-1}$ | dynamic viscosity |
| $\rho$ | $kg\ m^{-3}$ | density |
| $\mu$ | $N\ A^{-2}$ | magnetic permeability |
| $\mu_0$ | $N\ A^{-2}$ | magnetic permeability in vacuum |
| $\mu_r$ | | magnetic permeability relative to vacuum |
| $\nu$ | $kg\ m^{-1}\ s^{-1}$ | kinematic viscosity |

## List of figures

## List of tables

# 1 Introduction

## 1.1 Biocatalysis

Biocatalysis describes the utilization of naturally occurring catalysts such as enzymes, for chemical synthesis. These biocatalysts may be used in purified form or as whole cells. First references of biocatalytic processes date back to ancient Egypt, as archaeological studies revealed that bread and beer, both yeast fermentation products, formed major parts of the nutrition of the pyramid workers (David, 2002). However, only the scientific advances of the last two centuries allowed for specific development of today's wide range of biocatalytic processes. Starting with the discovery of enzymes by Buchner in 1897 (Buchner and Rapp, 1897) milestones in biotechnology such as the discovery of protein crystallography (Sumner, 1926), the chemical structure of DNA (Watson and Crick, 1953), and polymerase chain reaction (Mullis, 1985) as well as novel cell- and bacteria cultivation technology, purification-, and analytical methods provided the tools necessary to apply biocatalysis not only for the fermentation of crude nutritional products but also for fine and bulk chemicals and complex processes. By now over 500 products are produced using enzymes and about 150 industrial processes use enzymes or whole cell biocatalysis (Adrio and Demain, 2014). Biocatalysts and biocatalytically produced products have become a part of everyday life in washing detergents, starch, pulp and paper, leather, personal care, and detergents industries as well as food processing and animal food supplements (Johannes and Zhao, 2006). In pharmaceutical industry the use of biocatalysts is well established and it becomes more and more interesting also for bulk chemicals further down the value chain (Woodley et al., 2013). However, the major hurdles for the development of novel biocatalytic processes are still the high costs of biocatalysts for industrial production and slow market introduction of novel technologies into the industry (Lima-Ramos et al., 2013). Despite the dominance of chemical synthesis, the last fifteen years with their advances in molecular genetics, protein structure analysis- and simulation allowed for *in vitro* evolution and targeted modification of enzymes making them more attractive as an alternative to chemical methods (Lima-Ramos et al., 2013). These

improved biocatalysts theoretically allow for a wide range of optimization and adaptation of a given biocatalyst, not only for adaptation of its substrate spectrum but also for process stability, and optimal chemo- and stereoselectivity (Bornscheuer et al., 2012). Recent literature proves that biocatalysis is not only able to produce molecules such as (*S*)-phenypropionylcarbinol that was not accessible by chemical synthesis in highly chemo- and stereoselectively purity (Baraibar et al., 2013) but also that pharmaceutically interesting molecules such as nor(pseudo)ephedrine can be produced in high enantiomeric excess, concomitant by a drastic reduction of the number of synthetic steps (Sehl et al., 2013).

These advances in combination with the environmentally friendly use of mild reaction conditions in biocatalysis as well as the versatility of application and the development of enzymatic or chemo-enzymatic multistep cascades (Clouthier and Pelletier, 2012) make biocatalysis one of the key technologies for green chemistry. The American Chemical Society (ACS), the Green Chemistry Institute (GCI), and several global pharmaceutical corporations founded the ACS GCI Pharmaceutical Roundtable in 2005. The motivation for this institution is not only to reduce process costs but also the awareness of increasing sustainability of manufacturing processes (Jiménez-González et al., 2011). A brainstorming prioritization of this roundtable identified continuous processing and bioprocesses as the two prior research areas (Jiménez-González et al., 2011). One of the great challenges in introducing novel biocatalytic processes into industrial application is the high cost and long development time of processes, as a close investigation of a given biocatalyst, its variants and the process parameters are crucial for industrial process development (Lima-Ramos et al., 2013). Therefore the Swiss Industrial Biocatalysis Consortium (SIBC) was founded in 2004 to overcome the limitations of biocatalysis for industrial application. Besides ready to use enzyme libraries, including all classes of enzymes and new cooperation models between academia and industry they suggest the development of technologies for rapid scale up (Meyer et al., 2013). Novel screening methods and the capabilities of small volume reaction systems offer a cheap and versatile solution for this bottleneck in process development (Pollard and Woodley, 2007).

## 1.2 Synthesis of α-Hydroxy ketones

α-Hydroxy ketones serve as valuable building blocks for the pharmaceutical industry (Hoyos et al., 2010). Many different biologically active compounds contain this building block. They include antidepressants such as bupropion and 1555U88 (Fang et al., 2000), but also amyloid-β-protein inhibitors used in Alzheimer's treatment as well as farnesyl transferase inhibitors (Kurasoin A and B) and antifungal agents such as the fungicide Ro09-3355 (Adam et al., 1999; Hoyos et al., 2010; Tanaka et al., 2004; Wallace et al., 2003).

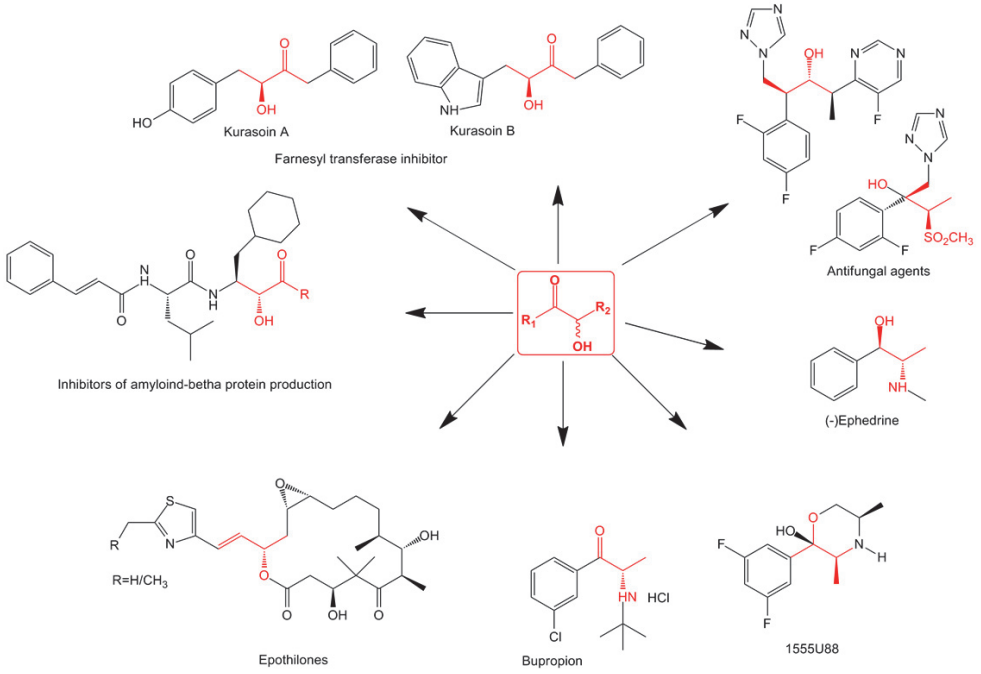


**Figure 1: Biologically active compounds derived from α-hydroxy ketones (Hoyos et al., 2010).**

Due to its value as a chemical precursor numerous chemical and enzyme catalyzed strategies for the access of complex α-hydroxy ketones have been investigated (Hoyos et al., 2010). Synthetic chemical approaches such as α-hydroxylation of ketones, the Sharpless asymmetric dihydroxylation of the silylenol ether of the corresponding ketone, the ketohydroxylation of olefins, the oxidative kinetic resolution of racemic α-hydroxy ketones and some organocatalytic approaches are often limited by their low enantionselectivity and large number of synthetic steps (Hoyos et al., 2010). Therefore biocatalytic approaches for the synthesis of α-

hydroxy ketones provide a valuable alternative. Different enzymatic approaches have been published (Figure 2).

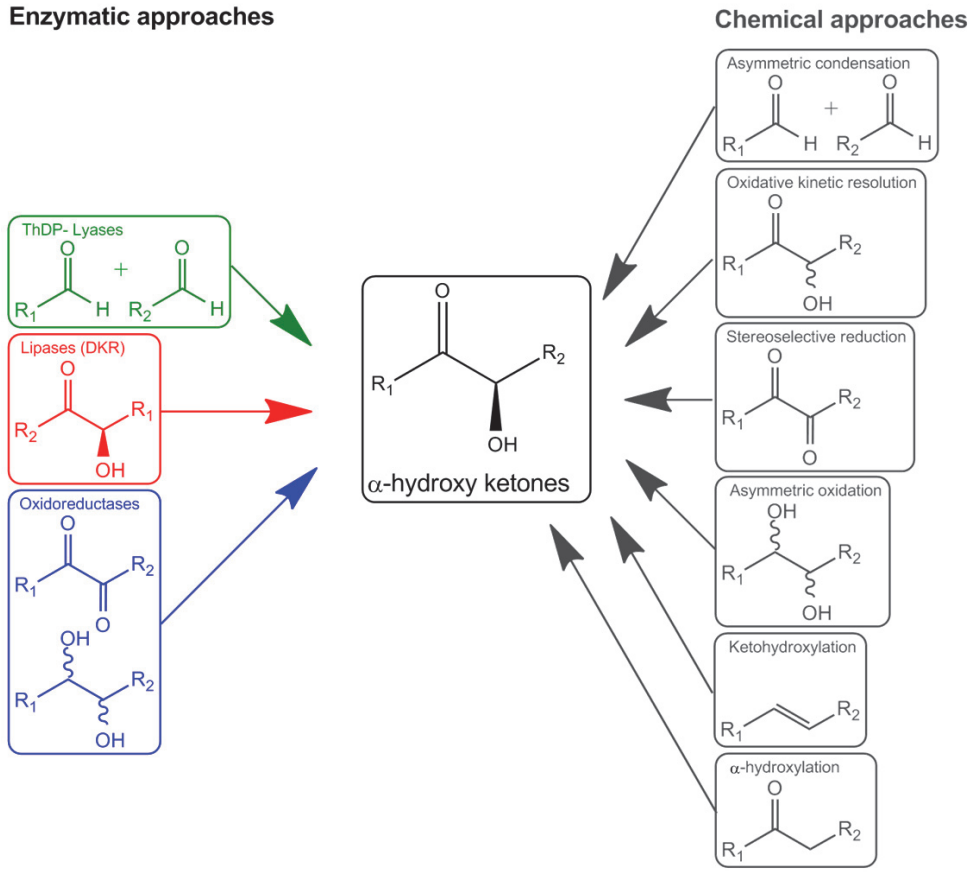


**Figure 2: Strategies for the synthesis of α-hydroxy ketones. Left**: enzymatic approaches: ThDP-dependent lyases, lipases (dynamic kinetic resolutions (DKR)) and oxidoreductases **right**: Chemical strategies: Asymmetric condensation, stereoselective reduction, asymmetric oxidation, ketohydroxylation and alpha-hydroxylation (Hoyos et al., 2010).

Among these, the carboligation of cheap aldehydes using ThDP-dependent enzymes is a promising approach to access a multitude of α-hydroxy ketones with high yields and high enantioselectivity (Gocke et al., 2008). Therefore a toolbox of ThDP-dependent enzymes was created (Gocke, 2010). During the last years this toolbox was continuously extended by novel wild-type enzymes as well as variants of already known enzymes, thus expanding the product range to a vast number of

substituted aliphatic, aromatic, and araliphatic α-hydroxy ketones (Müller et al., 2013).

The carboligation of benzaldehyde and acetaldehyde catalyzed by ThDP-dependent enzymes is exemplarily depicted in figure 3. This reaction was used as a model reaction in of this thesis.

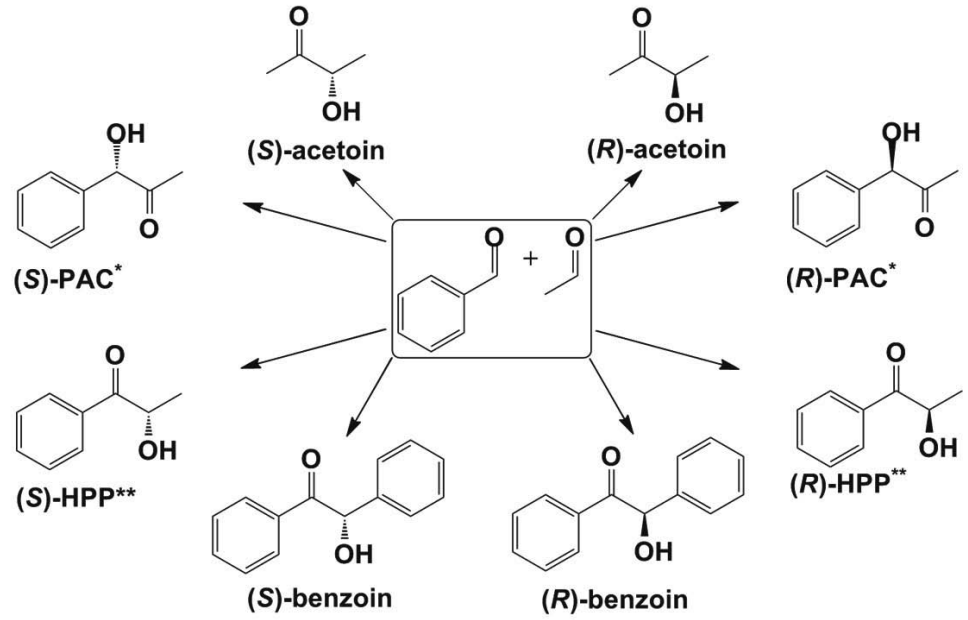


**Figure 3: Possible products of the stereoselective carboligation of benzaldehyde and acetaldehyde.**

## 1.3 ThDP-dependent enzymes

Cofactors are molecules needed for several enzymes to develop their specific enzymatic activities (IUPAC, 2014). The enzyme used in this thesis uses thiamine diphosphate (ThDP) as a cofactor, which is the biologically active form of thiamine (vitamin B1) (Hübner et al., 1998). While vitamin B1 can be synthesized by plants, it is an essential vitamin for animals and humans. Vitamin B1 deficiency causes polyneuritis (beriberi in humans) (Gangolf et al., 2010). ThDP is composed of a

pyrimidine ring and a thiazolium ring and carries a diphosphate group allowing the molecule to bind to the enzyme. In ThDP-dependent enzymes a magnesium ion complexes the cofactor within the catalytic center which was verified first for the pyruvate oxidase from *Lactobacillus plantarum* (Muller and Schulz, 1993) .

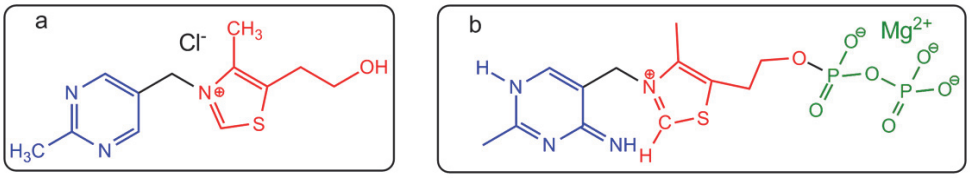


**Figure 4: Structure of thiamine (vitamin B1) (a) and its biologically active form thiamine diphosphate (b). Blue: pyrimidine ring, black: methyl bridge; red: thiazolium ring; green: diphosphate group**.

Today a broad spectrum of ThDP-dependent enzymes has been identified, including dehydrogenases, transketolases, oxidases, oxidoreductases, and lyases. These enzymes are found in numerous organisms and are involved in a multitude of different metabolic pathways (Bunik et al., 2013).

Interestingly there is a strong similarity in the tertiary structure of ThDP-dependent decarboxylases active sites. The two domains involved in ThDP-binding are highly conserved throughout all ThDP- dependent decarboxylases (Pohl et al., 2009). The conserved structure within ThDP-dependent enzymes includes three domains for each monomer, the pyrimidine binding domain (α), the pyrophosphate binding domain (β) and an additional domain (γ). As two active sites are formed at the contact interface of two monomers the dimer is the minimal catalytic subunit of these enzymes (Pohl et al., 2009).

### 1.3.1 General reaction mechanism

All ThDP-dependent enzymes share a similar reaction mechanism, despite their differences in substrate range and reaction spectrum. This mechanism is explained exemplarily for the cleavage and formation of C-C bonds. The first step of the reaction is the activation of the catalytic center, the acidic C2 atom of the thiazolium ring, by deprotonation resulting in a nucleophilic ylide (Breslow, 1957). In all known structures of ThDP-dependent enzymes the cofactor is bound in a typical V-conformation which brings the C2 atom of the thiazolium ring in reactive distance to

the 4-imino group of the pyrimidine ring (Figure 5). This 4-imino group can then deprotonate the C2-position, supported by a conserved glutamate residue (Frank et al., 2007; Hübner et al., 1998; Jordan, 2003; Polovnikova et al., 2003). The resulting C2-ylide may then attack electrophilic groups of aldehydes or α-ketoacids. The first substrate, called the donor substrate, is thereby covalently bound to the C2 atom of ThDP. The formed tetrahedral adduct is stabilized either by deprotonation (in case of an aldehyde) or by decarboxylation (in case of a ketoacid) yielding a resonance-stabilized carbanion-enamine. This common intermediate, known as “Breslow intermediate” or “active aldehyde”, now has nucleophilic activity at the former carbon atom of carbonyl group (Krampitz and Greull, 1958). Finally the carbanion-enamine can be protonated, which results in aldehyde release. Alternatively it can react with an acceptor substrate i.e. an aldehyde to form an α-hydroxy ketone.

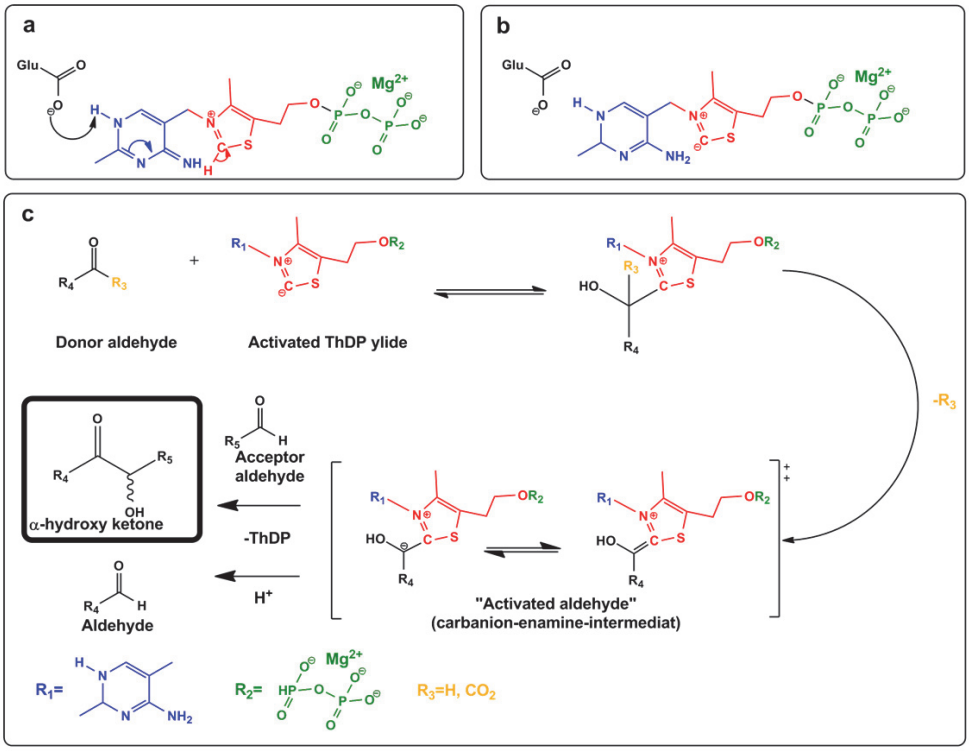


**Figure 5: General mechanism of ThDP-dependent enzymes. a. enzyme bound ThDP molecule; b:** activated ThDP ylide **c:** Catalytic cycle: Formation of the "active aldehyde" by binding of a donor substrate to the ThDP ylide and subsequent deprotonation/decarboxylation. Protonation of the carbanion-enamine results in release of an aldehyde, whereas reaction with a further aldehyde molecule (acceptor) yields an α-hydroxy ketone (box).

### 1.3.2 Chemo and stereoselectivity of ThDP-dependent enzymes

While mechanism and cofactor binding are conserved in all ThDP-dependent enzymes, the substrate spectrum as well as the chemo- and stereoselectivity of different enzymes can vary greatly (Müller et al., 2009; Sprenger and Pohl, 1999). While the chemoselectivity is determined by the order of the substrate binding (Dünkelmann et al., 2002), the stereoselectivity is controlled by the relative orientation of donor and acceptor prior to C-C-bond formation (Knoll et al., 2006). Extensive investigation of ThDP-dependent enzymes and their active sites has shown that the conformation of the active site directly influences not only the

substrate spectrum but also the stereoselectivity (Pohl et al., 2009; Gocke et al., 2009). Using the carboligation of benzaldehyde and acetaldehyde as a model the different chemoselectivity options are shown in Figure 6 using benzaldehyde lyase from *Pseudomonas fluorescence* (BAL, large donor and acceptor binding site) and pyruvate decarboxylase from *Acetobacter pasteurianus* (PDC, small donor -, large acceptor binding site) as examples (Gocke et al., 2009; Maraite et al., 2007; Mosbacher et al., 2005). Due to these steric properties in the donor binding site, larger aromatic substrates such as benzaldehyde are preferred by BAL, whereas small aliphatic donor substrates are favored by PDC. As a consequence, the mixed carboligation of acetaldehyde and benzaldehyde yields two isomeric mixed products: 2-hydroxypropiophenone (2-HPP) by BAL-catalysis and phenylacetylcarbinol (PAC) by PDC catalysis (Figure 6).

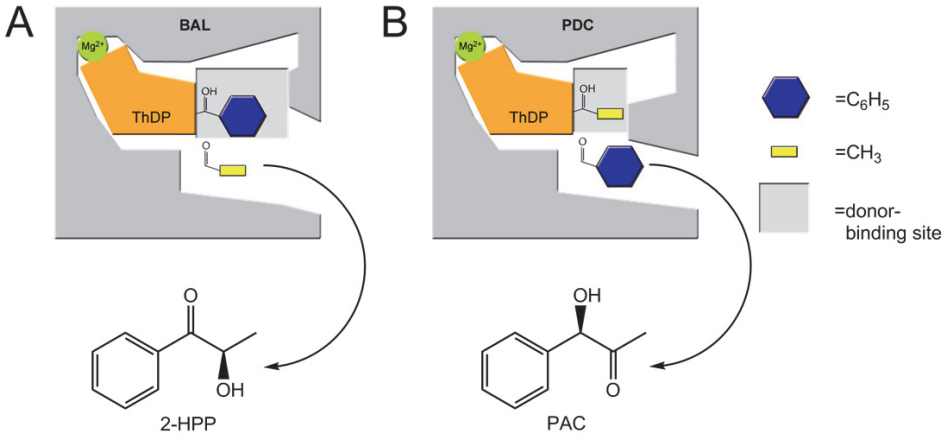


**Figure 6: Chemoselectivity of ThDP-dependent enzymes. A:** BAL has a large donor binding site, allowing bulky substrates (benzaldehyde) to bind first, which leads to the formation of 2-HPP with acetaldehyde as the acceptor. **B.** PDC has a smaller donor binding site than BAL, therefore only smaller substrates such as acetaldehyde may bind. The carboligation with benzaldehyde therefore yields PAC.

The stereoselectivity of the carboligation of benzaldehyde and acetaldehyde is subsequently explained based on the mixed carboligation catalyzed by BAL and benzoylformate decarboxylase from *Pseudomonas putida* (BFD). The main difference in the active sites of both enzymes is a structural element called the *S*-pocket in BFD that allows the antiparallel binding of the acceptor relative to the

ThDP-bound donor prior to C-C-bond formation. As the parallel binding mode is still possible in BFD, (*S*)-2-HPP is formed with an enantiomeric excess (*ee*) of only ca. 92% (Iding et al., 2000). Furthermore, bulkier acceptor substrates than acetaldehyde do not fit into the *S*-pocket and are therefore bound in parallel orientation yielding (*R*)-products. By contrast the stereoselectivity of BAL, which does not contain an *S*-pocket, is significantly higher, yielding (*R*)-2-HPP with an *ee* of 99% (Demir et al., 2001). Furthermore it was extensively shown that high enantiomeric excesses can only be obtained when at least one of the substrates is aromatic (Domínguez de María et al., 2007; Gocke et al., 2009). These findings further underline the importance of stabilization of donor and acceptor during the enzymatic carboligation using ThDP-dependent enzymes (Hailes et al., 2013).

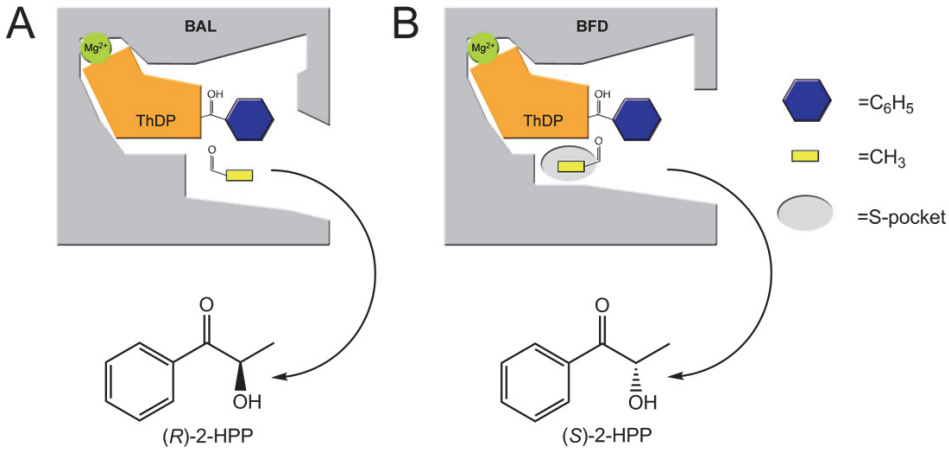


**Figure 7: Stereoselectivity of ThDP-dependent enzymes. A:** BAL features an acceptor binding site only allowing for parallel orientation of the acceptor aldehyde relative to the ThDP-bound donor and yielding (*R*)-2-HPP. **B:** The so-called *S*-pocket in BFD enables antiparallel orientation of the aldehyde acceptor, yielding (*S*)-2-HPP (Knoll et al., 2006)**.**

Chemoselectivity can be further improved by stabilizing the specific donor inside the active site through selection of different organic cosolvents (Gerhards et al., 2012). In recent literature it has furthermore been shown that the active center of ThDP-dependent enzymes can be engineered rationally in order to change the stereoselectivity of enzymes by either introducing an S-pocket for the acceptor

aldehyde or by modifying the donor binding site (Gocke et al., 2008; Westphal et al., 2013; Yep and McLeish, 2009).

## 1.4 BFD from *Pseudomonas putida* as model enzyme

Benzoylformate decarboxylases are known from a vast number of different species (*Pseudomonas aeruginosa* (Barrowman et al., 1986), *Bradyrhizobium japonicum* (Wendorff, 2006), *Acinetobacter calcoaceticus* (Barrowman and Fewson, 1985), *Pseudomonas stutzeri* (Saehuan et al., 2007), *Pseudomonas putida* (Hegeman, 1966). Among these BFD from *Pseudomonas putida* plays an important role as the best characterized BFD (Gerhards, 2012; Hegeman, 1966; Hilterhaus et al., 2008; Iding et al., 2000; Peper et al., 2011; Tural et al., 2013). BFD is a tetrameric enzyme with four active sites, each formed by two of the monomers (Bruning et al., 2009; Hasson et al., 1995; Polovnikova et al., 2003; Sprenger and Pohl, 1999). The native activity of BFD is the decarboxylation of benzoylformate to benzaldehyde and carbon dioxide in the mandelate metabolism (Hegeman, 1966) (Figure 8). For this reaction the enzyme shows a very high activity of 300 to 400 U/mg (Gocke et al., 2008; Iding et al., 2000). However BFD can also be utilized as a catalyst for the carboligation of benzaldehyde and acetaldehyde yielding the α-hydroxyketone (*S*)-HPP with an *ee* of 92% (Iding et al., 2000; Wilcocks et al., 1992) (Figure 8). Beside the carboligation of benzaldehyde and acetaldehyde a vast number of aromatic, heteroaromatic, aliphatic, cyclic aliphatic, and olefinic aldehydes have been tested as substrates yielding the respective α-hydroxy ketones with high *ee* (Dünnwald et al., 2000; Iding et al., 2000).

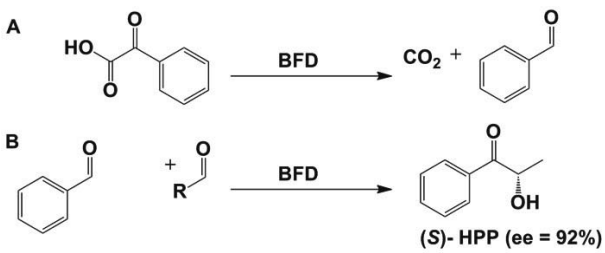


**Figure 8: Physiological decarboxylase activity of BFD and carboligase side activity. A:** Decarboxylation of benzoylformate **B:** Carboligation of benzaldehyde and acetaldehyde forming (*S*)-2-hydroxypropiophenone (HPP).

The influence of various process parameters on the continuous BFD-catalyzed carboligation of benzaldehyde and acetaldehyde in batch reaction mode and in a continuous stirred tank membrane reactor (enzyme membrane reactor) has been earlier investigated in detail (Iding et al., 2000). The findings encompass faster enzyme deactivation with increasing pH (6.5 to 8) and increasing temperature (10°C to 30°C), higher initial carboligase activity with increasing pH (6.5-8) and temperature (10°C to 50°C) as well as decreasing *ee* with increasing temperature (10°C to 50°C). The process optimum for the continuous reaction was determined between 20°C and 30°C at a pH of 7 to 7.5. Low concentrations of benzaldehyde (10 mM) gave the highest *ee*-values and a tenfold excess of acetaldehyde over benzaldehyde was determined to be favorable for high conversion. This detailed investigation of reaction parameters is especially interesting as BFD provides a well-characterized highly active model enzyme and has therefore been used before to test and characterize enzyme reactor systems before (Fagaschewski et al., 2012; Valinger et al., 2014).

## 1.5 Biocatalytic process development and multi-parameter optimization

A given process in biocatalysis is influenced by numerous parameters such as pH, shear stress, residence time (τ), buffer composition, cofactors, cosolvents, ionic strength, catalyst load, and substrate concentrations (to name only few). Identification of a respective optimum in this multi-parameter space by independent optimization for single parameters is not only laborious but also of limited success. As some parameters may interfere with each other the amount of data to be generated increases exponentially with the number of experiments per parameter and the number of parameters to be optimized. Different approaches for process optimization either decrease the number of experiments by using empirical algorithms, a mechanistic based algorithmic approach and/or employ high throughput experimental setups such as multiwell plates or microfluidic devices (Tufvesson et al., 2013).

However, the large number of experiments carried out during process development still generates high cost and is time consuming. This poses a bottleneck in terms of

process development. Therefore, novel approaches reducing the amount of enzymes, buffers, and substrates during development of biocatalytic processes have become an interesting field of study (Bolivar et al., 2011; Ferreira-Torres et al., 2005; Micheletti and Lye, 2006; Miyazaki and Maeda, 2006; Urban et al., 2006).

## 1.6 Enzyme reactor concepts

In enzyme catalysis the choice of a reaction system may significantly influence the performance of a given process (Tufvesson et al., 2013). Each reactor system has its advantages and drawbacks. In general there are three different types of idealized reactors: batch stirred tank reactor (BSTR), continuous stirred tank reactor (CSTR) and continuous plug flow reactor (CFPR) (Rao et al., 2009). While the BSTR features easy operation and well mixed reaction conditions, the substrate and product concentrations change with reaction time. Further, problems of this reactor concept are shear stress induced enzyme deactivation and the low volumetric yield. Due to the change of the reactant concentrations over time, the BSTR may not be the optimal choice process optimization in biocatalysis as this renders it impossible to adjust a constant optimized set of reaction parameters. Similar problems arise with a CFPR, which is used as a packed bed reactor in biocatalysis. While in the steady state the concentrations of substrate(s) and product(s) are constant at a given point within the reactor, respective concentration gradients form along the length of the reactor (Figure 9) (Illanes, 2008). A CSTR offers an interesting alternative as the reaction conditions can be adjusted to a steady state with optimal reaction parameters. There is no concentration gradient over the reaction time or the reactor compartment of a given volume within an ideal CSTR at steady state. Therefore, the defined reaction conditions within the reaction compartment make this reactor a very good choice for process development to investigate the influence of different parameters on the biocatalytic process (Illanes, 2008; Woodley, 2012). A schematic comparison of the three ideal reactor types is shown Figure 9.

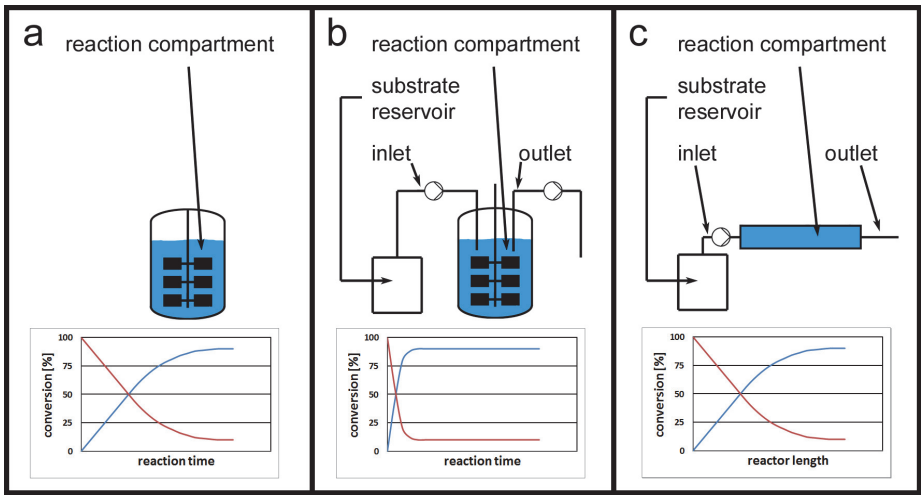


**Figure 9: Comparison of different reactor types. Conversion curves show substrate depletion (red) and product formation (blue). a:** Batch stirred tank reactor (BSTR): closed vessel with catalyst; homogenous reaction conditions for a given time point but decrease of substrate concentration and accumulation of product over reaction time; **b:** Continuously stirred tank reactor (CSTR): constant substrate feed and product effluent; homogenous reaction conditions over time and perfect mixing within the reaction compartment of an idealized CSTR; **c:** Plug flow reactor: gradient of substrates and products along the length of the reaction compartment; constant reaction conditions at a given point within the reactor (Illanes, 2008; Woodley, 2012).

A vast number of applied reactor systems have been developed, such as membrane reactors, packed bed reactors, and fluidized bed reactors. An exemplary type of a CSTR is the widely used continuously stirred tank ultrafiltration membrane reactor. This type of setup is also called enzyme membrane reactor (EMR) (Wandrey, 1979) and consists of a continuously stirred tank reactor utilizing an ultrafiltration membrane for enzyme retention (Giorno and Drioli, 2000; Rios et al., 2004). While substrates and products may pass through the membrane the enzyme is retained within the reactor in a soluble form. A widely used alternative to the EMR for immobilized biocatalysts is a stirred tank reactor with the catalyst immobilized on carriers either as a batch system or with a carrier retention system in continuous mode (Tischer and Kasche, 1999).

In a fluidized bed reactor gravity is used to retain beads, which incorporate the catalyst, inside a reaction compartment. As a subtype of the plug flow reactor this concept requires an equilibrium between gravitational forces and flow rate/resistance

force on the beads for optimal distribution of the catalyst along the reaction compartment (Coughlin and Charles, 1977).

### 1.6.1 Continuous reactors for enzyme process optimization

In an ideal CSTR the reaction will only be influenced by the enzyme kinetics and its stability, as the reaction compartment is perfectly mixed providing homogenous reaction conditions with constant concentrations of substrates and products (Schmid et al., 2001). However in reality different factors may negatively influence the enzyme activity such as substrate surplus inhibition, product inhibition, competitive and non-competitive enzyme inhibition as well as temperature, pH, shear forces, reactor material etc. For a process the inactivation rate of an enzyme can be described as an exponential decay (equation 1) with $A_t$ = activity at a defined time point, $A_0$ = initial activity, $k_{des}$ = inactivation constant, and t = time.

$$\boldsymbol{A_t = A_0 * e^{(-k_{des} * t)}} \qquad 1$$

For a given enzyme the conversion rate in the steady state of the reactor is inversely proportional to the residence time, enzyme load and its activity. Therefore the mass balance in the CSTR can be derived from equation 2 with $n_0$=initial substrate amount in moles, n=outlet substrate amount in moles, τ=residence time and v=reaction rate.

$$\boldsymbol{\frac{n_0 - n}{\tau} = v} \qquad 2$$

For a plug flow reactor calculation of the mass balance is more complicated due to the length/residence time-dependent concentration gradients of substrate(s) and product(s) over the length of the reactor, which may locally affect enzyme specific parameters differently. A plug flow reactor may be simulated by an infinite series of CSTRs (Van Erdeghem et al., 2011). A non-ideal CSTR can often be simulated as a finite series of CSTRs with different concentrations of substrate(s) and product(s) where the inlet conditions of one reactor equal the outlet concentrations of the previous one.

In production processes a high conversion (> 95%) should be maintained as long as possible in order to make full use of the substrate and achieve high product concentration. An ideal CSTR with 100% conversion under steady state conditions is

depicted in Figure 10a. Depending on the stability of the biocatalyst under the conditions tested, progressive inactivation will result in reduced conversion over time Figure 10b. This effect will be more pronounced the lower the enzyme load in the reactor is.

However, the situation is different for process optimization. Here the goal is to analyze as many process parameters as possible as fast as possible. There a reaction setup resulting with a long steady state, in which the influences of different parameters cannot be quantified, is not advantageous. For rapid parameter optimization during process development a low enzyme load combined with a short residence time should be particularly advantageous, since the constant conversion phase is short but the conversion curves nevertheless enable the determination of optimal conditions (Figure 10c) and inactivation effects such as enzyme inhibition or denaturation due to reaction conditions (Figure 10d).

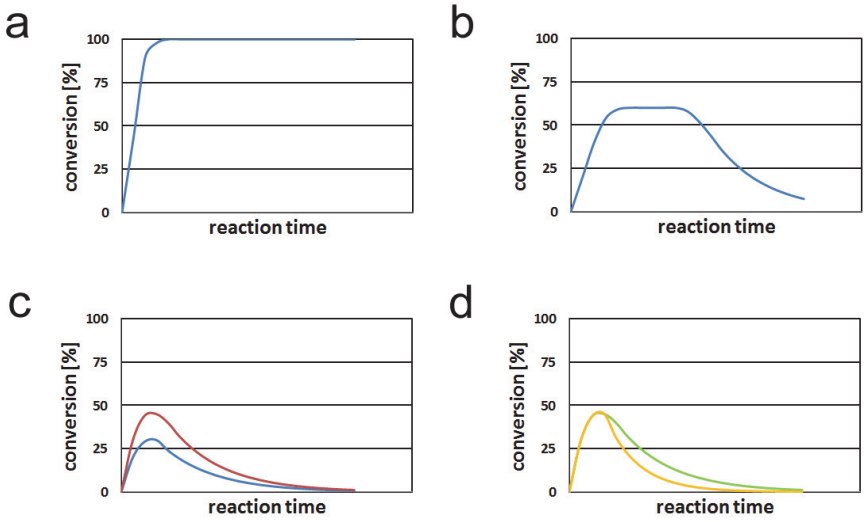


**Figure 10: Product formation in continuous reactors for process development. a:** Ideal CSTR with 100% conversion without enzyme inactivation; **b**: real CSTR with 60% conversion during steady state and enzyme inactivation; **c**: Comparison of two CSTRs with different initial activities and equally fast enzyme inactivation; **d**: comparison of two CSTRs with different enzyme inactivation rates.

## 1.7 Microfluidics

Microfluidics describes sub millimeter fluidic devices for handling small volumes in the µL to fL range. Due to the small volumes they feature low liquid costs, low energy consumption compared to bench scale fluidic systems, laminar flow, large surface areas per volume, and diffusion based transport vertical to the flow direction; the so called effects of micro scale (Squires, 2005; Whitesides, 2006). In the last two decades microfluidics came more and more into the focus of interest of biotechnology as an alternative for many bench scale applications. Microfluidics proved to be a key technology for reaching milestones in biotechnology such as second generation sequencing, enabling for example the decoding of the human genome (Margulies et al., 2005; Shendure and Ji, 2008). Furthermore, a multitude of different reactor types for chemical, biochemical, and microbial processes has been developed (Abgrall and Gue, 2007; Kintses et al., 2010; Krenková and Foret, 2004). In analytics microfluidics has become an everyday application, as laboratory devices such as the nanodrop photometry, capillary gel electrophoresis, flow cytometry, and DNA chip technology are widely used (Baker, 1995; Robertson and Box, 2003; Sun and Morgan, 2010; Wang and Li, 2011). Currently one of the aims of microfluidics is to establish “lab on a chip” platforms that integrate laboratory processes and all analytics in one microfluidic device. Therefore, a multitude of different processes has been established at microscale such as single cell analysis, chromatographic processes, and a multitude of analytics assays (Asanomi et al., 2011; Lim et al., 2010; Mark et al., 2010; McCalla and Tripathi, 2011; Neuži et al., 2012; Schäpper et al., 2009; Urban et al., 2006). While microfluidics features a significant decrease in materials cost due to lower consumption of chemicals and solvents, the initial investment to develop completely new systems and processes at microscale poses a hurdle for further application in biotransformation (Bolivar et al., 2011). Additionally the relatively high cost of microfluidic chip prototyping and manufacturing has to be taken into account. Continuous flow microfluidics comprise of a closed channel system through which fluids are pumped either by external or microfluidic pumping devices. As a tool for enzyme process optimization, continuous flow microfluidics offers a great perspective as a continuous flow microreactor can be operated under steady state conditions mimicking a CSTR. Additionally samples can be collected and analyzed by standard bench scale analytics such as HPLC and GC.

## 1.8 Microscale flow

A fluid can either flow in parallel layers, called laminar flow, or the fluid can intermix between the layers, which is called turbulent flow. The concept of turbulent and laminar flow was developed in 1883 by mathematician Reynolds whose famous flow tube experiment illustrated the different behaviors of a fluid depending on the flow rate (Reynolds, 1883). The so-called Reynolds number (Re) is a dimensionless number, which describes the ratio of inertial forces to viscous forces. It is used as a means to characterize the flow in a given fluid mechanics problem. Equation 3 defines the Reynolds number with *u* denoting the flow velocity, *l* the characteristic length, $\rho$ the density, and $\eta = \nu \cdot \rho$ the dynamic viscosity; $\nu$ is the kinematic viscosity (Brody et al., 1996).

$$\boldsymbol{Re} = \frac{\boldsymbol{\rho \cdot u \cdot l}}{\boldsymbol{\eta}} \qquad 3$$

The Reynolds number gives a measure to characterize whether a given problem involves laminar or turbulent flow. Once a problems specific critical Reynolds number threshold is exceeded, which is typically between $10^{-2}$ and $10^{-4}$, the flow becomes turbulent. Reynolds numbers <<1 persist at micro scale, indicating that the flow in micro volume flow cells is always laminar. However, laminar flow may pose a problem for reaction systems, due to diffusion limited transport and reaction rates. Therefore novel technologies to introduce active transport into these devices ,e.g. some degree of turbulence, are being studied (Brody et al., 1996).

In case of carrier-based catalyst retention in a flow cell the retention force on the beads has to be stronger than the flow resistance of the beads. The flow resistance ($F_w$) of a spherical bead for laminar flow has been determined by G. G. Stokes in 1851 (Stokes, 1851):

$$\boldsymbol{F_w = 6 \cdot \pi \cdot r \cdot \eta \cdot u} \qquad 4$$

with *u* denoting the inflow velocity, and *r* the radius of the sphere.

While the viscosity is constant for a given aqueous reaction mixture, the inflow velocity as well as the diameter of a spherical carrier may change and alter the flow

resistance of the carrier. On one hand, smaller carriers may be favorable due to smaller influence of diffusion limitation on the reaction rates (Tischer and Kasche, 1999), on the other hand, larger beads feature a larger volume to surface ratio. This is, assuming a constant (i.e. magnetic) holding force per volumetric unit, favorable for bead retention as the flow resistance per bead volume is effectively decreased.

## 1.9 Computational fluid dynamics

The Navier-Stokes equations describe the flow of Newtonian fluids and are widely applied for Computational Fluid Dynamics (CFD) simulations. Equation 5 shows the Navier-Stokes equations for incompressible flow without external forces (*p* denotes pressure):

$$\boldsymbol{\rho} \cdot \left(\frac{\partial \boldsymbol{u}}{\partial \boldsymbol{t}} + (\boldsymbol{u} \cdot \boldsymbol{\nabla})\boldsymbol{u}\right) = -\boldsymbol{\nabla p} + \boldsymbol{\eta}\Delta \boldsymbol{u} \qquad 5a$$

$$\boldsymbol{\nabla} \cdot \boldsymbol{u} = \mathbf{0} \qquad 5b$$

In case of stationary flow, i.e. a time invariant velocity profile, which is typically the case in microfluidic applications, equation 5a simplifies to equation 6:

$$\boldsymbol{\rho} \cdot \left((\boldsymbol{u} \cdot \boldsymbol{\nabla})\boldsymbol{u}\right) = -\boldsymbol{\nabla p} + \boldsymbol{\eta}\Delta \boldsymbol{u} \qquad 6$$

For creeping flow (Reynolds numbers <<1) equation 6 can further be simplified to equation 7:

$$-\boldsymbol{\nabla p} + \boldsymbol{\eta}\Delta \boldsymbol{u} = \mathbf{0} \qquad 7$$

Equations 7 and 5b together are called Stokes equations. For practical applications these equations need to be numerically solved, as explicit solutions exist only for a few special cases (Wang, 1991). Microfluidic channels with laminar flow and without turbulences can be described by Stokes equations (Stone et al., 2004). The mass transport may then be calculated using a stationary velocity profile and solving a time-dependent convection and diffusion equation (equation 8).

$$\frac{\boldsymbol{dc}}{\boldsymbol{dt}} = -\boldsymbol{u} * \boldsymbol{\nabla}\mathbf{c} + \mathbf{D}\Delta\mathbf{c} \qquad 8$$

With *c* denoting solute concentration, and *D* the diffusion coefficient.

## 1.10 Microscale enzyme reactor concepts

In the last two decades numerous microscale systems for enzyme catalysis have been developed. They include packed-bed, membrane-based, and laminar flow concepts (Asanomi et al., 2011; Bolivar et al., 2011; Fagaschewski et al., 2012). Each of these systems has specific advantages and drawbacks. In laminar flow reactors the enzyme- and the substrate/product solutions flow next to each other in a simple setup consisting of one long channel with two inlets and one or two outlets. However, the reaction may become diffusion-limited due to the laminar flow conditions. The diffusion-limited reactions necessitate high enzyme amounts in order to ensure high product formation (Pohar et al., 2009; Šalić et al., 2013).

Furthermore, the laminar flow reactor, as a classical plug flow reactor, shows the main drawback of a plug flow reactor: substrate and product concentration gradients along the length of the channel, which hinder the determination of kinetic parameters due to the variation of substrate/product/enzyme concentrations at different positions along the length of the reactor. Another problem of many laminar flow reactors is the inhomogeneous separation of both flows at the end of the reactor due to inhomogeneity of the microfluidic chips and diffusion effects (Šalić et al., 2013). This in combination with pump pressure pulses impairs recirculation of the enzyme (e.g. by recirculation of the enzyme flow), which results in relatively large enzyme consumption. Due to these disadvantages laminar flow systems are not advantageous for process optimization.

A different approach, which allows trapping the enzyme in the microfluidic reactor without complex flow recirculation, is immobilized enzyme reactors (IER). One method of enzyme immobilization within a microfluidic device is direct immobilization of enzyme at the walls of a microfluidic channel. However, this procedure requires chemical crosslinking, which may result in partial enzyme inactivation or other undesired changes of the enzymatic properties. Furthermore, the interfacial area between the substrate/product flow and the enzyme immobilization matrix is very small, resulting in low diffusion-limited reaction rates (Asanomi et al., 2011). The drawback of the limited interfacial area can be avoided by packed bed bead based microreactor systems. Such packed bed reactors even show some mixing of laminar flows (Seong and Crooks, 2002). Packed bed microfluidic reactors feature a

relatively easy enzyme immobilization. By use of porous bead material the immobilization surface and thus the amount of immobilized enzyme as well as the enzyme substrate interaction are also considerably higher than in reactors with channel wall immobilization. Among the IER reactors magnetic bead based systems are of high interest as loading, retention and removal of the biocatalyst coupled to magnetic beads can easily be handled using a magnet. The drawbacks of this concept are: high backpressure (Dräger et al., 2007; Srinivasan et al., 2004) or in some cases even clogging of the reactor (Li et al., 2007; Nomura et al., 2004).

Even though IERs are easier to handle in terms of enzyme retention than laminar flow reactors, the problem of a concentration gradient along the length of the plug flow type reactor persists. Another concept, presented by Fagaschewski et al. is the miniaturization of the EMR to 200 µL (Fagaschewski et al., 2012). This CSTR system presents an interesting approach in terms of enzyme retention, mixing and control of reaction parameters. However, the relatively large volume of 200 µL still results in relatively high buffer, enzyme and substrate consumption.

## 1.11 Enzyme immobilization

Especially for the implementation in industry enzyme immobilization plays an important role, either to enhance enzyme stability and/or to simplify enzyme retention and recycling. Therefore, numerous studies have been carried out dealing with the immobilization of a vast variety of enzymes (Sheldon and van Pelt, 2013). However, the comparison of different studies is impaired by the fact that most immobilizations are compared to the free enzyme as a reference but not among each other (Sheldon, 2007).

In general, enzyme immobilization can be achieved by three different concepts: carrier-based binding of the enzyme, covalent crosslinking of the enzyme by respective chemical reagents, and entrapment/encapsulation in polymer matrices. While cross-linked enzyme aggregates (CLEAs) and cross-linked enzyme crystals (CLECs) offer carrier-free enzyme beads, crosslinking of the enzyme may lead to impaired enzyme activity even though cases of enhanced activity have been reported (Sheldon et al., 2005; Sheldon, 2007; Sheldon and van Pelt, 2013).

Entrapment/encapsulation using Sol-gels, membranes or hollow fibers often require additional covalent binding of the enzyme to the support or enzyme crosslinking to prevent leakage (Sheldon and van Pelt, 2013). Therefore the borders between covalent carrier-based binding and entrapment/encapsulation are often not clear. Additionally, entrapment of enzymes may lead to decreased reaction rates by diffusion limitation (Hanefeld et al., 2009). For microscale applications reproducible quantification of carrier-free systems like CLEAs, CLECs, achieved via specific interactions as well as entrapped enzymes is difficult. Here, carrier-based (.g. using metal ion chelate binding or unspecific binding via adsorptive or covalent interactions) immobilizates are easier to handle in terms of quantification, dilution, and retention of the enzyme. Covalent and therefore in most cases unspecific binding of an enzyme to a carrier may also result in unspecific binding of impurities contained in the sample, since respective procedures usually target amino groups on the protein surface. However, increased stability has been reported for numerous covalently attached enzymes (Sheldon and van Pelt, 2013). The applicability of covalent immobilization and entrapment varies strongly between different enzymes. While both of these methods are cheap and versatile for immobilization, a purification of the enzyme has to be carried out first in order to achieve high activity and to prevent immobilization of other enzymes/impurities. For rapid enzyme immobilization affinity-tag based immobilization through various protein tags (i.e. e. Strep-Tag, His-Tag) linked to the C- or N-terminus of recombinant enzymes offers an interesting alternative for direct and selective enzyme immobilization also from crude cell extracts (Asanomi et al., 2011; Ha et al., 2012; Zhang et al., 2013).

### 1.11.1 Ni-NTA-based immobilization of ThDP-dependent enzymes

Among protein tags used for immobilization, the His-tag is of special interest because many enzymes in research are already available as His-tagged variants due to the wide application of immobilized metal ion affinity chromatography (IMAC) for protein purification. It is based on the complexation of a polyhistidine residue (six to ten histidines) with a divalent metal ion (usually $Ni^{2+}$) (Hochuli et al., 1988). The most common form is the use of matrix-bound 2,2′,2″-nitrilotriacetic acid as a complex ligand for divalent nickel ions (Ni-NTA). Other ions such as $Cu^{2+}$, $Co^{2+}$,

$Mn^{2+}$, $Fe^{2+}$ or $Fe^{3+}$ have also been reported (Lloyd R. Snyder, Joseph J. Kirkland, 2010; Lottspeich, Friedrich, Engels, 2006).

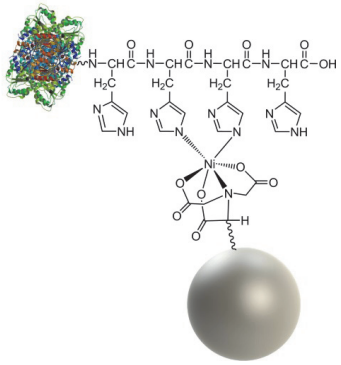

**Figure 11: Ni-NTA-based specific binding of a protein to Ni-NTA beads.** Complex formed by two neighboring histidine residues with the divalent nickel ion complexed by the 2,2′,2″-nitrilotriacetic acid (NTA) matrix.

Previous work already described successful applications for His-tag immobilized ThDP-dependent enzymes in biotransformations. BAL was immobilized via His-tag and used for batch, repetitive batch, and continuous carboligation experiments (Kurlemann and Liese, 2004). Furthermore, BFD, serving as a model enzyme in this thesis, has been immobilized on an Ni-NTA matrix via His-tag successfully by Tural et al. (Tural et al., 2013). Additionally the transketolase from *E. coli* has been successfully immobilized reversibly via His-tag and used in a microreactor (Matosevic et al., 2009).

A wide range of Ni-NTA matrices with different porosities, bead diameters as well as additional features such as ferromagnetism or superparamagnetism are commercially available. Superparamagnetic beads are favorable for the use in microreactors applying magnetism for bead retention, as the particles are only magnetic when positioned within a magnetic field (chapter 1.12). This allows easier handling and quantification of the particles in absence of a magnetic field. One specimen of superparamagnetic beads from Millipore®, (Millipore PureProteome Nickel magnetic beads), which was used throughout this thesis, is a polymer matrix around an inorganic core which is pre-loaded with $Ni^{2+}$ ions. It offers enzyme immobilization without the diffusion limitation of a completely porous material.

## 1.12 Magnetism

Magnetic fields exhibit forces on materials with magnetic properties. Magnetic fields can be generated in two types of magnetic setups: an electric current or a permanent magnet (Hans Christian Ørsted 1820). A magnetic field generated by an electric current follows Ampère's circuital law (Ampére, 1826). The most commonly used setup for an electromagnet therefore consists of a coil around a core of a magnetizable material. The generated magnetic moment increases with increasing electric current as well as each additional winding of the coil of an electromagnet. Furthermore, the coil wire diameter defines the electric resistance of the wire and therefore the heat generation at a given current. For a given size of an electromagnet the magnetic moment generated is directly correlated to its heat dissipation. If heat generation becomes an issue, as it is the case for a microbioreactor system used for biocatalysis, permanent magnets offer an alternative to induce magnetic fields.

The magnetic flux density ($\vec{B}$) can be used to describe these magnetic fields. The force ($\vec{F}$) exerted on an object within the magnetic field can be expressed as a function of the gradients of magnetic flux density ($\vec{B}$) and magnetic moment ($\vec{m}$) of the object (equation 9).

$$\vec{F} = \nabla(\vec{m} * \vec{B}) \qquad 9$$

The magnetization ($\vec{M}$) describes the magnetic moment per volume (equation 10).

$$\vec{M} = \frac{d\vec{m}}{dV} \qquad 10$$

The magnetization in turn is dependent on the geometry of an object as well as its magnetic permeability. The permeability is a constant in vacuum ($\mu_0$) but becomes dependant on the material properties.

For a spherical object magnetization is given by equation 11 with $\mu_r$ as the permeability relative to vacuum (Jackson et al., 1999).

$$\vec{M} = \frac{3}{4\pi}\left(\frac{\mu_r - 1}{\mu_r + 1}\right) * \vec{B} \qquad 11$$

Due to these relations the force applied on a magnetizable object within a magnetic field depends not only on the field applied but also on the magnetic permeability of the object as well as its geometry. The permeability is a good measure to characterize the magnetism of a given material. If the permeability is < 1 a material is diamagnetic. In case of a relative permeability > 1 paramagnetism is persistent, whereas a relative permeability >> 1 is characteristic for ferromagnetic materials. While in many materials the different components have a specific magnetization, the overall or macroscopic magnetization of a material is the sum of its components.

In ferromagnetic materials the magnetic dipoles of the elementary particles are not independent. So the magnetic dipoles are arranging in parallel spontaneously and form the so-called magnetic domains of nanometer to micrometer scale. Due to the random orientation of these domains a ferromagnetic material normally appears not to be magnetic. The exposure to a magnetic field now directs all magnetic domains into the same orientation, thus generating the macroscopic magnetic moment. This magnetic moment persists upon removal from the external magnetic field up to a given magnetization, the so-called remanence. Thus a permanent magnet is created. It has to be noted that the concept of a permanent magnet violates the relation described in equation 11 due to the fact that magnetism persist upon removal of the magnetic field. A permanent magnet can be demagnetized by heating above the so-called Curie temperature or by exposure to an adverse magnetic field. Physical stress (falling down) may also decrease the magnetization of a permanent magnet.

Paramagnetism consists of independent magnetic dipoles. These dipoles are naturally randomly oriented. If a magnetic field is applied to a paramagnetic material, the dipoles are oriented in the direction of the magnetic field, but return to their random orientation once the field is removed. Superparamagnetism describes the phenomenon that a multitude of different microscopic ferromagnetic moments behaves like a paramagnet, as if they each had an independent magnetic spin. This allows for objects which behave like a paramagnet but have a much larger magnetic permeability. Diamagnetism is persistent in materials which induce a magnetic field

directed against a magnetic field applied on the material. The magnetic field flux density is lower in these materials than in the vacuum with a $\mu_r<1$.

Due to relations described by equations 9 and 11 objects with ferro- or paramagnetic properties (positive magnetization) tend to be drawn into regions with higher magnetic flux densities, whereas diamagnetic materials (negative magnetization) tend to move to areas with lower magnetic flux densities. Dia- and paramagnetism can be neglected for most applications involving magnetic adhesion due to the fact that their effects are minimal when compared to ferromagnetic behavior.

Beside ferromagnetism, paramagnetism and diamagnetism, there are three other kinds of magnetic phenomena; ferrimagnetism, antiferromagnetism, and meta-magnetism, which are of no relevance for this thesis and are therefore not further discussed.

## 1.13 Active mixing in microfluidic devices

A multitude of different approaches has been implemented for mixing in microfluidic devices. Among them are active as well as passive mixers (Blom et al., 2010; Kuo and Chiu, 2011; Verbarg et al., 2012). The construction of micro stirrers is challenging (Zhang et al., 2006) and passive mixers cannot be used with carrier-based immobilization due to clogging of the mixing structures by the beads. Therefore magnetic bead mixing is an interesting novel approach. However, a magnetic bead-based immobilization is limited by the relation of the flow resistance of the beads versus the holding force the magnetic field applies on the beads. Due to the fact that many suppliers do not provide data on the magnetization of their beads the retention of each set of magnetic beads has to be examined experimentally.

Many different experimental layouts to implement magnetic bead movement, utilizing a vast number of electric- as well as permanent magnet arrays have recently been published (Lee et al., 2009; Lund-Olesen et al., 2008; van Pelt et al., 2011; Wang et al., 2007). On the one hand electromagnets feature easy adjustability of field direction, strength, and frequency, but on the other hand they generate heat (Liu et al., 2011), which is a major drawback for chemical and biotechnological reaction

systems as a defined temperature is crucial for such systems. This problem can be solved by using permanent magnets. However, existing permanent magnet systems show moving magnetic elements underneath the microfluidic chip (Verbarg et al., 2012). This setup has a number of drawbacks for reaction systems. Leakage at the macro- to micro interface can cause damage to electric and/or mechanic components of the magnetic field setup. Additionally, the implementation of a temperature control system placed underneath the reaction chamber is hindered by the magnetic agitation setup. Furthermore, the application of a magnetic force drawing beads to the bottom of a microfluidic channel imposes the threat of shear stress induced damage to enzymes immobilized on the magnetic beads. Finally, microscopic observations in such a setup to characterize the system are impaired.

## 1.14 Charge-coupled device sensor-based dye distribution analysis

Charge-coupled device sensors can be used to obtain a two-dimensional image (Amelio et al., 1970). Such sensors are used for image generation in commercially available digital cameras. A digital camera records an image by generating values for red, green, and blue, which can be used to generate all visible colors according to the Young-Helmholtz theory (Helmholtz, 1909). Today the red green blue (RGB) color space is defined by setting a digital value for each pixel of an image. This is depicted below in Figure 12 as a three-dimensional cube in which each of the three colors (red, blue and green) is represented by one axis. Every color can now be defined by a coordinate within this cube as exemplarily depicted in Figure 12c.

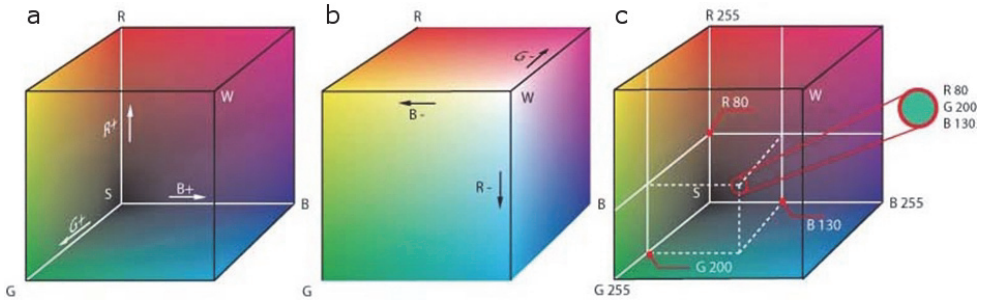


**Figure 12: RGB color space definition as a cubic view.** All visible colors may be described using a given R G B coordinate within this three dimensional cube. **a+b:** visualization of the RGB color space, **c:** exemplary definition of a green pixel (Frank, 2004)**.**

Each of these three values for a given pixel cannot only be used to visualize the respective image but may also be read out as a data point and can be used as a relative photometric signal (Werts et al., 2012).

## 1.15 Aim of the project

Enzyme reactors are traditionally used at bench scale (volume 1 - 100 mL) for process development and optimization before further upscale. However, the concept of bench-scale reaction systems for process development is time-consuming and requires large amounts of enzymes and reagents. Furthermore, parallelization to evaluate different reaction conditions is limited, which results in long process development times. Therefore, continuous-flow microfluidics offers an alternative perspective for biocatalytic process optimization. A well-mixed continuous flow microreactor could be operated under steady state conditions mimicking a CSTR. Additionally, samples can be collected and analyzed by standard bench scale analytics such as high performance liquid chromatography (HPLC) and gas chromatography (GC).

The objective of this project was to develop, build, and test such a continuously operated microfluidic reactor with immobilized enzyme for process optimization of an enzymatic carboligation process. The system should mimic a CSTR and utilize magnetic beads for easy metal chelate-based immobilization and allow easy parallelization of the reactor setup. A microfluidic process optimization reactor based

on highly specific enzyme immobilization on magnetic beads could be used to immobilize enzyme directly from crude extract. In order to obtain process relevant parameters as fast as possible, the system should be tested using high flow rates and low enzyme loads (chapter 1.6.1). If such a system was constructed successfully, it would lower the amount of enzyme, buffer, and substrates by several orders of magnitude relative to a commonly used bench scale reactors and therewith reduce the costs and effort of enzyme process development significantly. Thus, the time for optimization could be reduced significantly.

## 1.16 Catalogue of demands

In order to achieve the aim of this project, the demands for such a microfluidic reactor system were defined as follows:

- Reproducible and easy enzyme retention
  It is essential for a process optimization tool to retain the enzyme within the reaction compartment without laborious working steps. Especially when numerous different variants of an enzyme are comparatively studied to identify the best for the process, an easy immobilization, preferably from crude cell extract, would be favorable.

- Modular setup
  Due to the highly experimental character of this project, numerous different previously published microreactor concepts, such as packed bed or laminar flow reactor, were initially considered as fall back plans for this thesis. Therefore, the reactor system had to be designed as a modular setup, allowing for the adaptations necessary to be used for different microreactor concepts. Additionally a modular setup has the advantage of simple step by step setup, operation and maintenance.

- Solvent resistance
  The synthesis of chiral α-hydroxy ketones by carboligation of cheap aldehydes necessitates reaction systems which are able to sustain the volatile

and very reactive aldehydes. Therefore a completely capsuled reaction system is crucial to maintain defined reaction conditions and close the mass balance.

- Easy parallelization

  As the reaction system is supposed to be used for process development one of the main demands is parallelization of the reaction. This will allow investigation of the influences of different parameters at the same time, increase the sampling volume by parallel runs and to perform experimental replicates at the same time.

- Simple setup

  A simple easy-to-use setup ensures a failsafe use and is crucial for any laboratory equipment. Any reaction system not being easy to use would increase the hurdle for users to apply it.

- Temperature control

  A defined reaction temperature is essential, as biocatalytic processes are strongly temperature-dependent. The temperature may have an effect on chemical side reactions, stereoselectivity, as well as the enzyme activity and stability.

- Scalability

  It is crucial for future application of a process development reaction system to proof that data obtained at micro scale is similar to respective bench scale studies. However, as many parameters in microfluidic systems are intrinsically different to bench-scale systems (reactor material, enzyme retention, surface-volume relations, sheer stress), it is expected that some differences in enzyme activity and stability will be observed. Nevertheless, general trends concerning the response of a given enzyme towards reaction parameters such as pH, T, and substrate concentration (relation) should result in similar trends. In our case a 10 mL enzyme membrane reactor (Iding et al., 2000; Wandrey, 1979) was defined as the bench scale reference.

As none of the microfluidic reactor systems described in chapter 1.11 meets all the required criteria for our microfluidic process optimization tool, a novel enzyme microreactor concept utilizing magnetic beads for enzyme immobilization and mixing should be developed in this thesis.

# 2 Materials and Methods

## 2.1 Software

| | |
|---|---|
| AMPERES® software | magnetic field simulation/reactor development |
| ChemBioOffice 2010 | chemical structure and equation drawings |
| Chemstation | HPLC analysis |
| COMSOL | CFD simulations |
| DIYPhotobits | time lapse photography |
| Python 2.7.3 | dye distribution image analysis |
| Solidworks 2010/11 | construction of reactor system |
| Labview | reactor control (controls programmed by Andra Rübsteck, Forschungszentrum Jülich IBG1) |
| NanoPro | reactor control |

## 2.2 Chemicals

All chemicals, if not stated otherwise, were obtained from Fluka/Sigma Aldrich Chemie GmbH (Steinheim Germany), Merck KGaA (Darmstadt, Germany, Carl Roth GmbH + Co. KG (Karlsruhe, Germany. BFD overexpression recombinant *E. coli* BL21 (DE3) cells for enzyme purification were obtained from workgroup internal stocks.

## 2.3 Equipment

**Table 1: Equipment used during experiments.**

| Equipment | Manufacturer | Model |
|---|---|---|
| **Pipettes** | Eppendorf | Research |
| **Electronic pipette** | Eppendorf | Research pro |
| **Multichannel pipette** | Eppendorf | Research pro electronic |
| **Cuvettes** | Brand | Half micro 1 mL |
| **Reaction tubes** | Merwe | 1.5 mL, 2.0 mL |
| **Reaction tubes** | Greiner | 15 mL, 50 mL |
| **96 well plates** | Nunc | F96 |
| **Vortex** | Scientific Industries | Vortex Genie 2 |
| **Centrifuge** | Bechman Coulter | Avanti J20 XP |
| **Water bath** | Laudo | M3 |
| **Photometer** | Shimadzu | UV1601 |
| **96 well plate reader** | Tecan | M1000 infinity |
| **Pipetting robot** | Tecan | Freedom evo |
| **Vacuum pump** | Ilmac | |
| **Sonifier** | Dr. Hielscher | UP-200s |
| **Chromatography column (Qiagen Ni-NTA Superflow)** | GE healthcare | XK 26 |
| **Chromatography column (size exclusion)** | GE healthcare | XK 50 |
| **Chromatography system** | GE healthcare | Äkta Purifier |
| **Luer adapter** | Idex | 052P-659 |
| **Tubing connector** | Idex | 052P-201 |
| **Glass syringe 1.0 mL** | Hamilton | TLL1001 |
| **Glass syringe 2.5 mL** | Hamilton | TLL1002 |
| **Analytic HPLC** pump** | Agilent/Hewlet Packard | G1332A/G1379A |
| **Analytic HPLC degasser** | Agilent/Hewlet Packard | G1312A |
| **Analytic HPLC autosampler** | Agilent/Hewlet Packard | G1329A |
| **Analytic HPLC thermostat** | Agilent/Hewlet Packard | G1330A/G1330B |

| Equipment | Manufacturer | Model |
|---|---|---|
| **Analytic HPLC column compartment** | Agilent/Hewlet Packard | G1316A |
| **Analytic HPLC detector** | | G1315A |
| **Analytical chromatography guard cartridge** | Daicel CHIRALPAK | ID L=10 mm, 4.0 mm ID, 5 µm particles |
| **Analytical chromatography column** | Daicel CHIRALPAK | ID L=250 mm, 4.6 mm ID, 5 µm particles |
| **Microscope** | Nikon | Diaphot |
| **Enzyme membrane reactor** | IBG1 custom build | 10 mL |
| **Pump EMR** | Pharmacia | Pump-500 |
| **Fraction collector EMR** | Pharmacia | Frac100 |
| **Ultrafiltration membrane** | Millipore | 30 Kd |
| **Microreactor system prototype** | IBG1 custom build | For 15 x 45 mm Micronit chips |
| **Microreactor system** | IBG1 custom build | For 15 x 45 mm Micronit chips |
| **Microfluidic chips** | Micronit | Custom build |
| **Syringe pump** | Landgraf* | LA-160 |
| **Fraction collector** | BasiInc | Honeycomb micro |
| **PTFE tubing*** ** | Idex | 1/16 OD, 100 µm ID |
| **PEEK tubing**** ** | Idex | 1/16 OD, 100 µm ID |
| **FEB tubing***** ** | Idex | 1/16 OD, 10 µm ID |
| **Magnetic beads** | Millipore | PureProteome Nickel magnetic beads (10 µm) |

***Landgraf syringe pumps are identical to the respective new era syringe pump models; **High performance liquid chromatography; *** polytetrafluoroethylene; **** polyether ether ketone ***** fluorethylenepropylene**

## 2.4 Magnetic modelling

AMPERES® software was used for simulation of the magnetic flux density within the microfluidic reaction chambers. The geometries were exported form Solidworks as .STEP files and then imported to AMPERES® for magnetic field simulation. Magnetic modelling was carried out by Dr. Helmut Soltner (Zentralinstitut für Engineering, Elektronik und Analytik , Forschungszentrum Jülich). For magnetic modelling the magnetic properties as described in chapter 2.6 in a vacuum were used.

## 2.5 CFD Simulation

Computational fluid dynamics (CFD) simulations using a numerical approach were used for verification of the dye distribution measurements (chapter 1.9). The commercial software COMSOL Multiphysics was used. The fluid properties were assumed to be that of water ($\rho$ = 998.2 $Kg\ m^{-3}$, $\eta$ = 0.001 $Pa\ s$). The diffusion coefficient for rhodamine B used was $D = 4.27 \cdot 10^{-6}\ cm^2\ s^{-1}$ (Gendron et al., 2008). CFD simulations were carried out by Dipl.-Ing. Birgit Stute (IBG 1).

## 2.6 Relevant materials properties for construction of the µMORE

**Table 2: Properties of different construction materieals used for the µMORE**

| Material | Relative permeability | Thermal conductivity*** $W\ m^{-1}\ K^{-1}$ | Machining properties | Magnetism |
|---|---|---|---|---|
| **Aluminum** | 1.000022 | 236* | 0 | paramagnetic* |
| **Brass** | 1.05 | 106* | ++ | paramagnetic* |
| **ABS** | - | 0.14-0.21** | ++ | - |

*(The National Physical Laboratory, 1995); **(Lasance, 2001); ***at 273.2 K;

**** Acrylnitrile-Butadien-Styrene-Copolymerisat

Custom built magnets (N50, 155 x 10 x 10 mm, Remanence (Nom) 1.47 T, Coercivity (Nom) 1035 kA/m) were purchased from ChenYang Technologies GmbH & Co. KG (Finsing, Germany) with a maximum working temperature of 80°C were used for all experiments.

## 2.7 Microfluidic reactor chips

Glass chips from Micronit were used for all experiments. The chips were custom build with 100 µm depth, single layer and 200 µm depth, double layer all glass, respectively. They feature cigar-shaped reaction chambers with comparable volumes (Figure 21), two inlets for two different fluids that end next to each other in the flow chamber and one outlet. Both chip layouts were wet etched microfluidic chips. The layout was developed in Solidworks® 2010/2011. The total internal volume of the 100 µm (200 µm) depth chip was 6.4 µl (7.36 µl) with a reaction chamber volume of

4.5 µl (4.66 µl). The outer dimensions of the chips were 45 mm x 15 mm. Detailed drawings of the chip can be found in chapter 3.3. As the outer dimensions of new reactor chips were not accurate, they had to be ground with sand paper carefully until they fit into the chipholder.

## 2.8 Reactor chip connection

The concept of the reactor setup involving magnetic beads within a microfluidic reaction chamber necessitates a reproducible filling of the microreactor with magnetic beads and a connection avoiding pressure pulses or air bubbles. Pressure pulses would result in washout of the beads prior to the experiment while air bubbles would press the beads out of the reaction compartment during the experiment. The connection protocol is explained using detailed images of the connection steps for one chip shown in Figure 13 and Figure 14.. For convenience the nomenclature of the subfigures **a** to **i** is continued for both figures. First the microfluidic chip was placed in the chip holder (Figure 13a). The reaction chamber was prefilled with immobilization buffer (see chapter 2.16) (Figure 13b_1) using a 1000 µL Eppendorf pipette. Next, immobilization buffer droplets were placed on all inlets and outlets of the microfluidic chip (Figure 13b_2 and c_2) using a 1000 µL pipette (Figure 13c_1). Afterwards a magnet (Figure 13d_1) was placed on the chip above the reaction compartment. Then the magnetic beads were inserted using an Eppendorf research pro electronic pipette (Figure 13e) with Eppendorf research pro pipette tips. Tips from other manufacturers resulted in unreproducible filling due to higher wall thickness and manufacturing tolerances. The pipetting speed of the pipette was adjusted to the lowest setting. The magnet was removed directly after bead filling (Figure 13f).

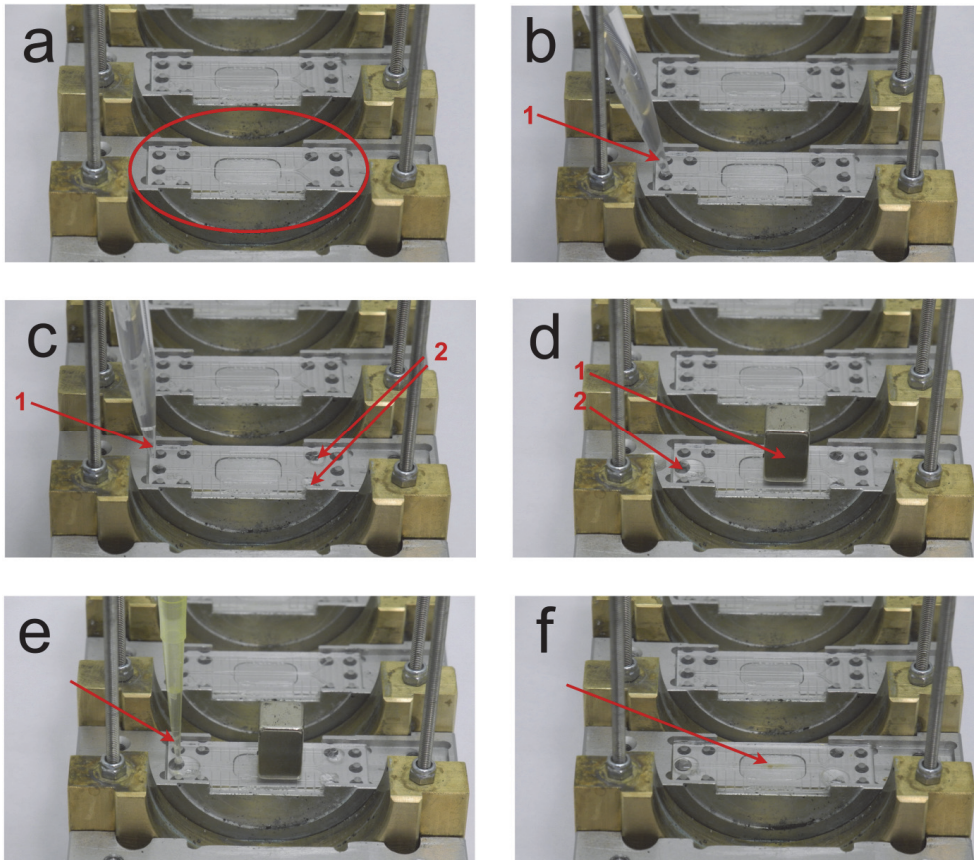


**Figure 13: Connection of the microfluidic chip part I. a:** Place microfluidic chip in chip holder **b:** Prefill microfluidic chip with immobilization buffer with 1000 µL pipette **c:** use 1000 µL pipette (1) to place immobilization buffer droplets on the two chip inlets (2),**d:** place magnet on microfluidic chip above reaction chamber (1) and place immobilization buffer droplet on chip outlet (2), **e:** use electronic Eppendorf pipette to fill magnetic beads into chip, **f:** remove magnet after filling of the chip with magnetic beads.

Now one magnetic mounting cylinder was placed in its mounting beside the microfluidic chip (g). Next the inlet tubing was connected to the Hamilton TLL1001 syringes containing the respective substrate solution using Idex/Upchurch 052P-659 and 052P-201 connectors. The outlet tubing was connected to a disposable plastic syringe. Subsequently, all tubing was prefilled either using the syringe pump, the syringe fine tuning adapter (chapter 3.5) (inlet) or the disposable plastic syringe (outlet). Afterwards the tubing ends to be connected to the chip were administered through the respective connection holes (Figure 14h 2+4) in the chip holder lid (Figure 14h_1) and a Micronit pro FFKM ferrule was placed ca. 5 mm from the end of each tube (Figure 14h_3). Then one droplet of substrate solution was pressed out of each tube prior to connecting it to the chip (Figure 14i). Finally the chip holder was carefully placed on top of the microfluidic chip (Figure 14j). By combining the droplets on the inlet of the chip and the tubing, an air bubble-free connection was established. Next the lid was pressed down by the four chip holder screws. First the inlet side (Figure 14k) and then the outlet side (Figure 14l) was screwed down. Transversal screwing down of the chip holder lid resulted in tilting and breakage of the chip during tightening of the screws.

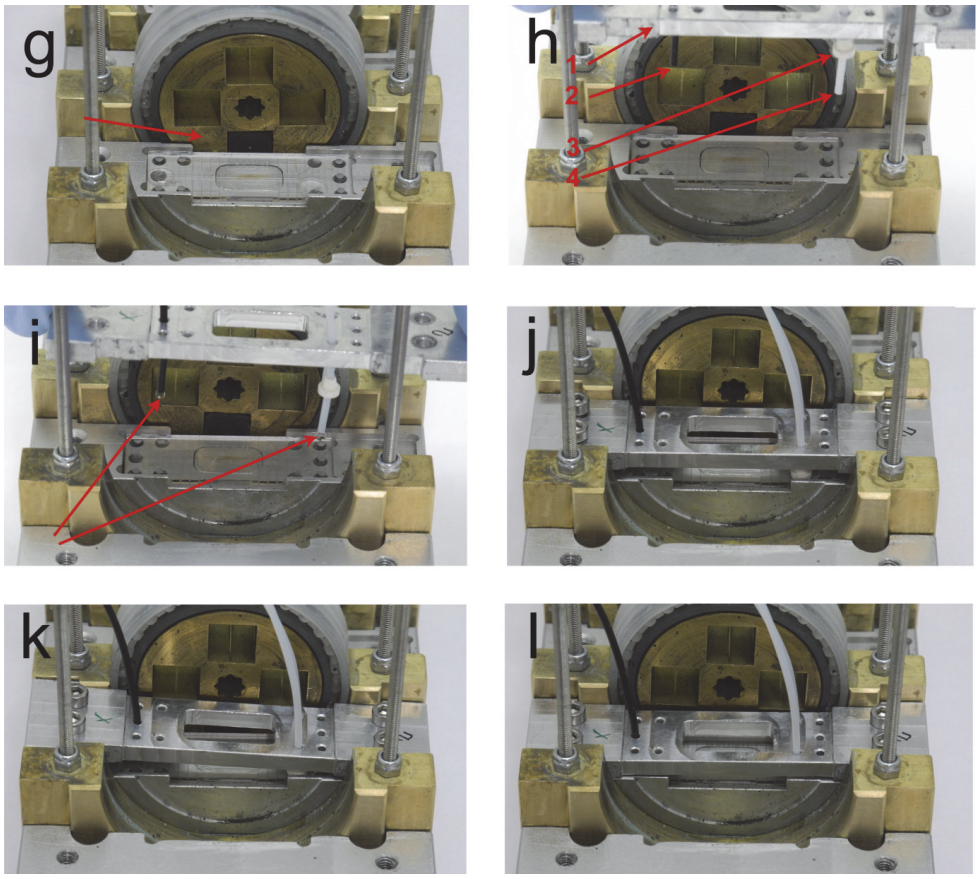


**Figure 14: Connection of the microfluidic chip part II. g:** place magnetic mounting with magnet beside chip holder h: place chip holder lid (1) with outlet tube (2) and inlet tube (4) with ferrules ca. 5 mm from chip**, i:** press one droplet out of inlet and outlet tubing with disposable plastic syringe (outlet)/syringe pump/syringe fine tuning adapter (inlet), **j:** carefully place chip holder on microfluidic chip joing the droplets on the tubing and chip to ensure air bubble free connection**, k:** carefully screw down inlet side of chip holder**, i:** carefully screw down outlet side of the chip for complete connection.

For all connections from the syringes to the reactor chip PTFE tubing (1/16 OD, 100µM ID) was used. For the connection from the reactor to the outlet or auto sampling unit PEEK tubing (1/16' OD, 100µM ID) or FEB (1/16' OD 10 µM ID) was used to decrease dead volume.

## 2.9 Dye distribution analysis

For characterization of the magnetic mixing system in the microfluidic reactor a rhodamine B solution (0-1 mg/mL in pH 6.5 Kpi buffer, in 0.1 mg/ml increments) was pumped through the chip and images were recorded with a Nikon D3100 Camera close to the outlet of the reactor (Figure 22). The color density signal was recorded from the green channel of the RGB images using Python 2.7. The Python script used for image analysis can be found in the appendix (chapter 7.1). For each of the positions analyzed along the chips width, a separate calibration curve was measured in order to minimize the effects of unequal light distribution in the microscope on the concentration determination of rhodamine B (Figure 22). For diffusion and mixing analyses each inlet of the chip was filled with 0.8 mg/ml and 0.4 mg/ml rhodamine B, respectively. Flow rates were adjusted by programming a profile into the pump prior to starting the device. A total volume of at least 10 µl was pumped through the system before taking the pictures for image analysis. In order to carry out multiple experiments in a row, a stepwise increase of the pump rate between 0.1 and 1.0 µl/min was combined with time lapse photography utilizing the DIYPhotobits camera control software.

## 2.10 Protein determination according to Bradford

**Preparation of Bradford solution (1L)**

100 mg Commassie brilliant blue G250 dissolved in 50 mL ethanol p.a.
100 mL phosphoric acid (85%)
Fill to 1L with water.

100 mg Commassie brilliant blue G250 were dissolved in 50 mL ethanol. After adding 100 mL phosphoric acid the solution was stirred for at least one hour. Afterwards the solution was filled with water up to 1 L. Next the Bradford solution was filtered and stored in light-protected bottles at room temperature. For protein determination bovine serum albumin was used as a reference for assay calibration. The assay was carried out using 10% v/v sample and 90% v/v Bradford reagent. For protein determination in 96-well microtiter plates (200 µl volume per well), 10 µL or 20 µL sample and 90/180 µL Bradford reagent were used whereas for photometric determination in half-micro cuvettes (volume 1.5 mL) 100 µL sample and 900 µL

Bradford reagent were used. Photometric measurements were carried out at 595 nm and room temperature after 5 min incubation without light exposure.

## 2.11 Cell disruption

***Cell disruption buffer***

50 mM potassium phosphate (Kpi)-buffer, pH 6.5
0.1 mM ThDP
2.5 mM magnesium sulfate

20 to 25 g of recombinant *E. coli* BL21 (DE3) cells with overexpressed of His- tagged wildtype BFD from previous projects were suspended in 100 mL of cell disruption buffer and sonicated using a Dr. Hielscher UP-200s sonifier in a cooled continuous-flow sonication device with. Sonication was carried out continuously for 3 x 5 min under constant cooling. Afterwards the crude cell extract was centrifuged for 15 min at 10000 g. The supernatant was stored at 4°C until it was used for protein purification (chapter 2.12).

## 2.12 Purification of BFD

Enzyme purification was performed using immobilized metal ion chelate affinity chromatography (IMAC) on $Ni^{2+}$-NTA agarose (Qiagen) as a stationary phase. Subsequently, the eluent was subjected to size exclusion chromatography (SEC) using Sephadex G25 (GE Healthcare). For all chromatography steps an ÄKTA system (GE Healthcare) was used.

***IMAC:***

***Equilibration/wash buffer***

50 mM Kpi-buffer, pH 6.5
0.1 mM ThDP
2.5 mM magnesium sulfate

***Wash buffer***

50 mM Kpi-buffer, pH 7.0
0.1 mM ThDP
2.5 mM magnesium sulfate

50 mM imidazole

***Elution buffer***

50 mM Kpi-buffer, pH 7.0

0.1 mM ThDP

2.5 mM magnesium sulfate

250 mM imidazole

**SEC:**

**SEC-buffer**

10 mM Kpi-buffer, pH 6.5

0.1 mM ThDP

2.5 mM magnesium sulfate

All buffers were sterile filtrated using an IImvac vacuum pump and degased either by sonification in an ultrasound bath for 15 min or by purging with Argon for 15 min per liter. Prior to each chromatography the $Ni^{2+}$-NTA column (diameter 26 mm), filled with ca. 25 mL Qiagen Ni-NTA Superflow was equilibrated with at least 5 column volumes of equilibration buffer. Subsequently, 100 mL crude cell extract (chapter 2.11) were applied onto the column using a superloop. After non-binding components were washed from the column, the wash buffer with 50 mM imidazole was used to remove non-specifically bound proteins from the column material. Finally BFD was eluted using the elution buffer. In order to remove the imidazole and decrease the salt content of the protein solution, a size exclusion chromatography was carried out. For this step a 1L Sephadex® G-25 column (inner diameter 50 mm, length 1000 mm) was equilibrated with 2L SEC-buffer. After the sample had been applied to the column it was rinsed with SEC-buffer until BFD was eluted. Afterwards the separated salt was washed off. Finally, both columns were washed with at least two column volumes of 20% v/v ethanol for storage. The activity of all purified enzyme batches was tested by measuring the BFD-catalyzed decarboxylation of benzoylformate (chapter 2.13). Purified BFD showed ca. 300 U/mg decarboxylase activity. All comparative experiments were carried out using the same batch of purified enzyme.

## 2.13 Decarboxylation assay for BFD

**Assay mixture**

50 mM Kpi-buffer, pH 7.0

0.1 mM ThDP

2.5 mM magnesium sulfate

5 mM Benzoylformate

0.25-0.35 mM Nicotinamide adenine dinucleotide (NADH)

0.25 U Horse liver alcohol dehydrogenase (HI-ADH)

The decarboxylation activity was measured using the BFD-catalyzed decarboxylation of benzoylformate to benzaldehyde. In order to amplify the signal of the assay it was carried out with an excess of NADH-dependent horse liver alcohol dehydrogenase (HI-ADH). HI-ADH catalyzes the reduction of benzaldehyde to benzyl alcohol while consuming NADH as a hydrogen donor. The consumption of NADH was measured photometrically at 340 nm. The assay mixture, except NADH, was prepared in a 50 mL reaction tube for numerous samples. Buffer, HI-ADH and benzoylformate were mixed and warmed to 30 °C. NADH was stored on ice and added 5 min before the measurement. Then the completed assay mixture was again incubated for 5 min at 30°C. Next the sample was pipetted into a cuvette/microtiter plate and the respective volume of assay mixture was added. For the activity assay in 96-well microtiter plates 20 µL BFD-sample and 180 µL assay mixture were used whereas for half micro cuvettes 50 µL BFD-sample and 950 µL assay mixture were used. The composition of the assay is described in detail in Table 3.

**Table 3: Assay mixture components of the BFD activity assay mixture**

| Component | Concentration | volume (half-micro cuvette ) [µL] | volume microtiter-plate [µL] |
|---|---|---|---|
| **assay buffer*** | 50 mM | 700 | 130 |
| **Benzoylformate**** | 50 mM | 100 | 20 |
| **NADH**** | 2.5- 3.5 mM | 100 | 20 |
| **HI-ADH**** | 5U/5.5mg/mL | 50 | 10 |
| **BFD** | - | 50 | 20 |

*50 mM (Kpi)-buffer, pH 7.0, 0.1 mM ThDP, 2.5 mM magnesium sulfate

**dissolved in assay buffer

## 2.14 Adsorption isotherm measurements for BFD on magnetic beads

To determine the adsorption isotherm of BFD on magnetic beads a ca. 10 mg/mL stock solution of the enzyme was prepared in immobilization buffer (see below) and the concentration was determined using the Bradford assay (chapter 2.10). Subsequently, the stock solution was diluted to 0.1 to 2.0 mg/mL BFD solutions. The protein concentration in all enzyme solutions was again determined using the Bradford assay. Subsequently, 10 µL of magnetic bead suspension were pipetted into a 96-well microtiter plate and 200 µL of the respective enzyme solution were added. The microtiter plate was then placed on the shaker unit of a Tecan pipetting robot for agitation for 10 sec. Afterwards, the beads were allowed to sediment for 5 min until all beads had accumulated on the bottom of the respective well. The shaking and incubation steps were then repeated twice. Then the beads were settled using a 96 well magnetic settling plate (Figure 15), and the supernatant was removed and analyzed using the Bradford assay (chapter 2.10). By comparing the enzyme concentrations before and after incubation with the magnetic beads, the bound enzyme fraction was determined.

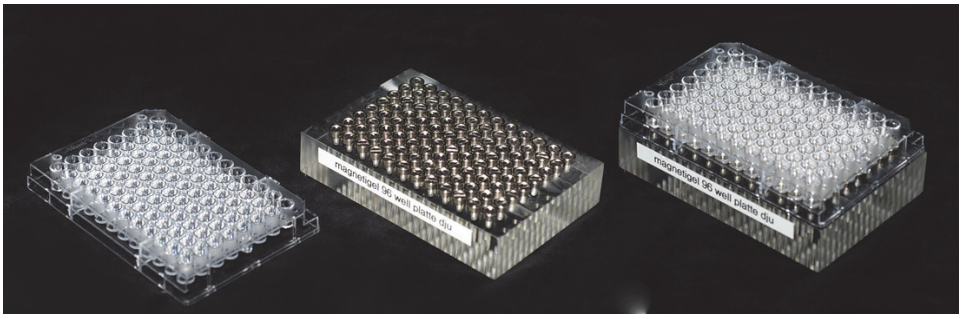


**Figure 15: 96-well settling plate for F96 standard microtiter plates.**

### Immobilization buffer

50 mM Kpi-buffer, pH 6.5

0.1 mM ThDP

2.5 mM magnesium sulfate

## 2.15 BFD immobilization for carboligation

For carboligation with BFD a stock solution of 1 mg/mL BFD was prepared as described in chapter 2.14 and diluted to 0.2 mg/mL with immobilization buffer (chapter 2.14). The final concentration was determined using the Bradford assay. 200 µL of this dilution were then added to 10 µL of the magnetic bead suspension in a 1.5 mL Eppendorf reaction tube. The beads were mixed with the enzyme solution by inverting the reaction tube and afterwards incubated for 15 min at room temperature. This step was carried out three times. Afterwards the beads were retained at one side of the tube using a magnet and the residual enzyme concentration in the supernatant was measured using the Bradford assay. Next, 1 mL buffer were added to the magnetic beads with bound BFD and the sample as stored at 4°C until it was loaded into the microreactor. Using this procedure 2 µg of enzyme per µL of PureProteome Nickel magnetic beads were immobilized reproducibly. Even though much higher enzyme loads are possible (chapter 3.8) a low enzyme load was chosen to minimize leaching of the enzyme from the beads (Nieba et al., 1997).

## 2.16 Carboligation experiments

**Reaction buffer 1**

50 mM Kpi buffer, pH 6.5-7.0
0.1 mM ThDP
2.5 mM magnesium sulfate

**Reaction buffer 2**

50 mM Triethanolamine buffer, pH 7.1- 8.0
0.1 mM ThDP
2.5 mM magnesium sulfate

For Kpi buffer the pH was adjusted with $H_3PO_4$ (1N, 2N or 20%) while the triethanolamine buffer was adjusted with HCl (1N, 2N or 20%). All pH-values were adjusted considering the reaction temperature, the buffer preparation temperature and the temperature-dependent pH shift of the respective buffers.

### 2.16.1 Substrate solution preparation

For all experiments at pH 6.5 to pH 7 were carried out in reaction buffer 1, while for reactions at pH values > 7 reaction buffer 2 was used (see above). All experiments were carried out with temperature control (±1°C). The buffers were degassed for 15 min using sonication before use. For the preparation of substrate solutions 90% of the total buffer volume was filled into a graduated flask (total volume 10 mL for microfluidic experiments, 2000 mL for bench scale experiments) and benzaldehyde and acetaldehyde were added using gastight Hamilton syringes. The properties of the respective chemicals are presented in Table 4.

**Table 4: Substrate properties (molar mass, density (20°C) and volume added for preparation of substrate solutions(20 mM, 30 mM, 40 mM and 50 mM benzaldehyde; 200 mM 300 mM 400 mM 500 mM and 600 mM acetaldehyde.**

| Substrate | molar mass g/mol | density (20°C) g/cm$^3$ | Volume added [µL/(mL × mM)] |
|---|---|---|---|
| **benzaldehyde** | 106.12 | 1.05 | 0.11 |
| **acetaldehyde** | 44.1 | 0.784 | 0.056 |

To ensure complete solution of the aldehydes in the respective reaction buffer, vortexing for 2 min or magnetic stirring was used. After the aldehydes were fully dissolved the rest of the respective buffer volume was added.

### 2.16.2 Carboligation activity test of immobilized BFD

50 µg BFD in 250 µL immobilization buffer were immobilized on 12.5 µL magnetic bead suspension as described in chapter 2.15. The beads were washed twice with 200 µL immobilization buffer for 5 min and then dispersed in 500 µL reaction buffer (pH 7.5 50 mM Kpi, 0.1 mM ThDP, 2.5 mM magnesium sulfate), resulting in an enzyme load of 50 µg/mL solution. 50 µL of these bead suspensions were then pipetted into 1.5 mL glass vials and 200 µL reaction buffer with 12.5 mM benzaldehyde and 250 mM acetaldehyde were added, resulting in overall initial concentrations of 10 µg/mL enzyme, 10 mM benzaldehyde and 200 mM acetaldehyde within the reaction vial. The vials were then placed in 15 mL falcon tubes and rotated on a rotator at room temperature for four hours. For each sample

one vial was removed and the reaction was stopped with 250 µL acetonitrile. The benzaldehyde- and (*S*)-HPP concentrations were analyzed by HPLC.

### 2.16.3 Carboligation activity test of free BFD

50 µg/µL free BFD solution was prepared. 50 µL of these bead suspensions were then pipetted into 1.5 mL glass vials and 200 µL reaction buffer (TEA pH 7.5, 50 mM Kpi, 0.1 mM ThDP, 2.5 mM magnesium sulfate) with 12.5 mM benzaldehyde and 250 mM acetaldehyde were added, resulting in overall concentrations of 10 µg/mL enzyme, 10 mM benzaldehyde and 200 mM acetaldehyde within the reaction vial. The vials were then placed in 15 mL falcon tubes and rotated on a rotator at room temperature for four hours. For each sample one vial was removed, the reaction was stopped with 250 µL acetonitrile. The benzaldehyde- and (*S*)-HPP concentrations were analyzed by HPLC.

### 2.16.4 Continuous carboligation with BFD in the micro scale reactor

To study BFD-catalyzed carboligation of benzaldehyde and acetaldehyde in the novel microreactor system, each substrate solution was filled in separate Hamilton TLL 1001 syringes. The carboligation was setup as described in 2.8). The microfluidic magnetic oscillation reactor (µMORE), as described in chapter 3.1, was used for the reactions. All experiments were carried out with 0.5 µL magnetic bead suspension carrying immobilized BFD. Immobilization of the enzyme to the beads was carried out according to chapter 2.15 whereas loading of the microfluidic chips with beads was carried out as described in chapter 2.8. If not otherwise stated the flow rate of all microreactor experiments was set to 0.4 µL/min (addition of both syringe pumps).

### 2.16.5 Bench scale continuous carboligation with BFD

Bench scale reference experiments were carried out in a 10 mL enzyme membrane reactor (EMR) made of stainless steel (Figure 14).This reactor consists of a reaction compartment with a stirrer disc with a magnetic core which is agitated by an IKA magnetic stirrer. Enzyme retention is achieved using an ultrafiltration membrane below the stirrer disc. The reactor was assembled completely. Then 10 mL BSA solution (1 mg/mL) in reaction buffer 2 pH 7.5were pressed into the reactor using a 10 mL disposable plastic syringe to prevent unspecific binding of the enzyme to the ultrafiltration membrane (Millipore 30 Kd, Ø 90 mm). The reactor was incubated with this solution overnight. Afterwards the reactor was washed with reaction buffer 2, pH 7.5, and 10 mL of a BFD solution (1 mg/mL), dissolved in immobilization buffer and prepared as described in chapter 2.14, were injected into the inlet of the reactor with a 25 mL disposable plastic syringe.

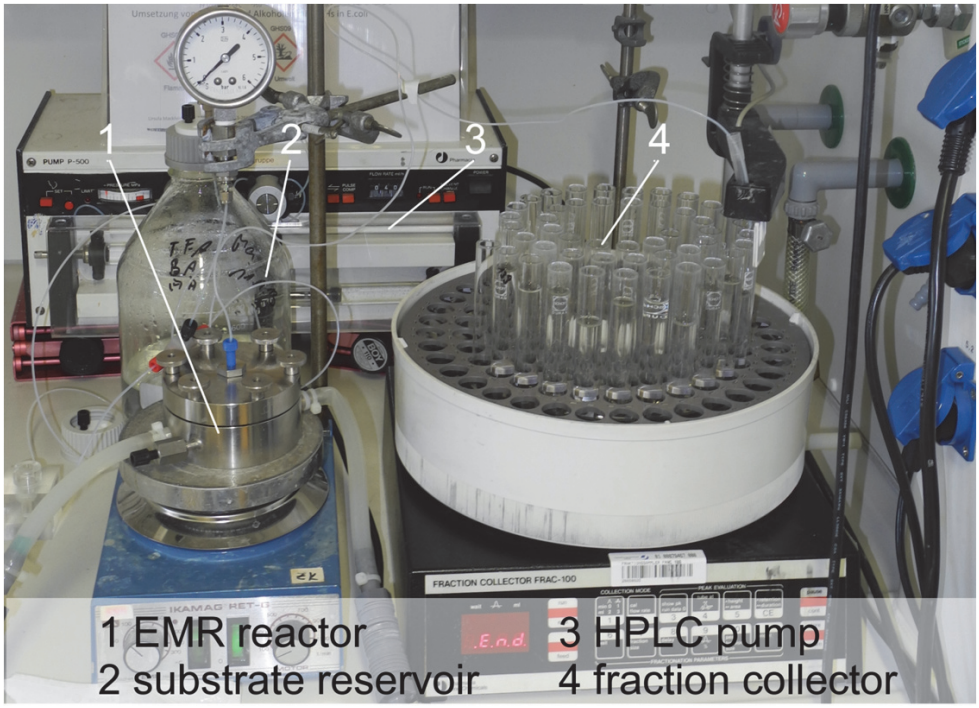


**Figure 16: Bench scale reference system for BFD-catalyzed carboligation.** 1: enzyme membrane reactor (inner volume: 10 mL); 2: substrate reservoir with benzaldehyde and acetaldehyde in reaction buffer 2, pH 7.5 (chapter 2.16.1); 3: HPLC pump; 4: fraction collector.

The reactor was started by starting the stirrer and the pumps, after prefilling the reaction compartment with substrate solution. The flow rate for these experiments was 40 mL/h and the stirrer frequency 300 rpm, respectively. The experiment was carried out three times (one reactor run could not be analyzed in detail due to sampling problems). Residence time was 15 min respectively and the fractions collected were 10 mL.

## 2.17 HPLC method

HPLC was used to identify and quantify substrates and products of the carboligation reaction of benzaldehyde and acetaldehyde. The microvials used by the fraction collectors integrated into the microreactor setup for automatic sampling of the continuous reactor samples were not compatible with the HPLC autosampler. Therefore, custom-build adapter tubes were used to fit the microvials into the autosampler of the HPLC system. The chromatogram was recorded using an Agilent/Hewlet Packard G1315A DAD detector and Chemstation software.

Column: Daicel Chiraltec ID column

**Program:**
Gradient: 35% acetonitrile (v/v) in dd$H_2O$
Flow: 0.9 mL /min
Injection volume: 1 µL; 5 µL; 10 µL
**Detection wavelength:**
λ = 200 nm for: PAC, HPP, Benzaldehyde, Benzoin
λ = 250 nm for: HPP, Benzaldehyde, Benzoin
**Retention time:**

| | |
|---|---|
| (*S*)-HPP | 7.6 min |
| (*R*)-HPP | 8.2 min |
| Benzaldehyde | 10.2 min |
| (*S*)-Benzoin | 14.5 min |
| (*R*)-Benzoin | 15.1 min |

# 3 Results & Discussion

## 3.1 Concept for the microfluidic magnetic oscillation reactor for enzymes (µMORE)

In order to achieve a well-mixed microfluidic enzyme reactor system, capable of mixing two separate substrate flows in a reaction chamber, an actuation system within the microfluidic system is imminent. Our reactor concept therefore incorporates immobilization of the enzyme on magnetic beads which at the same time are used as actuation system within the reaction chamber. Movement of the magnetic beads used for agitation is achieved by an oscillating magnetic field. Figure 17 shows the novel concept idea of the microfluidic magnetic oscillation reactor (µMORE) in comparison to the existing microreactor concepts laminar flow- and packed-bed reactor.

**Figure 17: µMORE concept (right) with the oscillating magnetic field symbolized by red arrows in comparison with previously published microreactor systems: laminar flow reactor (left) and packed-bed reactor (middle).**

In literature the use of electromagnetic fields for actuation has already been described, but these concepts could not be used for biocatalytic applications due to

the correlation of heat dissipation and magnetic field strength (Liu et al., 2011) (chapter 1.12). Initial ideas to generate oscillating magnet fields using permanent magnets, which avoid heating of the microreactor, lead to the development of a cylinder on both sides of the microfluidic channel in a chip reactor (Figure 18). In these cylinders up to four magnets per cylinder (n) can be placed. If all four mountings are filled with magnets (0°, 90°, 180°, 360°), they are placed in a staggered orientation by 45° between the cylinders. Depending on the application and the dimensions of the magnetic layout, the system may show increased performance with only one magnet per cylinder. The magnets have to be placed staggered and evenly distributed by X°. While X is defined as follows:

$$X = \frac{360}{n*2} \qquad \textbf{12}$$

By turning both cylinders simultaneously stepwise in a way that always one magnet is alternately placed beside the microfluidic chip, an oscillating magnetic field is generated. The µMORE concept is presented exemplarily in Figure 18 as a setup with only one magnet per cylinder. In first experiments this setup turned out to be most favorable, because magnetic field deviations were avoided, so it was used for all experiments in this thesis.

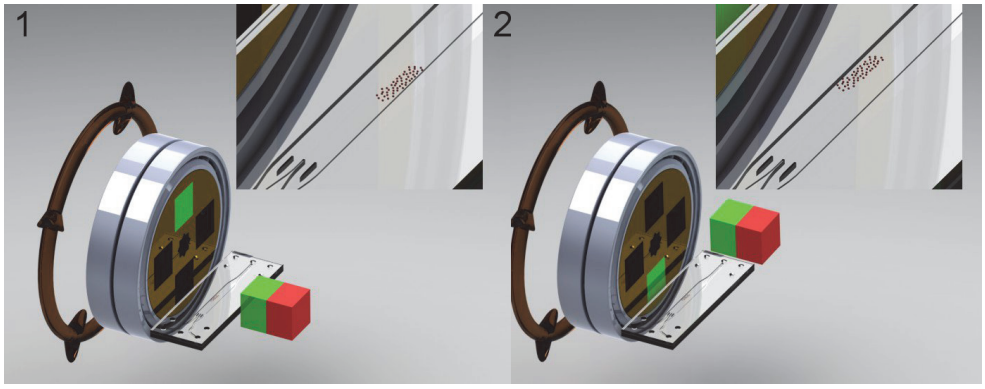


**Figure 18: Principle of the magnetic array for the µMORE.** Two cylinders with permanent magnets staggered by 180° in antiparallel orientation are placed on the left and right side of the chip (cylinder only shown on the left side). 1) In position 1 magnetic beads move to the right side, 2) in position 2 they move to the left side. Switching between the positions is realized by a 180° turn of the cylinders.

The µMORE concept allows for easy numbering up by adding microfluidic channels and cylinders in a way that always one chip is positioned between two cylinders resulting in n chips and n+1 cylinders for a respective multi reactor setup.

### 3.1.1 Material properties demands of the µMORE system

All materials for the µMORE reactor where chosen according to their magnetic, heat conductivity, corrosion resistance, and machining properties. While aluminum features excellent heat conduction coupled with slight paramagnetism, brass shows almost no magnetism and better machining properties. Therefore the magnet mounting cylinders and the cylinder mountings were constructed from brass while the main heat sink for temperature control was constructed from aluminum. For bearings plastic 61808 bearing with glass balls were used. Non-disposable parts from plastics were avoided to prevent damage by swelling due to contact with the aldehydes. Threaded bolts and screws used were made of stainless steel. Even though they exhibit light ferromagnetism, their location in the periphery of the reactor results only in a negligible influence on the magnet fields.

### 3.1.2 Dimensions of the magnetic agitation design

The dimensions of the microfluidic chips were limited to 15 x 45 mm standardized glass chips manufactured by Micronit in order to optionally use standard Micronit reactor chips such as the laminar flow reactor as a fallback position in case the novel setup would have failed. The axis for the magnetic agitation system (Figure 19, 1) is placed 13 mm above the chip base (Figure 19, 3). The magnets (Figure 19, 2) are placed with a 6.5 mm distance from the center of the respective cylinder. This assembly results in a configuration in which the base of the chip (Figure 19, 1) is placed 1.5 mm below the middle of the magnet to compensate for the glass plate at the base of the microfluidic chip. All magnets used for the system were 15 x 10 x 10 $mm^3$ N50 NeFeB magnets, magnetized along the 15 mm length. The distance between the magnet mounting and the microfluidic chips is 2 mm. An overview of the respective dimensions is given below (Figure 19). Detailed construction drawings of all parts can be found in the appendix.

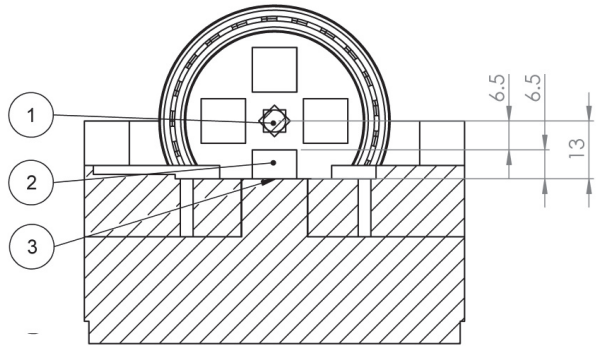


**Figure 19: Dimensions of the magnetic agitation design (section through the chip holder).**
1: axis of motor, 2: magnet, 3: chip holder base. All dimensions are provided in mm.

## 3.2 Test of the first µMORE prototype

The first microreactor setup was designed for investigation of bead movement and mixing characteristics by dye distribution as well as to test the handling of the microreactor and to gain first experience with the system. Therefore, a prototype of the µMORE system was constructed consisting of only one microfluidic chip plus two cylinders with magnets. The whole setup was integrated into a Nikon Diaphot microscope, which was equipped with a Nikon D3100 digital camera (Figure 20). The initial setup still shows stainless steel bearings (6), which were changed to plastic in for all experiments and the next version of the µMORE due to diversion of the magnetic fields.

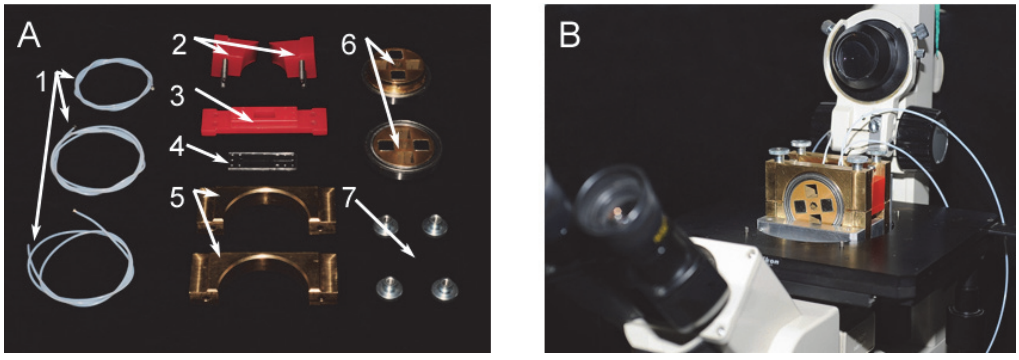


**Figure 20: First prototype of the µMORE for microscopic characterization of the mixing behavior.** A: 1: PTFE 1/16" OD 100 µM ID tubing; 2+3: First version of chipholder lid (2: spacer with

screw, 3 chip holder lid); 4: microfluidic chip; 5: upper bearing mounting; 6: magnetic agitation assembly (with two magnets and stainless steel bearing (later special nonmagnetic bearing and only one magnet per array were used); 7: thumb screws for bearing mounting; B: assembled microfluidic reactor on the microscope.

## 3.3 Microfluidic chip prototyping and characterization

During the course of this thesis two different designs were tested with the μMORE concept. Both designs basically consist of a Y-shaped channel layout with two inlets, a reaction chamber and one outlet (Figure 21). The first design (chip 1), has 100 μm channel depth, a 2150 μm wide reaction chamber and a total volume of 6.4 μL. It was used for development of the dye distribution experiments (chapter 3.3.1; Figure 23) and was afterwards characterized (chapter 3.3.2). The second microfluidic chip layout (chip 2) was developed as an optimized design based on the results obtained with chip 1. Chip 2 features a 1250 μm wide and 200 μm deep reaction chamber. It has the same general Y-shaped layout as chip 1 and an internal volume of 7.36 μL. In order to validate the method used for dye distribution the diffusion based dye distribution without magnetic beads generated with the second chip was exemplarily compared with computational flow dynamics simulations (chapter 3.3.1; Figure 24).

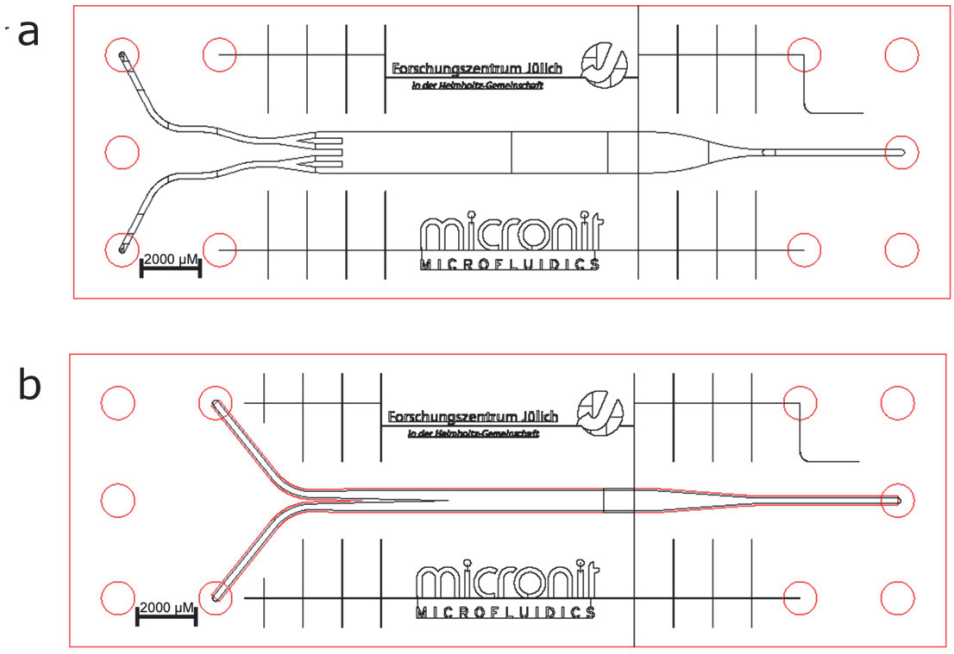


**Figure 21: Microfluidic reaction chips used for this thesis.** a: **Chip 1;** 2150 µm reaction chamber width, 100 µm depth; internal volume 6.4 µL; cross sectional area of reaction chamber 0.215 $mm^2$, surface area 139.95 $mm^2$; b: **Chip 2**; 1250 µm reaction chamber width, 200 µm depth internal volume 7.36 µL; cross-sectional area of reaction chamber 0.250 $mm^2$; surface area 92.54 $mm^2$.

### 3.3.1 Validation of dye distribution reactor characterization

In order to validate the mixing behavior of two laminar flows in the µMORE, a number of dye distribution experiments were carried out in the first microfluidic chip prototype utilizing a Nikon Diaphot microscope and a Nikon D3100 digital camera according to chapter 2.9. The concept is summarized in Figure 22.

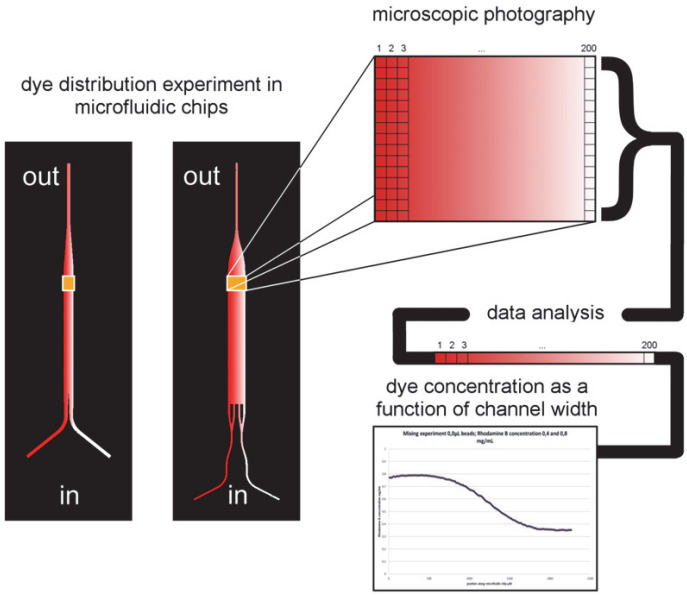


**Figure 22: Schematic explanation of the dye distribution analysis system used to characterize the magnetic mixing system in the microfluidic chip.** Left: 200 µm depth chip 1; right 100 µm depth chip 2. Measurements were performed in the marked area close to the outlet of the reaction chamber (yellow).

The different pixel colors were evaluated for their sensitivity and linearity concerning the concentration detection for the rhodamine B dye used. The data presented in Figure 23 exemplarily depicts the average pixel readout within the measuring window of the three different colors of an RGB .jpeg picture taken within the measuring window (Figure 22) with different rhodamine B concentrations pumped through chip 1.

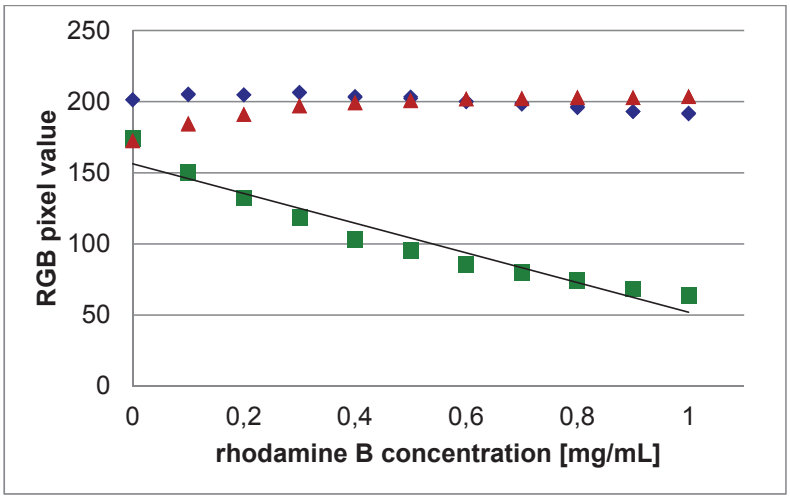


**Figure 23: Validation of pixel readout for dye distribution experiments.** R: red pixel readout; B: blue pixel readout; G: green pixel readout; linear function for green pixel readout: y=-104.29x + 156.29; $R^2$= 0.9329.

While the red and blue pixel signals did not show any correlation with the dye concentration, a clear correlation was found between the green pixel readout and the dye concentration. This may seem odd as we use a red dye. However, the concept of the RGB color space (chapter 1.14) explains the underlying relationships. Due to unstable illumination conditions in the microscope, it was necessary to subtract the background signal in order to compare different datasets. The Y axis intercept in Figure 24 was adapted by auto zeroing the average signal ($s_{avg}$) to the known average rhodamine B concentration ($c_{avg}$ = 0.6 mg/mL) within the measuring window of the microfluidic chip (see equation 13).

$$\boldsymbol{c_{avg} = 0.6\ mg\ mL^{-1} = a\ s_{avg} + b_{cor}} \qquad \textbf{13}$$

Then the corresponding dye concentration within the microfluidic chip at a certain location along the width within the measuring window was calculated according to equation 14, based on the slope (a) generated by calibration with rhodamine B of the green pixel signal from the respective spot (s) and the Y intercept ($b_{cor}$).

$$\boldsymbol{c = a\ s + b_{cor}} \qquad \textbf{14}$$

The method was verified by COMSOL® computational fluid dynamic (CFD) simulation of the diffusion based dye distribution of 0.4 mg/mL and 0.8 mg/mL

rhodamine B using chip 2 (Figure 24) at a flow rate of 0.4 µL/min. No magnetic particles were introduced at this point as CFD simulation for complex systems such as chaotic mixing was not available (chapter 1.9). It can be seen that the simulation provides a good description of the experimental data. Slight differences between the CFD-simulation and the experimental data at the edges of the channel may be caused by inhomogeneity in the chips surface or pulsing of the syringe pumps used.

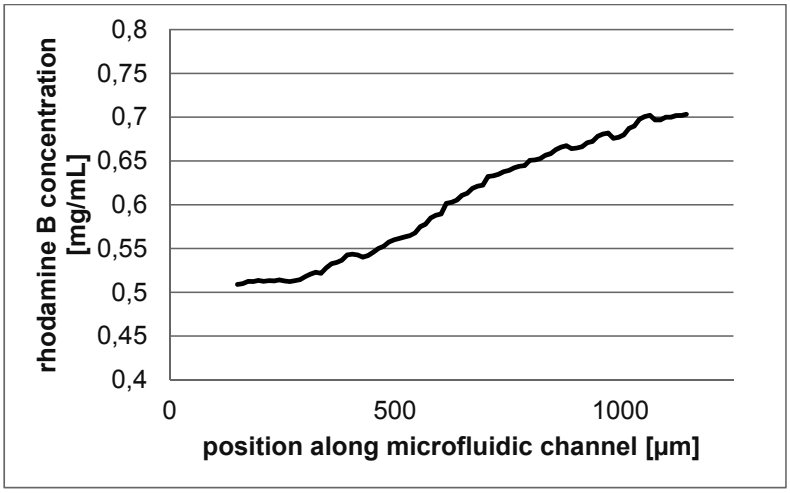


**Figure 24: Exemplary comparison of dye distribution data for diffusion based rhodamine B mixing (solid line) according to the setup shown in Figure 22 (flow rate 0.4 µl/min, normalized dye distribution data) and COMSOL computational fluid dynamic simulation (dashed line). Complete mixing would result in a horizontal line.**

### 3.3.2 Dye distribution characterization of chip 1

In order to characterize the mixing and bead retention in reactor chip 1 (Figure 21) the dye distribution method (chapters 1.14, 2.9, 3.3.1) was applied for reactor characterization. The flow rate was increased stepwise between 0.1 µL/min and 1.0 µL/min. Furthermore 0.125 µL, 0.25 µL, and 0.5 µL magnetic bead suspension were used to determine the mixing characteristics with different bead loads. For each setup the frequency of the magnetic field oscillation was set such that all beads would just travel from one side of the chip to the other. For chip 1 (Figure 21) this maximum frequency was 0.05 Hz for all tested magnetic bead loads. First the diffusion-based mixing within the reactor without magnetic beads was investigated as a reference. Figure 25a depicts the dye concentration at the end of the reaction

chamber for only diffusion based transport under laminar flow conditions in the reactor as a 3D plot of the rhodamine B concentration, the position along the width of the chip and the flow rate. In Figure 25b to Figure 25d the same plot is presented for different magnetic bead loads (0.125, 0.25 and 0.5 µL) using the magnetic bead agitation system.

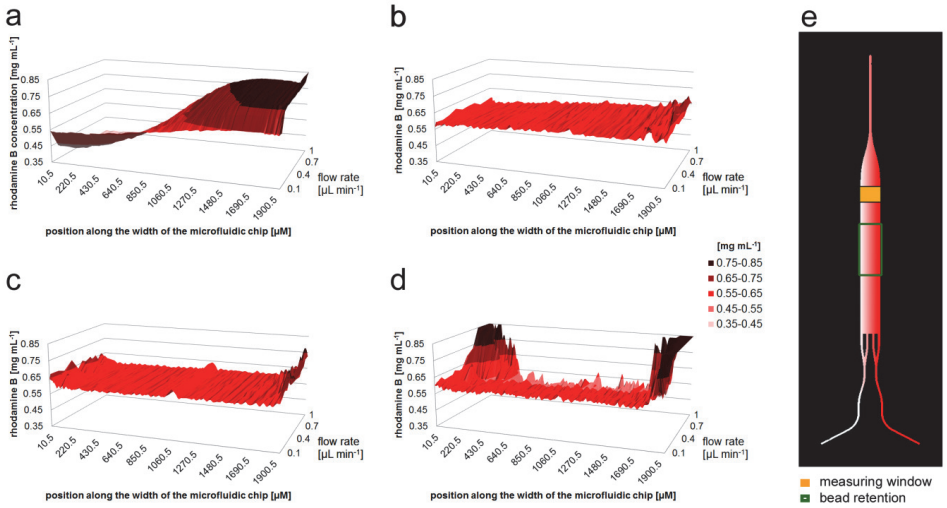


**Figure 25: Dye distribution data of the first microreactor prototype.** Dye distribution at the end of the first microfluidic chip: a: without magnetic bead suspension, b: with 0.125 µL magnetic bead suspension; c: with 0.25 µL magnetic bead suspension, and d: with 0.5 µL magnetic bead suspension, e: Design of chip 2 with bead retention area (green) and measuring window (orange).

In all measurements with particles (Figure 25 b-d) noise of the signal can be seen due to magnetic beads which were sluiced out from the magnetic bead retention zone (Figure 25e, green box) into the measuring window of the microscope (Figure 25e, yellow marking) during filling of the microfluidic chips. As long as the magnetic bead retention force is stronger than the force applied to the beads by their flow resistance, these artefacts are static. Therefore, they do not impair the validity of the data. As soon as washout of beads occurs an increase of these artifacts, especially on the sides of the channels, can be seen. The data presented in Figure 25 thus shows that the dye distribution method applied is restricted to flow rates at which no washout of the beads occurs. As a result, increasing amounts of beads within the measuring window impair the measuring. The artifact shown in Figure 25C at ca.

900 µm is an example for beads stuck in the measuring window during filling of the reactor, while the noise increase at 1900 µm is an example for increasing noise due to washout. Additionally the washout was analyzed using the image raw data. While complete mixing does not even occur at flow rates as low as 0.1 µL/min for the diffusion based mixing, agitation of the magnetic beads in the µMORE system allows for complete mixing up to flow rates of 1.0 µL/min. However, the noise at the left and right edge of the measuring window indicates that bead washout occurs already at flow rates as low as 0.3 µL/min. With regard to the flow properties in the µMORE with magnetic beads, the question whether there is complete laminar flow or some degree of turbulence within the microfluidic reaction compartment where the beads are moving can currently not finally be answered. Swirls have been observed microscopically behind the beads when different dye concentrations in the one flow were mixed, suggesting at least some turbulence in the reaction compartment. However, a simulation of the mixing or a model for determination of the Reynolds number, and thus characterization of the flow behavior, is not possible. Further investigation on this subject therefore provides an interesting challenge for future research. Even though complete mixing along the width of the reactor was achieved, it has to be noted that a concentration gradient along the length of the mixing zone/reaction chamber may persist!

### 3.3.3 Magnetic modelling of chip 1

In order to draw conclusions from the performance of microfluidic reactor chip 1 (Figure 22) magnetic field simulation was utilized. While the magnetic holding force depends on the flux density gradient in the direction of flow, the particle movement is forced by the oscillating flux density gradient along the width of the channel. Additionally, the holding force for a given particle is dependent on the magnetization and size of the respective particle (chapters 1.8 and 1.12). The flux density gradients along two exemplary axes along the microfluidic chip 1 are depicted below. The flux density gradient along the width of the chip, measured in the middle of the mixing zone, shows that the flux density gradient decreases with increasing distance from the magnet (Figure 26a). Additionally Figure 26b shows that there is a region (middle ca. 4 mm along the length of the chip; green marking) with a maximum flux density gradient along the direction of flow. Outside this middle 4 mm of the chip the flux density gradient rapidly declines. It was microscopically observed that the particles

were oscillating within this area below the washout flow rate of 0.3 µL/min (chapter 3.3.2).

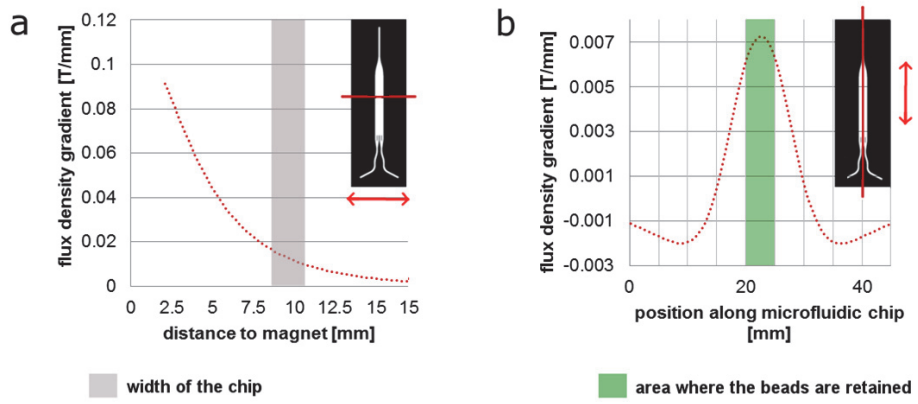


**Figure 26: Magnetic flux density gradient simulation along the width and length of the microfluidic chip 1.** The pictogram in the upper right corner of each diagram indicates the axis (red line) along which the field gradient was measured; the direction of the gradient is visualized by red arrow. a: flux density gradient along the width of the microfluidic chip as a function of distance to the magnet; the grey area indicates the channel of chip 1. b: flux density gradient along the length of the microfluidic chip 1; green area indicates the mixing zone in which particles are present below the washout flow rate.

The magnetic flux density gradient simulation was used to visualize the magnetic field distribution within the chip in order to optimize the chip design accordingly. While the magnet is placed on the left side of the microfluidic chip, as shown in Figure 27, it can clearly be seen that the magnetic flux density gradient is not constantly distributed over the width of the reaction chamber and gradually declines with increasing distance to the magnet. The green box represents the area with the highest mean magnetic flux density gradient across the cross section of the reactor. While on the left channel edge (where the magnet is positioned) a flux density of >0.9 T is prevalent the gradual decrease over the width of the microfluidic chip results in a flux density of only 0.65 - 0.6 T on the right side. This anisotropy of the magnet field may cause the leakage of the beads at the reaction chamber side where no magnet is positioned. As the bead retention within the reaction compartment is limited by the magnetic force applied to the beads, the results of the dye distribution measurements with this first prototype (chapter 3.3.2) clearly indicate

that the magnetic field was not sufficient to retain the beads within the reactor mixing zone at flow rates higher than 0.3 µL/min. As the magnets used in the current design are already N50 NiFeB magnets with a remanence of 1.47 T (chapter 2.6), a further increase of the magnetic force is only possible by using Cobalt iron alloys (The National Physical Laboratory 1995). However, due to limited availability of these magnets, this was not an option.

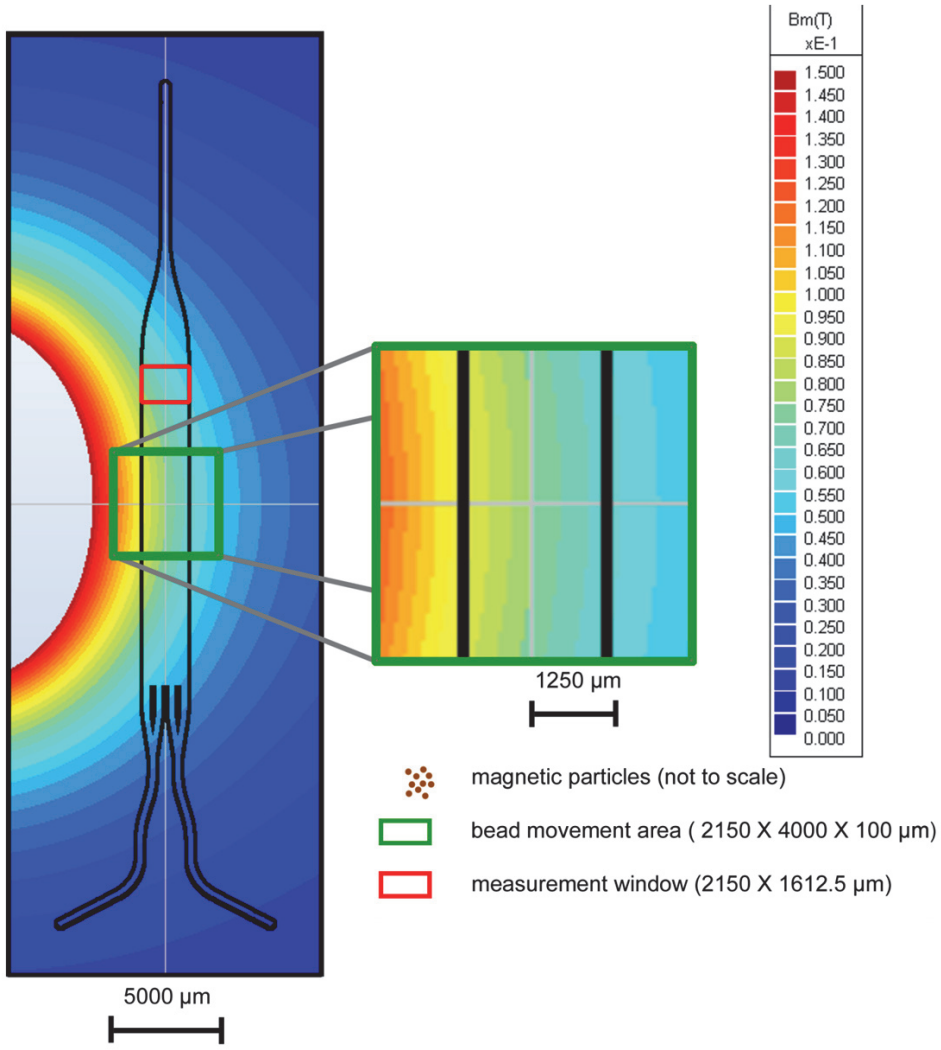


**Figure 27: Magnetic flux density within chip 1.** including a magnification of the mixing zone with magnetic beads in the middle of the microfluidic channel (green) and the measurement window for the dye distribution measurement (red) (for chip measurements please refer to Figure 21).

To solve the washout problem it was considered next to use larger magnetic beads. However, the magnetic moment defining the holding force of the beads varies depending on the manufacturer. Therefore the relation of volume/retention force versus flow resistance (chapter 1.8) is at this point not the only affecting factor. Additionally, larger beads could cause problems to fill the reactor reproducibly due to

clogging and increased effects of diffusion based transport within the beads. An increase in bead size was thus ruled out for further optimization. Instead the design of the microfluidic chip was reconsidered. As Figure 27 and Figure 26 clearly show, the area with the lowest magnetic flux density within the mixing zone (green box) is at the side of the chip not facing the magnet. Removing this part of the chip would be beneficial for bead retention. A smaller width of the chip would therefore solve the washout problem by achieving a higher minimum flux density/flux density gradient within the mixing zone. A simulation of the bead washout was considered, however this plan was abandoned due to lack of detailed information about the beads magnetic moment and the complications of modelling the flow in complex systems such as chaotic mixing (chapter 1.9).

### 3.3.4 Development of chip 2

Based on the dye distribution results of chip 1 the second microfluidic chip (chip 2) was designed. The main idea of the optimization was to decrease the width of the microfluidic channel in order to increase the minimum magnetic flux density as well as the mean magnetic flux gradient in order to achieve higher flow rates without bead washout. However, the flow resistance of a bead is a function of the flow velocity (distance/time) and not of the flow rate (volume/time) (chapter 1.7). A simple decrease in the width of the microfluidic channel would cause a decrease in the chips cross sectional area resulting in a higher flow velocity for a given flow rate. Thus, a decrease of the channel width without increasing the flow velocity for a given flow rate can therefore only be achieved by increasing the depth of the microfluidic channel at the same time. Therefore the thickness of the channel was increased from 100 µm (chip 1) to 200 µm (chip 2, Figure 21), while the width was decreased from 2150 µm (chip 1) to 1250 µm (chip 2). Thereby the cross sectional area of the reaction compartment was increased from 0.215 $mm^2$ to 0.25 $mm^2$ resulting in a decrease of the flow velocity of 16% for any given volumetric flow rate. Furthermore, the channel surface was decreased from 139.95 $mm^2$ to 92.54 $mm^2$, which should decrease magnetic bead adhesion to the chip surface (Figure 21).

### 3.3.5 Magnetic field simulation of chip 2

In Figure 28 the layouts of chip 1 and chip 2 are shown, overlaid with the magnetic flux density. It can clearly be seen that the minimum magnetic flux density within the mixing zone (right edge of channel) in the new design with 0.65 T to 0.7 T is higher than in the respective zone in chip 1 (<0.60 to 0.65 T). These results are in agreement with the design aims of chip 2 as stated in chapter 3.3.3.

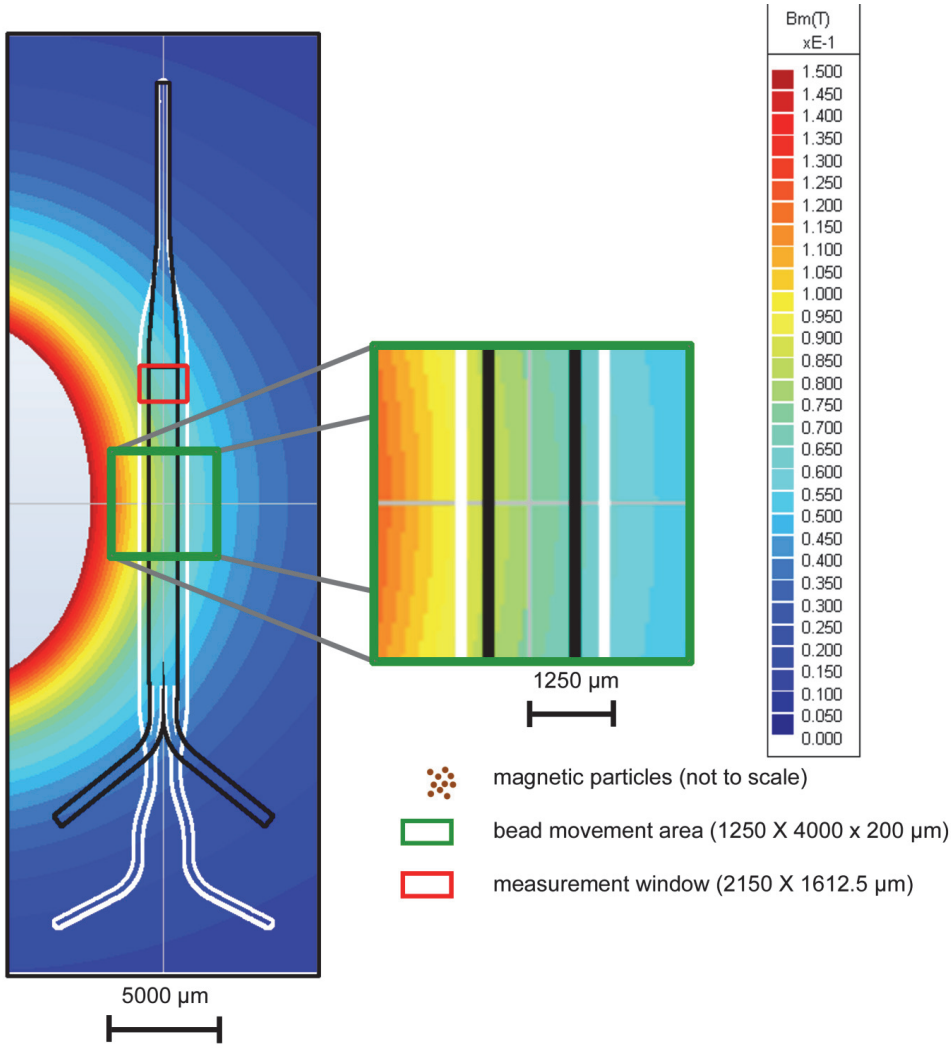


**Figure 28: Simulation of the magnetic flux density for chip 1 (white) and chip 2 (black)** including a magnification of the mixing zone with magnetic beads in the middle of the microfluidic channel

(green) and the measurement window for the dye distribution measurement (red) (for chip measurements please refer to Figure 21).

### 3.3.6 Dye distribution characterization of chip 2

Chip 2 was characterized identically to the first design using flow rates between 0.1 and 1.0 µL /min. Again the magnetic oscillation frequency was set to the highest frequency at which all beads move from one side of the chip to the other. Due to the decreased travel distance the oscillation frequency could be doubled from 0.2 Hz to 0.4 Hz compared to the first chip design. Furthermore, in contrast to the first chip design the maximum magnetic oscillation frequency increased proportionally when the amount of beads was decreased. The oscillation frequencies for all setups are presented in Table 5.

**Table 5: Oscillation frequency for the dye distribution experiment of chip 2 (for chip dimensions please refer to Figure 21).**

| Bead load (µL) | Oscillation frequency [Hz] |
|---|---|
| **0.125** | 0.4 |
| **0.25** | 0.2 |
| **0.5** | 0.1 |

As shown already in Figure 25 for the first chip design, the mixing behavior was again studied with the new chip design (Figure 28) using the two rhodamine B solutions. The results without beads and with different bead loads are depicted in Figure 29. First of all it can clearly be seen that at a flow rate of 0.1 µL/min the diffusion based mixing (Figure 24 A) resulted already in an almost completely homogenous dye distribution along the width of the channel. This is due to the decreased width of the reaction chamber. In presence of the magnetic beads (Figure 25 B-D), one can clearly see that the washout of beads was greatly minimized compared to the results with the first chip design in Figure 21. Washout of beads was now only observed at flow rates higher than 0.7 µL/min, whereas in the first chip design it occurred already at 0.3 µL/min. Additionally, the smaller bead travelling distance between the left and right side of the reactor and the decreased surface interaction due to the decrease of the chips surface area, resulted in higher oscillation frequencies (Table 5).

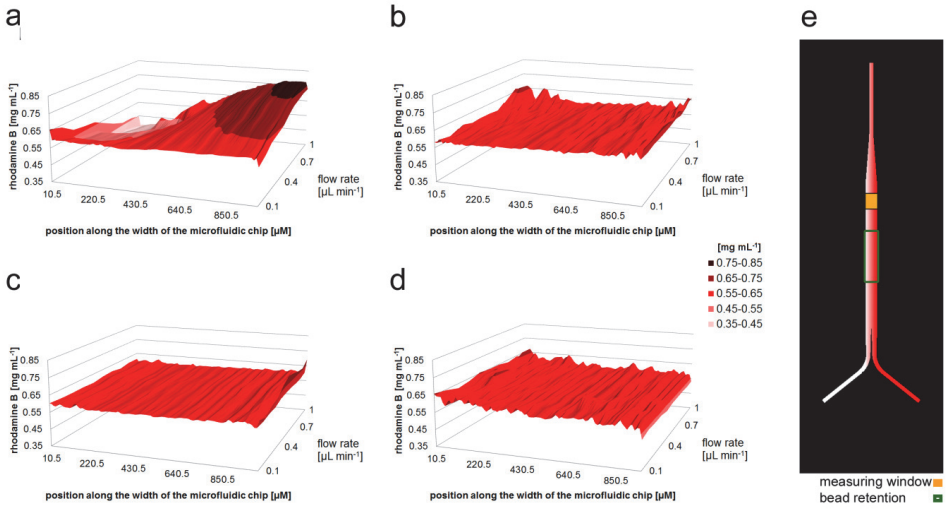


**Figure 29: Dye distribution data of the optimized microfluidic chip layout.** a: dye distribution at the end of the optimized microfluidic chip without magnetic beads, a: dye distribution at the end of the optimized microfluidic chip with 0.125 µL magnetic bead suspension, c: with 0.25 µL magnetic bead

suspension, and d: with 0.5 magnetic bead suspension, e: overview of chip 2 with bead retention area (green) and measuring window (yellow).

After proof of principle for the novel mixing system the µMORE system was subsequently further developed and optimized for biotransformations (chapter 3.4 and 3.5).

## 3.4 µMORE reaction system

The second microreactor system was designed with the aim to set up a parallelized micro reaction system with six microfluidic chips. Two threefold reactor blocks, each with three parallelized chips were incorporated into a Ditabis TK23 laboratory heating cooling device for temperature control and two Landgraf six-fold syringe pumps were employed for parallelization of the reactor. Each reactor block had a dimension of 128.5 x 85.5 mm, respectively. A detailed exploded view of one reactor block is presented in Figure 30.

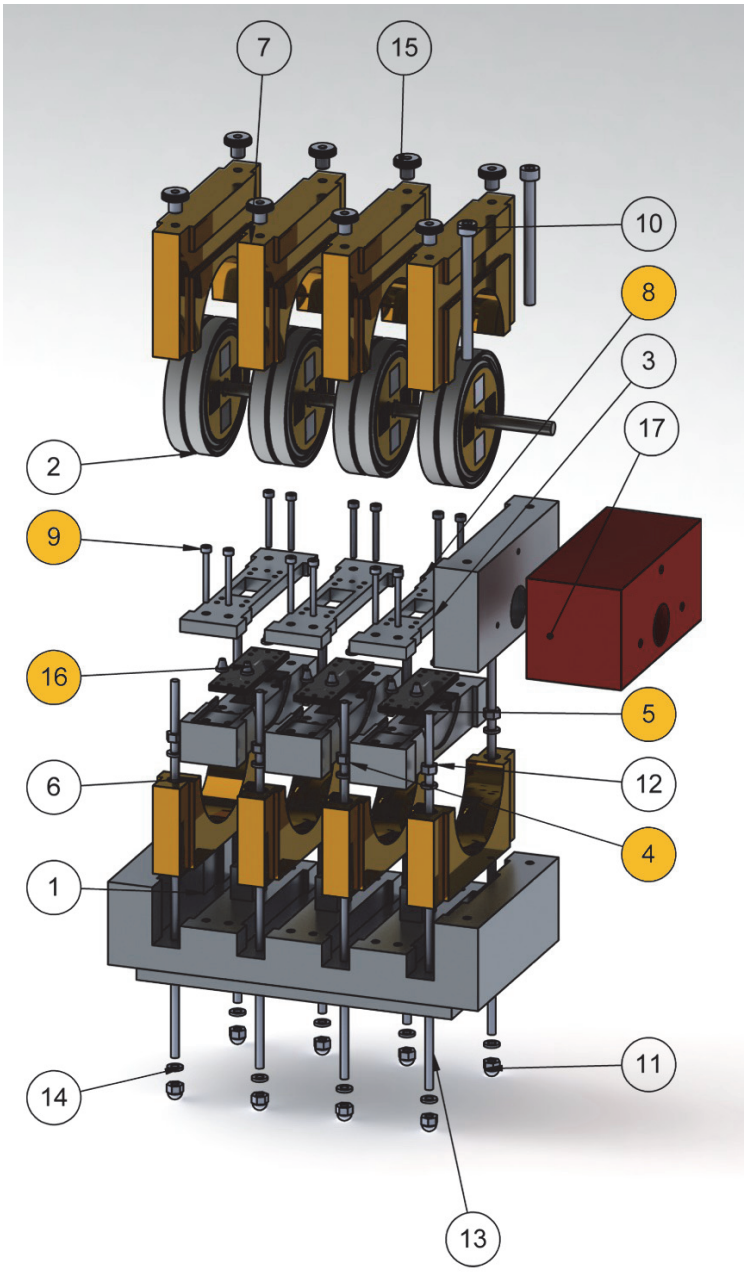


**Figure 30: Exploded view of a µMORE threefold reactor block. 1:** base of reactor block, **2:** axis with magnet mountings, **3**: motor mounting, **4**: bottom chip holder, **5**: microfluidic chip, **6**: bottom bearing mounting, **7**: top bearing mounting, **8:** chip holder lid, **9**: screw M1 x 20, **10:** screw M4 x 50, **11**: domed nut M3, **12**: nut M3, **13**: threaded bolt M3, **14**: washer M3, **15**: thumbscrew M3, **16**: Micronit pro ferrule, **17**: motor mounting spacer.

This system constructed for enzyme catalysis has a few differences compared to the initial setup (chapter 3.2). The first difference is the numbering up of the chips. Instead of a viewing window in the bottom chip holder and the chip holder lid for the light path of the microscope the threefold system features only a window in the top chip holder lid (Figure 30_**8**) for visual air bubble detection. Further, the base of each reactor block is a solid aluminum block for optimal heat conductivity (Figure 30_**1**). On this block three modular removable chip holders (Figure 30 yellow marked assembly) are placed. The reaction chamber for optimal temperature control of each chip is directly above a pistil on the base of the reactor block (Figure 30_**1**). This pistil fits into an opening in each of the three modular chip holders.

Both three-fold reactors were placed on a Ditabis TK 23 laboratory heating/cooling block (Figure 31_**3**). The inlets were connected to Landgraf LA 160 syringe pumps (Figure 31_**2**) while the outlets were connected to a BasiInc honeycomb micro fraction collectors (Figure 31_**4**). The whole µMORE system including periphery is presented in Figure 31. All construction drawings of the reactor system can be found in the appendix.

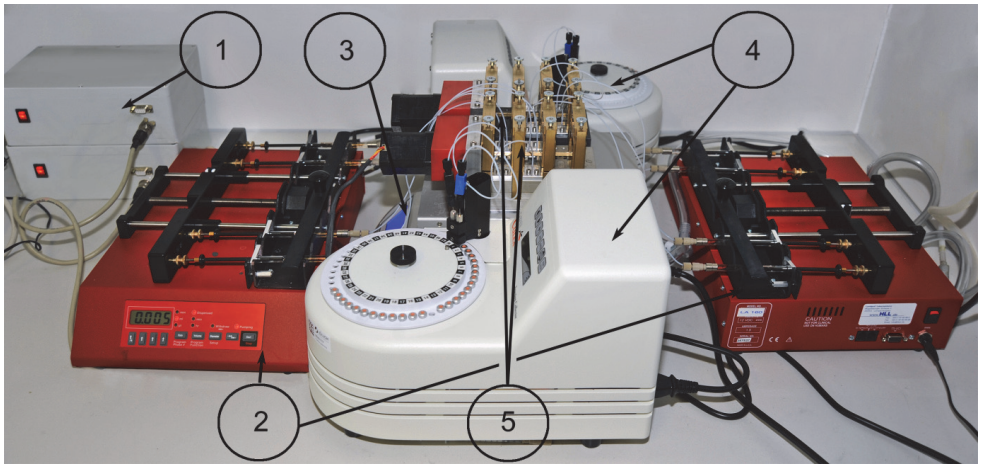


**Figure 31: Complete reactor assembly. 1:** Motor control; **2:** LA 160 Syringe pumps**; 3:** Ditabis TK23 heating/cooling block; **4:** BasiInc Honeycomb micro fraction collectors; **5: t**wo threefold µMORE systems (two chips per block connected).

## 3.5 Optimization of the µMORE prototype

While the chip was optimized successfully during prototyping, a number of drawbacks in the reactor holder were observed. First, the current design was not able to provide reproducible connection with standard 1/16' HPLC tubing which resulted in leakage and breaking of the expensive microfluidic chips. Furthermore, it was observed that polypropylene plastic was not a suitable material for the chip holder lid because of bending. Additionally, the reactor lid consisting of three pieces (Figure 20a 2+3) was unpractical and the M3 threaded screws used had a too high thread slope to connect the fragile glass chips. Finally it was observed that heat generation of the motor that drives the magnet cylinders may become a problem due to the temperature sensitivity of enzyme catalyzed reaction. Therefore, the respective mounting motor spacer (Figure 30 **17**) was manufactured from ABS instead of aluminum. It also became clear that removable modular chip holders are necessary for maintenance and reproducible setup of a 3-fold reactor holder (Figure 30, yellow marked parts). Finally, it was observed that a pre-installation of the magnetic agitation unit prior to filling the chips was not feasible due to the fact that a permanent magnet placed directly on top of the microfluidic chip was necessary to ensure bead retention during filling operation (Figure 13 and Figure 14). Therefore the chip holder lid was further optimized to enable easy installation of the magnetic mountings during chip connection.

### 3.5.1 Optimization of the microreactor chip connection

The chip holder lid was continuously adapted in order to ensure an easy leak-tight connection of the microfluidic chip with macro size 1/16 HPLC tubing (micro to macro connection). The different versions of the chip holder are depicted as exploded view in Figure 32a. For connection, a ferrule placed at the end of the 1/16" tubing is pressed down with the reactor lid. Thus, the ferrule is deformed around the tubing and a connection between the tubing and the microfluidic chip is accomplished (chapter 2.8). Initially one of the main problems was that these connections were prone to leak and that the pressure applied could not be controlled. Figure 32b shows the cross section along a macro to micro connection of the first chip holder lid (Figure 32.1). The bulky design with space for the axle of the magnetic actuation system (Figure 32.a.7) also proved to be unpractical for setting up the system,

especially as it turned out that motor and axle should be attached to the reactor as the final step, after loading the chip with magnetic beads and connecting it to the tubing. However, the main problem of the first chip holder lid was that the space between the microfluidic chip and the chip holder bottom cannot be set reproducibly as there is no fence between chip holder lid surface (red line) and chip holder bottom surface (blue line) when the connection is established. Therefore the pressure on the ferrule and the chip cannot be controlled reproducibly with this design. This resulted in tilting and consequently in destruction of the expensive microfluidic chips. Thus, an alternative chip holder lid was developed to compensate the drawbacks of the first design. In the new design (Figure 32c) the maximum pressure applied on the microfluidic chip is defined by a fence between the chip holder lid (Figure 32c red line) and the chip holder bottom (Figure 32c blue line) once a defined distance of 2.0 mm is reached.

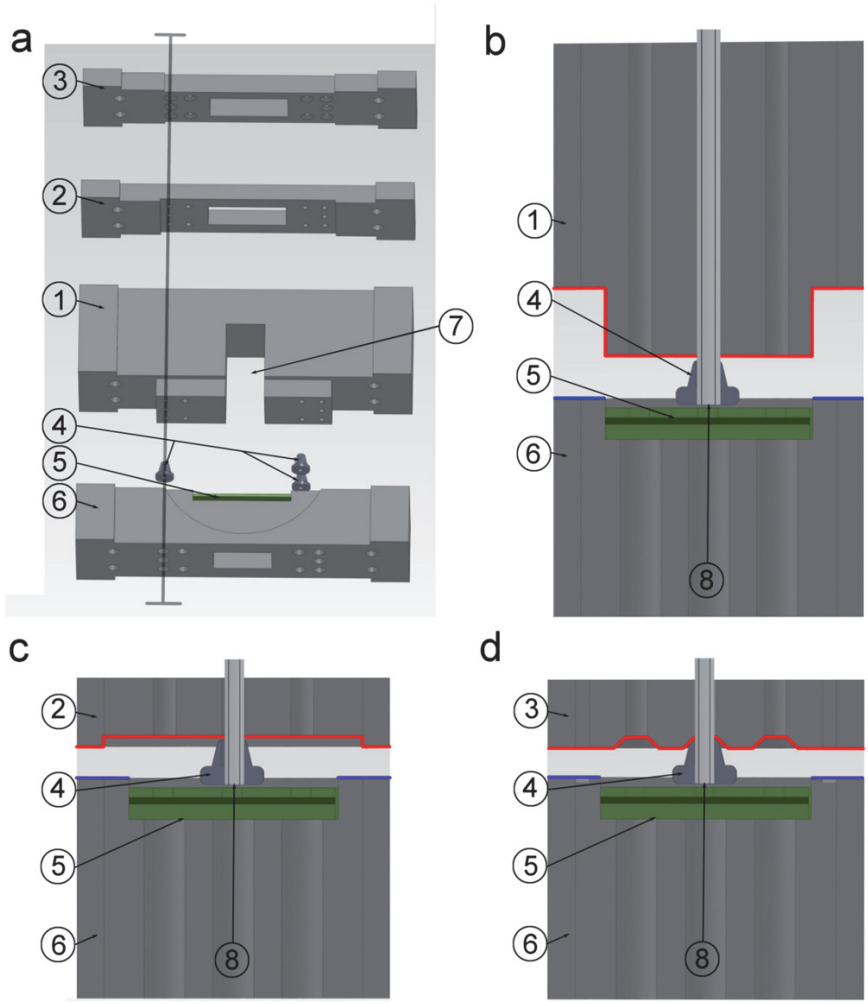


**Figure 32: Optimization of the microfluidic chip connection with 1/16" HPLC tubing (Figure 13 and Figure 14). 1:** first chip holder lid; **2:** second chip holder lid; **3**: third chip holder lid; **4**: ferrules; **5**: microfluidic chip (green); **6**: chip holder bottom; **7**: space for axle; **8**: 1/16' HPLC tubing; red line: surface of chip holder lid; blue line: surface of chip holder bottom defining the distance between chip holder lid (red line) and chip (green). **a**: Comparison of the three chip holders that were developed in the curse of this thesis as exploded view. **b** to **d**: cross section of the connection along the axis marked in subfigure a for all three chip holder lid versions tested. **b**: First chip holder version (bulky, inconvenient handling, no reproducible pressure during connection with tubing); **c**: second chip holder version (reproducible pressure due to defined distance, between lid surface (red line) and chip (green) by fence surface on chip holder bottom (blue line) but no leak-tight connection). **d**: final version of the chip holder lid which allows defined pressure on the ferrule (fence between chip holder lid (red line) and chip holder bottom (blue line)) and leak-tight connection due to use of a chamfer at the connection ports.

Because of production tolerances and wear of the ferrules, leak-tight connections of the chips were not established reproducibly. Therefore, the third and final design (Figure 32.3) was developed. The concept of a fence defining the pressure applied on the microfluidic chip was maintained but instead of adapting the headspace above the chip only chamfers on the connection ports were machined into the chip holder lid Figure 32.d red line). This design allowed for reproducible leak-tight connection, due to the fact that the final design pressures the ferrules reproducibly not only from the top but also laterally. The construction drawings of all three versions of the chip holder lid can be found in the appendix.

## 3.6 Magnetic modeling of the threefold reactor block

Magnetic modelling of the threefold reactor block was carried out in order to show that the magnetic field properties within the chip are comparable within all three reactor chips of a threefold reactor block and the single chip μMORE prototype. The flux density gradient data presented in Figure 33 shows that the numbering up only results in minor changes of the magnetic flux gradients generated for the three parallelized chips relative to a single chip system. Only a minor increase of the flux density gradient in the middle chip (green curve) can be detected. This is caused by magnetic field deviation due to parallelization. Thus, it was assumed that the beads would behave the same in all three chips of the parallelized layout and the single chip layout. Therefore, the influence of the numbering up on the magnetic field properties could be neglected for the application as an enzyme reactor.

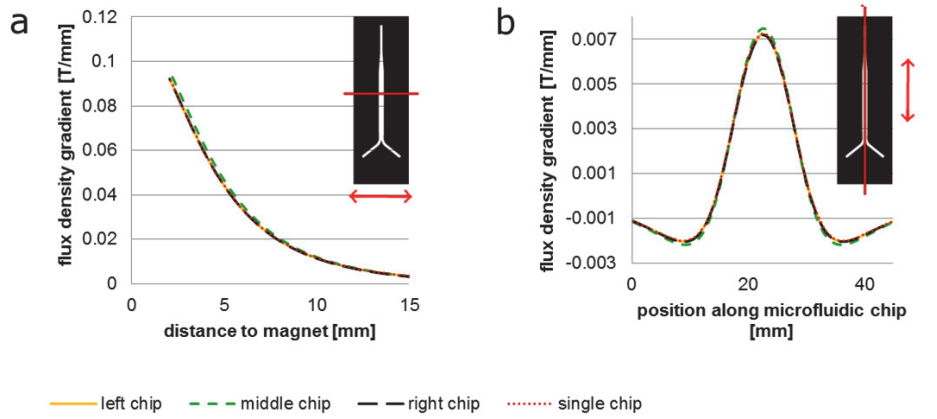


**Figure 33: Comparison of the magnetic field gradient within the three chip reactor holder compared to the single chip reactor holder for chip 2.** The pictogram in the upper right corner of each diagram indicates the axis (red line) along which the field gradient was measured; the direction (red arrow) of the gradient is visualized. **a:** magnetic field gradient along the width of the reactor in the middle of the mixing zone. **b**: magnetic field gradient along the length of the reactor along the symmetry axis of the chip.

## 3.7 Syringe fine tuning adjuster

It was observed that, when connecting more than one chip, it was impossible to place the droplet, necessary for leak-tight connection (chapter 2.8), at the end of each tube prior to connection using the syringe pump with up to a six syringes in parallel. Therefore, a fine tuning adjuster was designed in order to manually press a droplet out of each individual syringe prior to connection instead of starting the pump. The device, presented in Figure 34, consists of a 3/16 thread adapter (2), fitting into Hamilton gastight syringe plungers (1) mounting system, and a 3 mm threaded bolt (3) connected to it. At the end of the 3 mm threaded bolt are two thumb screws (4+5).

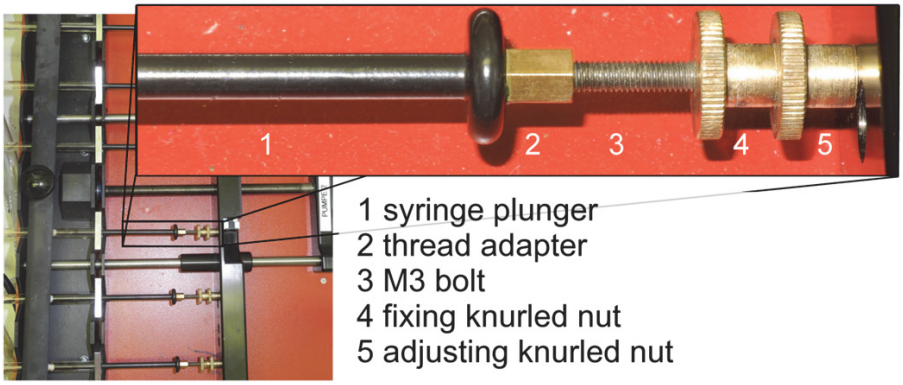


**Figure 34: Syringe fine tuning adapter to ensure air bubble free connection of the microfluidic chips. 1:** Syringe plunger, **2** thread adapte,; **3** M3 threaded bolt**, 4** thumb screw 1 (to fix position of thumb screw 2)**, 5** thumb screw 2 (to adjust plunger position).

By turning the first thumb screw (4) it was possible to adjust the length of the adapter and therefore press the plunger reproducibly while the syringe was already fixed within the syringe pump (Figure 34 b). The second screw (5) can then be used to fix the position of the first one during the reactor run.

## 3.8 Enzyme immobilization

In this work the µMORE reactor system is exemplarily used for process optimization of enzymatic carboligation using BFD (chapter 1.4) immobilized via His-Tag (chapter 1.11.1). In order to utilize the novel reactor system, the immobilization of the model enzyme (BFD) with C-terminal hexahistidine tag (His-tag) on the magnetic beads was investigated next. Therefore, the influence of the enzyme concentration on the final enzyme load on the beads was studied by increasing the BFD concentration in the supernatant and keeping the amount of magnetic bead suspension constant. Unspecific binding was characterized using bovine serum albumin (BSA) as a reference protein without His-tag. The balancing of bound protein was calculated based on the depletion of the protein concentration in the supernatant (chapter 2.14) using the Bradford assay (chapter 2.10). The results are shown in Figure 35. It can clearly be seen that up to 1 mg/mL BFD a linear correlation between enzyme in the supernatant and the amount of immobilized enzyme could be observed.

Furthermore, only very low unspecific binding of up to ca 0.8 µg/µL BSA was observed (Figure 35). As no saturation of the magnetic beads with BFD was observed, it was repeated with 10% of the initial amount of magnetic bead suspension in order to examine the maximum enzyme load of the beads (Figure 36).

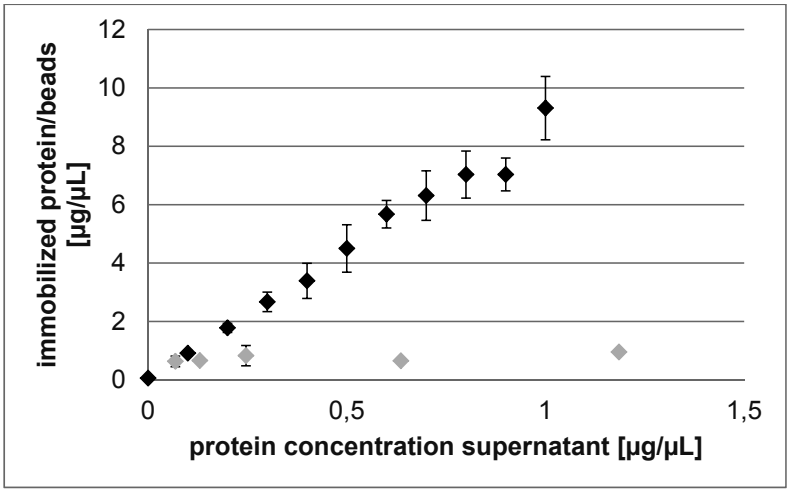


**Figure 35: Adsorption isotherms of ◆ BFD (His-tagged) and ◆ BSA on magnetic beads (10 µL bead suspension).** X- axis: protein concentration in the supernatant during bead loading; Y-axis: amount of protein (µg) immobilized per µL magnetic particles; Total volume: 200 µL, 50 mM Kpi buffer, pH 6.5; 2.5 mM $MgSO_4$ 0.1 mM ThDP.

The results indicated that saturation of the magnetic beads was reached with around 61.5 ±9.8 µg BFD per µL magnetic bead suspension. Investigation of higher enzyme concentrations was limited by the analytics and error amplification caused by necessary dilution steps to measure the protein concentration in the supernatant, as indicated by the increasing error bars.

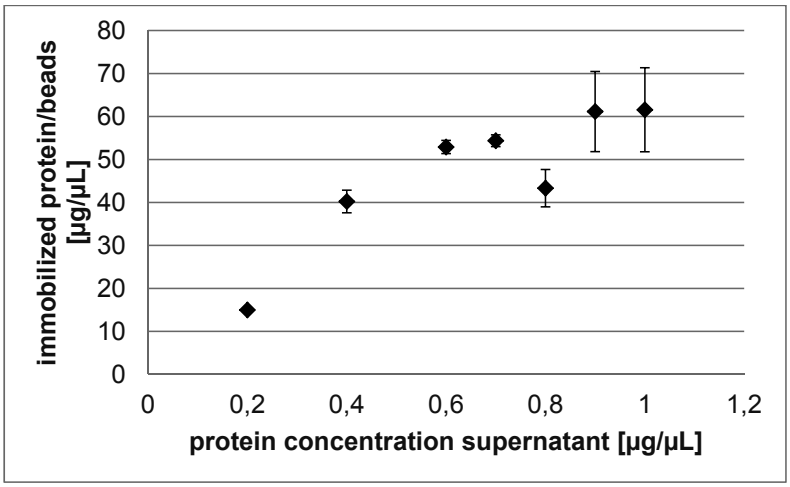


**Figure 36: Adsorption isotherms of BFD (His-tagged) on magnetic beads (1 µL bead suspension).** X- axis: protein concentration in the supernatant during bead loading; Y-axis: amount of protein (µg) immobilized per µL magnetic particles; Total volume: 200 µL, 50 mM Kpi buffer pH 6.5 2.5 mM $MgSO_4$, 0.1 mM ThDP.

Taking into account the manufacturers capacity information for PureProteome Nickel magnetic beads of 1- 5.5 µg protein per µL beads for a 30 kDa His tagged protein per µL bead suspension and the molecular weight of BFD of 248 kDa, a theoretical enzyme load of 8.3 to 45.5 µg protein per µL beads should be possible if the same number of BFD molecules can bind. However, it is likely that the capacity for larger proteins is decreased by steric effects. Additionally, it has been shown that multimeric proteins with more than one His-Tag tend to bind to more than one binding site (Nieba et al., 1997). Since BFD is a tetramer containing 4 His-Tags it is unlikely that this theoretical maximum load is achievable.

The elution of immobilized BFD with imidazole (500 mM, pH 8) was tested to quantify specifically the bound enzyme fraction. However, it was not possible to elute more than 40% of the enzyme loaded to the beads, which indicated that the enzyme was not only bound specifically to the $Ni^{2+}$-NTA-binding sites, as the applied imidazole solution should displace the protein from these binding sites.

Therefore, due to irreversible binding of the protein and the exceeding of the manufacturers binding capacity unspecific binding of the protein to the beads has to

be reconsidered. While unspecific binding of BSA as a model protein has already been excluded (Figure 35), it was concluded that the unspecific binding of BFD may result from an interaction of the His-tag with the iron included in the matrix of the magnetic beads. The presence of $Fe^{2+}$- and $Fe^{3+}$ ions on the surface of the bead matrix is also indicated by the rust brown color of the beads.

To elucidate this effect, the adsorption of BFD to iron particles was studied using the same method as for the magnetic beads. A binding of 1.36 ± 0.06 µg BFD per µL iron beads was determined with 200 µg/mL BFD in the supernatant. This underlines the conclusion that interaction with the iron ions may at least partially explain the increased binding capacity. This observation is in line with literature data, stating that $Fe^{2+}$- and $Fe^{3+}$ ions can be used as an alternative for His-tag chromatography (Lloyd R. Snyder, Joseph J. Kirkland, 2010; Lottspeich, Friedrich, Engels, 2006). Therefore, the findings strongly suggest that an interaction with the iron incorporated into the beads for magnetization is the cause for the incomplete elution of bound BFD by 500 mM imidazole. The results further indicate that pure iron particles may be a cheap alternative for enzyme immobilization.

However, a reversible enzyme binding is not necessary for the use of the His-tag immobilized enzyme in a microreactor. Therefore, the irreversible binding of the BFD does not impair the use of PureProteome Nickel magnetic beads for enzyme immobilization in a microfluidic enzyme reactor. On the contrary, the increased binding capacity of BFD in relation to the manufacturer's specifications may be favorable for immobilization and to prevent enzyme leakage. However, these findings also show that unspecific interaction of proteins with the bead matrix may impair direct immobilization form crude extract as it was originally planned.

## 3.9 Activity of immobilized BFD

In order to exemplarily investigate the influence of the immobilization on the carboligase activity of BFD comparative 250 µL batches with both, the His-tagged variant of the free enzyme and the same enzyme bound to magnetic beads were conducted with equal concentrations of 0.01 $\mu g_{BFD}/mL_{reaction\ volume}$ (Table 6).

**Table 6: Carboligase activity towards the formation of 2-HPP catalyzed by free and immobilized His-tagged BFD, respectively.** Reaction conditions: 20 mM benzaldehyde, 200 mM acetaldehyde in 50 mM TEA buffer, 2.5 mM $MgSO_4$, 0.1 mM ThDP, pH 7.5, 20°C.

| Enzyme state | Enzyme concentration | Activity (U/mg BFD) |
|---|---|---|
| **Immobilized enzyme** | 0.01 mg/mL | 2.67 ±0.01 |
| **Free enzyme** | 0.01 mg/mL | 4.92 ±0.05 |

The results clearly indicate that the initial carboligase activity of the immobilized enzyme (2.67 ±0.01 U/mg) is almost exactly half of the initial activity of the free enzyme (4.9 ±0.05 U/mg) under the tested conditions. It has been published that multimeric proteins often bind via more than one Ni-NTA group via His-tag (chapter 3.8). An attachment of more than one monomers of a tetrameric BFD molecule may cause the polymeric matrix of the support material to block one or more of the four active sites, which would explain the lower activity.

## 3.10 Carboligation studies in the µMORE

BFD (chapter 1.4), was used to study the enzymatic carboligation of benzaldehyde and acetaldehyde in the µMORE system. The goal was to identify relevant process parameters such as the temperature optimum, pH-optimum, and optimal substrate concentrations using the µMORE system and to compare them with earlier determined data using batch reactions and an enzyme membrane reactor (EMR) (Iding et al. 2000). All reactions were carried out continuously with a flow rate of 24 µL/h except for the residence time variation (chapter 3.10.5) in the µMORE.

The reaction parameters were adjusted such that factors influencing the activity and stability of the enzyme became pronounced during the rapid measurements (Figure 10), before the steady state was reached. This was achieved by high flow rates (24 µL/h), low residence times (2.5 min), and a low enzyme load (1 µg BFD on 0.5 µL magnetic bead suspension) in a volume of ca. 1 µL (mixing zone of the reactor Figure 28). The total volume of the microfluidic chip was 7.36 µL. Therefore, all continuous conversion curves show rapid enzyme inactivation. In this case this was a desired effect in order to shorten the measuring times and to investigate, whether

relevant data for the respective system could be obtained without reaching a stable steady state (1.6.1). It has to be taken into account that leaching of the enzyme from the beads may cause a loss of enzyme activity for all µMORE experiments. However, due to lack of appropriate analytics for enzyme quantification in the ng range this effect was not investigated.

Identification of optimal reaction parameters started with pH optimization at 30°C using substrate concentrations of 25 mM benzaldehyde and 250 mM acetaldehyde. Afterwards the temperature and then the substrate concentrations were optimized. All reactions were carried out twice. The complete reactor data is depicted in the appendix. For all µMORE carboligation runs the two substrate solutions were added separately into the two inlets of the Y shaped microfluidic chip 2 (Figure 21). Although in the present case both aldehydes could have been mixed prior to the experiment, this was done to demonstrate the potential of the reaction system also for reactions with e.g. chemical side reaction for which the substrates have to be stored separately.

**Table 7: Overview of all µMORE experiments carried out during the course of the exemplary parameter optimization.** Enzyme load: 1 µg on 0.5 µL beads; buffer pH 6.5 to 7: 50 mM Kpi; 0.1 mM ThDP, 2.5 mM $MgSO_4$; buffer pH 7.5 to 8.0: 50 mM TEA; 0.1 mM ThDP 2.5 mM $MgSO_4$, (substrate concentrations refer to concentrations in the reaction chamber; inital substrate concentration before mixing in the microfluidic chip were twice this). All experiments were carried out twice.

| pH* | T [°C] | benzaldehyde [mM] | acetaldehyde [mM] | Flow rate (µL/h) | Results in chapter |
|---|---|---|---|---|---|
| **6.5** | 30 | 25 | 250 | 24 | 3.10.1, 3.10.2 |
| **7.0** | 30 | 25 | 250 | 24 | 3.10.1 |
| **7.5** | 30 | 25 | 250 | 24 | 3.10.1 |
| **8.0** | 30 | 25 | 250 | 24 | 3.10.1 |
| **6.5** | 10 | 25 | 250 | 24 | 3.10.2 |
| **6.5** | 20 | 25 | 250 | 24 | 3.10.2 |
| **6.5** | 40 | 25 | 250 | 24 | 3.10.2 |
| **6.5** | 50 | 25 | 250 | 24 | 3.10.2 |
| **7.5** | 20 | 25 | 50 | 24 | 3.10.3 |
| **7.5** | 20 | 25 | 100 | 24 | 3.10.3 |
| **7.5** | 20 | 25 | 200 | 24 | 3.10.3, 3.10.4 |
| **7.5** | 20 | 25 | 300 | 24 | 3.10.3 |
| **7.5** | 20 | 10 | 200 | 24 | 3.10.4 |
| **7.5** | 20 | 15 | 200 | 24 | 3.10.4 |
| **7.5** | 20 | 20 | 200 | 24 | 3.10.4, 3.10.5 |
| **7.5** | 20 | 10 | 200 | 8 | 3.10.5 |
| **7.5** | 20 | 10 | 200 | 4 | 3.10.5 |

*at the given reaction temperature

### 3.10.1 pH-optimum of continuous BFD-catalyzed carboligation

Determination of the pH-optimum was carried out at pH 6.5, 7.0, 7.5 and 8.0 (for detailed buffer composition please refer to Table 7) using 25 mM benzaldehyde and 250 mM acetaldehyde at 30°C. The results for the BFD-catalyzed formation of (*S*)-HPP are presented in Figures 37 and 38. Figure 39 shows the (*S*)-HPP formation over time. It can clearly be seen that maximum conversion was achieved at pH 7.5 (grey color).

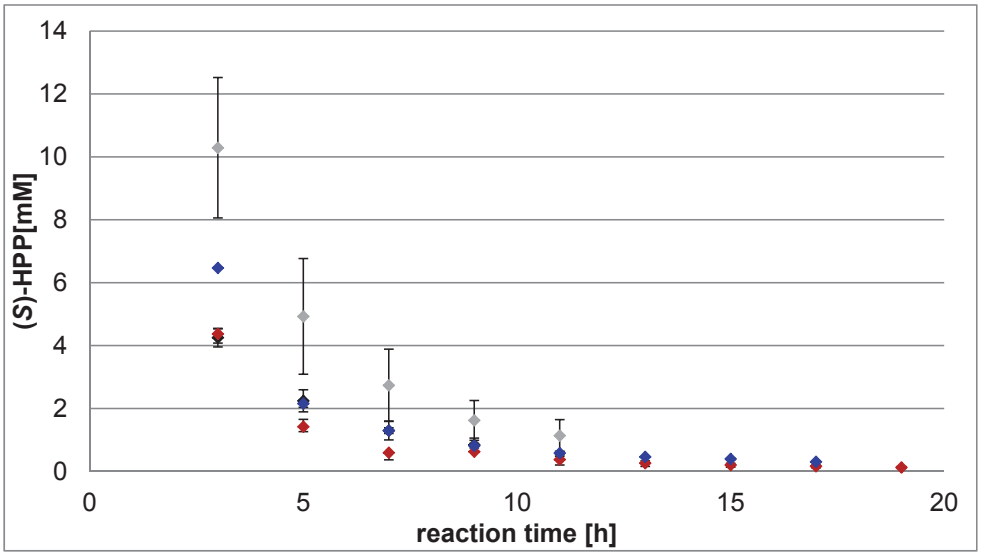


**Figure 37: (*S*)-HPP formation in the µMORE reactor at different pH-values: ◆ pH 6.5; ◆pH 7.0; ◆ pH 7.5; ◆ pH 8.0.** Enzyme load: 1 µg on 0.5 µL beads; 250 mM acetaldehyde; 25 mM benzaldehyde; 30°C. For detailed buffer composition please refer to Table 7.

The results for all tested pH-values are summarized in Figure 38 and were combined with the respective half-life of the enzyme, as calculated from the decay of activity (chapter 1.6.1, equation 1). Figure 38 clearly shows that maximum productivity for the formation of (*S*)-HPP is reached at pH 7.5. This holds for a reaction time of 3 h (10.3±2.2 mM (*S*)-HPP) and also for a reaction time of 9 h (1.6±0.6 mM (*S*)-HPP), which were significantly higher compared to the respective productivities at the other pH values tested. Besides, the half-life of BFD does not differ significantly between the different pH values. The half-life obtained for the different pH-values differs between 3.2 – 4.0 h within the error margins.

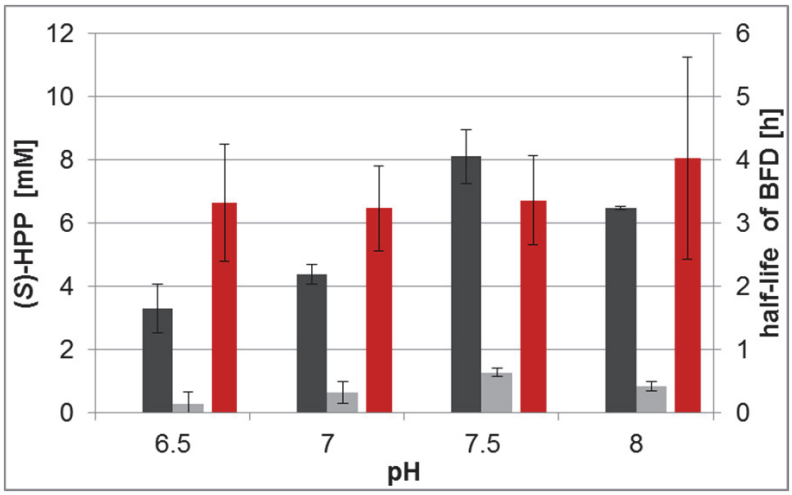


**Figure 38: (*S*)-HPP formation after 3 h ■ and 9 h ■ as well as half-life of BFD ■ in the µMORE reactor at different pH-values (6.5; 7.0; 7.5; 8.0).** For detailed reaction details please refer to **Figure 37** or Table 7.

Considering all four reactor runs a pH-optimum of 7.5 was determined for the (*S*)-HPP production under the tested conditions (Table 7). This is in good agreement for respective data obtained by Iding et. al. in a 10 mL EMR (Iding et al., 2000).

### 3.10.2 Temperature optimum of continuous BFD-catalyzed carboligation

Identification of the temperature optimum of the BFD-catalyzed formation of (*S*)-HPP was studied at pH 6.5 (for detailed buffer composition please refer to Table 7) between 10°C and 50°C with 10°C increments. The data presented in Figure 39 indicates a very low conversion at 10°C (black curve), whereas conversion increased with temperature up to 30°C (grey curve). It can also be seen that enzyme activity at 40°C (blue curve) and 50°C (green curve) is lower than at 20°C (red curve) or 30°C. This is most likely due to rapid enzyme inactivation. The reaction at 20°C provides a good compromise between conversion and enzyme stability.

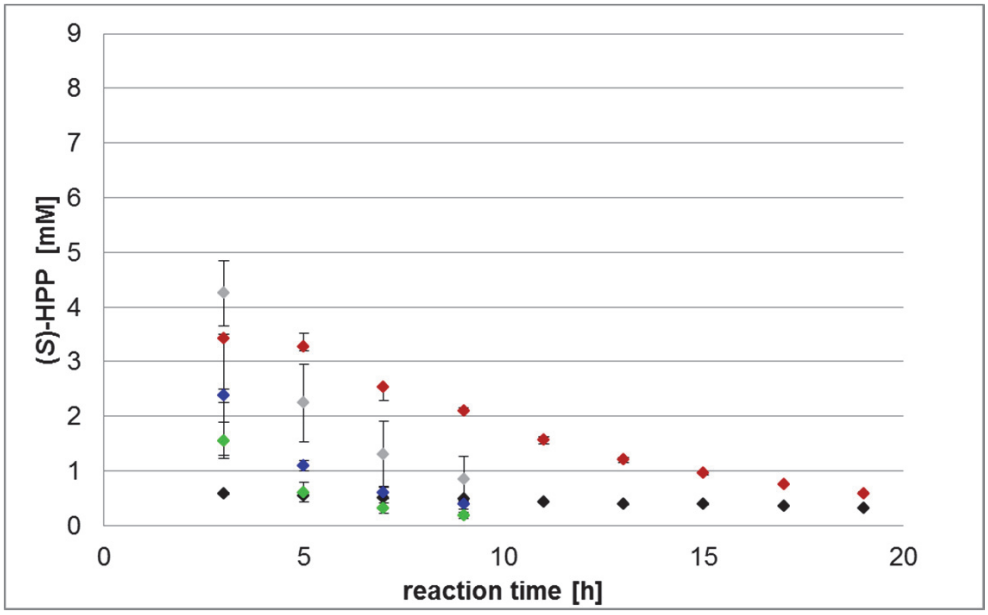


**Figure 39: (*S*)-HPP formation in the µMORE reactor at different temperatures:** ◆ 10°C; ◆20°C; ◆ 30°C; ◆ 40°C; ◆ 50°C. Enzyme load: 1 µg on 0.5 µL beads; pH 6.5; 250 mM acetaldehyde; 25 mM benzaldehyde. For detailed reaction parameters please refer to Table 7. Data are mean values of two independent reactor runs.

The summary depicted in Figure 40 confirms that the half-life of the enzyme is highest at 10°C (23.1±0.04 h) and decreases with increase of the temperature. Despite the long half-life, 10°C is not favorable for a production process due to the low productivity of the system (0.6±0.0 mM (*S*)-HPP after 3 h reaction time). While there is only a small difference in conversion after 3 h between 20°C (3.4±0.1 mM (*S*)-HPP) and 30°C (4.2±0.6 mM (*S*)-HPP), the higher stability at 20°C results in a 2.6-fold higher (*S*)-HPP concentration (2.1±0.1 mM) after 9 h compared to a reaction temperature of 30°C (Figures 34, 35). Therefore, 20°C is the best tested reaction temperature for the BFD-catalyzed formation of (*S*)-HPP in the µMORE.

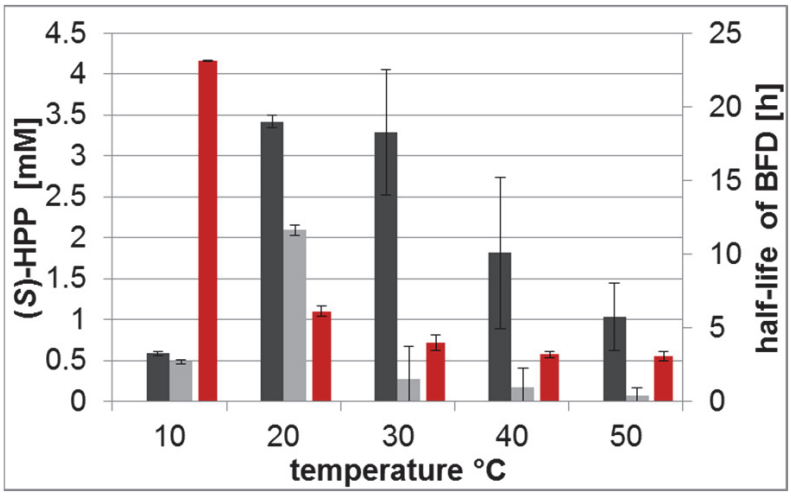


**Figure 40: (*S*)-HPP formation after 3 h ■ and 9 h ■ as well as half-life of BFD ■ in the µMORE reactor at different temperatures** (10°C, 20°C 30°C 40°C 50°C). For detailed reaction parameters please refer to Figure 39 and Table 7.

As temperature might also affect the stereoselectivity of the carboligation reaction and/or the stability of the (*S*)-HPP, the enantiomeric excess (*ee*) was studied as a function of temperature. The 3 h sample was chosen for *ee* comparison, because all reaction curves showed conversions high enough for quantification of both enantiomers. The results presented in Table 8 clearly indicate a strong decrease of the *ee* for (*S*)-HPP with increasing temperature from 89±0.5% at 10°C to 77±3.9% at 50°C. Temperature-dependent racemization is unlikely to cause the reported trends in *ee* considering the time spend in the temperature controlled reaction chip of ca. 18.4 min and the high stability of (*S*)-HPP up to pH 10 and 30°C (Kihumbu, 2007).

**Table 8: Enantiomeric excess of the (S)-HPP production after 3 h in the µMORE at different temperatures.** For detailed reaction parameters please refer to Figure 39 and Table 7.

| Temperature [°C] | ee (3 h) [%] |
|---|---|
| **10** | 89 ± 0.49 |
| **20** | 86 ± 0.53 |
| **30** | 86 ± 0.92 |
| **40** | 79 ± 0.07 |
| **50** | 77 ± 3.92 |

Similar trends of increased activity versus decreased half-life and *ee* of BFD with increasing reaction temperature were also reported by Iding et. al. (Iding et al., 2000). While the trends of Iding et al. were reproduced, the exact values of conversion and *ee* differ. It has to be taken into account that immobilized BFD was used in the continuous µMORE whereas free enzyme in batch reaction was used by Iding et. al. Thus, it cannot be expected to reproduce the exact literature values obtained by Iding et al.

### 3.10.3 Optimization of the acetaldehyde concentration

After pH and temperature the influence of the substrate concentrations on the BFD-catalyzed carboligation was investigated. First the acetaldehyde concentration was varied between 50 mM and 300 mM in TEA-buffer, pH 7.5 (Table 7), while the benzaldehyde concentration was kept constant at 25 mM. A clear maximum of (*S*)-HPP production at 250 mM acetaldehyde (blue curve) can be seen in Figure 41. By contrast, lower and higher concentrations of acetaldehyde resulted in a decrease of product formation.

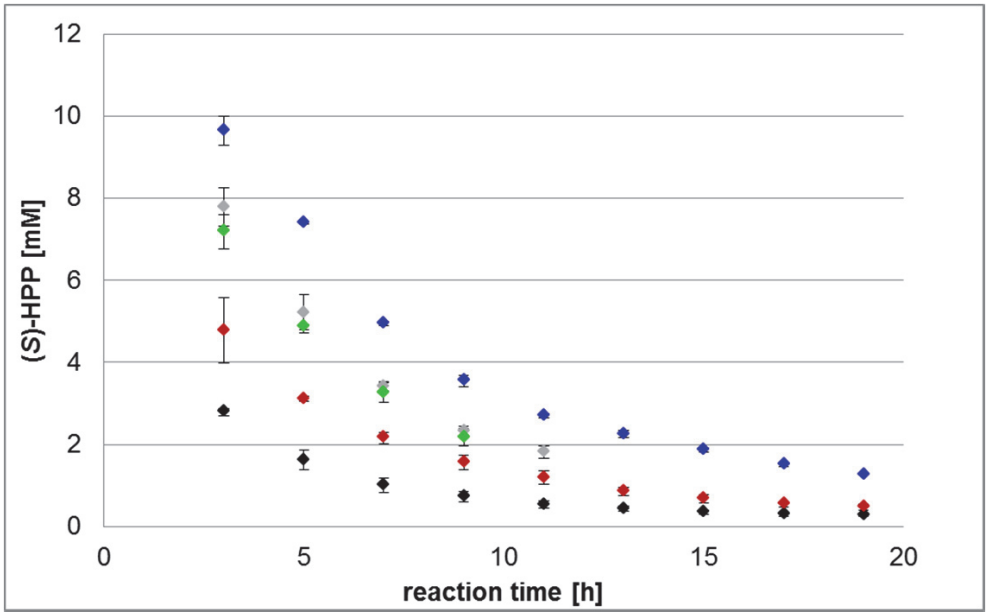


**Figure 41: (S)-HPP formation in the µMORE reactor at different acetaldehyde concentrations:** ◆ 50 mM; ◆100 mM; ◆ 200 mM; ◆ 250 mM; ◆ 300 mM. Enzyme load: 1 µg on 0.5 µL beads; pH 7.5; 25 mM benzaldehyde; 20°C. For detailed reaction parameters please refer to Table 7. Data are mean values of two independent reactor runs.

The trends discussed on the basis of Figure 41 are summarized in Figure 42. We observed no influence of the acetaldehyde concentration on the half-life of BFD. The half-lifes are all in a very small range between 3.7±0.3 h (50 mM acetaldehyde), 4.2±0.4 h (250 mM acetaldehyde), and 3.9 ±0.7 (300 mM acetaldehyde). This is in agreement with Iding et. al., who reported only a very small change of the half-life of BFD in the presence of acetaldehyde concentrations between 100 mM and 200 mM

(Iding et al., 2000). Furthermore, the clear productivity optimum of (*S*)-HPP with 250 mM Acetaldehyde, which was already indicated in Figure 41, was confirmed. The (*S*)-HPP production is highest with 9.6 ±0.7 mM after 3 and 3.5 ±0.3 mM after 9 h for this acetaldehyde concentration when compared to the other reactor runs summarized in Figure 42. For acetaldehyde concentrations below and above this optimum the product formation decreases.

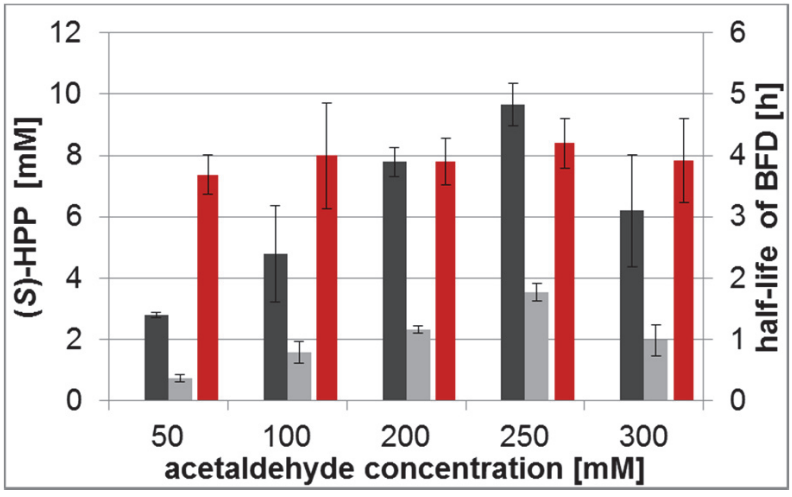


**Figure 42: (*S*)-HPP formation after 3 h ■ and 9 h ■ as well as half-life of BFD ■ in the µMORE at different acetaldehyde concentrations** (50 mM; 100mM; 200 mM; 250 mM 300 mM). For detailed reaction parameters please refer to Figure 41 and Table 7.

Further, the finding that a tenfold excess of acetaldehyde relative to benzaldehyde is preferred for maximal productivity and selectivity concerning (*S*)-HPP is in line with results obtained earlier in a 10 mL EMR (Iding 2000).

### 3.10.4 Optimization of the benzaldehyde concentration

Finally the benzaldehyde concentration was optimized. All reactions were carried out in TEA-buffer, pH 7.5 (Table 7) with 200 mM acetaldehyde at 20°C while the benzaldehyde concentration was variated between 10 mM and 25 mM in 5 mM increments. A lower acetaldehyde concentration than the optimum determined in the preious chapter (250 mM) was chosen in order to also investigate the effect of an acetaldehyde excess lower than tenfold during the benzaldehyde investigation. The

data presented in Figure 43 indicates an increase of (*S*)-HPP formation with increasing benzaldehyde concentration. This suggests that high benzaldehyde concentrations are favorable for (*S*)-HPP production.

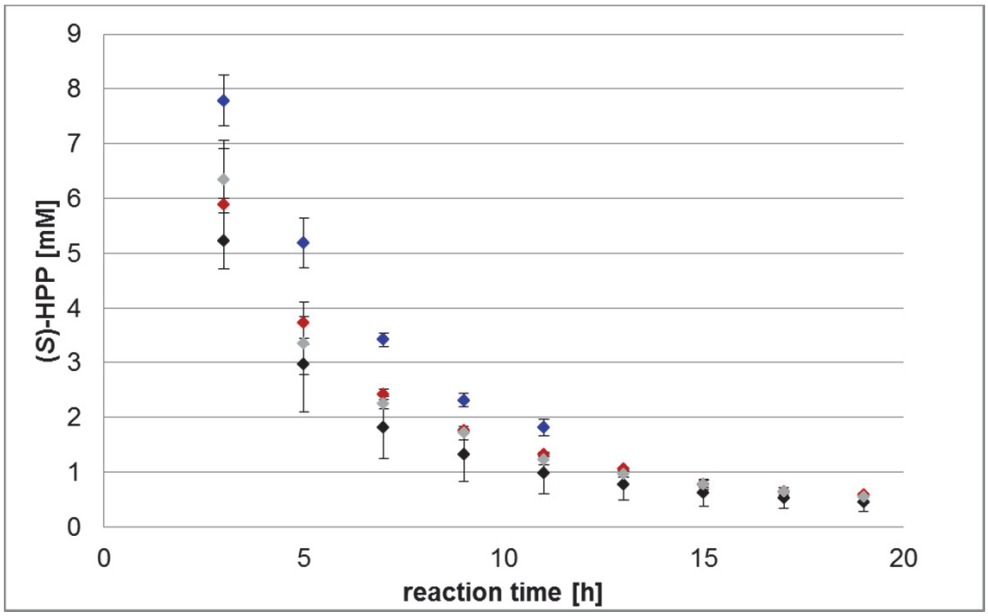


**Figure 43: (*S*)-HPP formation in the µMORE reactor at different benzaldehyde concentrations:** ◆ 10 mM; ◆15 mM; ◆ 20 mM; ◆ 25 mM. Enzyme load: 1 µg on 0.5 µL beads, 50 mM TEA buffer, pH 7.5, 200 mM acetaldehyde, 20°C. For detailed reaction parameters please refer to Table 7. Data are mean values of two independent reactor runs.

The differences between the half-life ($t_{1/2}$)at different benzaldehyde concentrations between 10 mM ($t_{1/2}$)=3.7±1.0) and 25 mM ($t_{1/2}$)=3.9±0.4) presented in Figure 44 are only minimal and do not show any clear trends. Furthermore, the summary diagram indicates that between 10 mM and 20 mM only very small differences (within the error margin) in productivity can be observed. A maximum (*S*)-HPP production was reached at 25 mM benzaldehyde (7.8 ±0.5 mM after 3 h and 2.3 ±0.1 mM after 9 h).

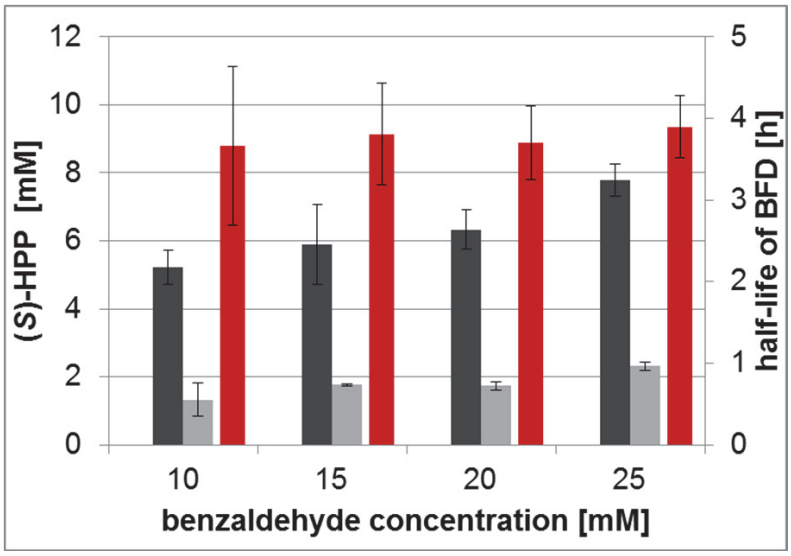


**Figure 44: (*S*)-HPP formation after 3 h ■ and 9 h ■ as well as half-life of BFD ■ in the µMORE reactor at different benzaldehyde concentrations** (10 mM; 15 mM; 20 mM; 25 mM). For detailed reaction parameters please refer to Figure 43 and Table 7.

However, when the *ee* for (*S*)-HPP of 91±0.7% obtained with 10 mM benzaldehyde versus 87±0.09% with 25 mM benzaldehyde (Table 9) is considered, the complete data presents a different productivity optimum at 10 mM benzaldehyde.

**Table 9: Enantiomeric excees obtained for (*S*)-HPP after 3 h for benzaldehyde concentrations during µMORE reaction. For detailed reaction parameters please refer to Figure 43 and Table 7.**

| Benzaldehyde [mM] | (*ee*) (3 h) [%] |
|---|---|
| **10** | 91±0.70 |
| **15** | 90±0.11 |
| **20** | 89±0.20 |
| **25** | 87±0.09 |

Furthermore, if the benzaldehyde conversion is considered instead of the product formation, which is 52% after 3 h with 10 mM benzaldehyde versus only 32% (3 h) with 25 mM benzaldehyde, the data presented shows that low benzaldehyde concentrations combine high conversion rates with high *ee*-values for the (*S*)-HPP

production. Thus, low benzaldehyde concentrations are favorable despite the fact that higher (*S*)-HPP concentrations were obtained at higher benzaldehyde concentrations. The finding that low benzaldehyde concentrations are preferred are again in line with the previously published data (Iding et al., 2000).

### 3.10.5 Optimization of the residence time

The data presented in the previous chapters (3.10.1 to 3.10.5) concering optimization of pH, temperature and substrate concentrations, successfully demonstrated the applicability of the novel µMORE system for process parameter optimization in biocatalysis. The next step for a process optimization was the development of a production process based on the determined optimal parameters. Therefore, the productivity optimum of the process was used for residence time optimization. The reaction parameters used for this experiment were 10 mM benzaldehyde, 200 mM acetaldehyde, 20°C, TEA buffer, pH 7.5, (Table 7). The flow rate of the reactor was then varied between 24 µL/h (used for all previous experiments) and 4 µL/h (Figure 45). For calculation of the residence time, a reaction volume of 1 µL was used. This corresponds to the part of the channel in which the beads actually move (chapter 3.3.4). Thus, the selected flow rates correspond to the following residence times: 2.5 min (24 µL/h), 7.5 min (8 µL/h), and 15 min (4 µL/h). One drawback of the large sample volume relative to the reactor volume is a very low time resolution for the reactor runs with (τ=7.5 min and 15 min). Thus, the sampling volume was reduced to 24 µL for the 4 µL /h and 8 µL /h experiments, respectively, to increase the time resolution of the data points. Figure 45 indicates that the production of (*S*)-HPP was successfully increased with increasing residence time. The longer residence times resulted in 80% (τ=7.5 min) and 100% conversion (τ=15 min), before enzyme inactivation led to rapid decrease of conversion.

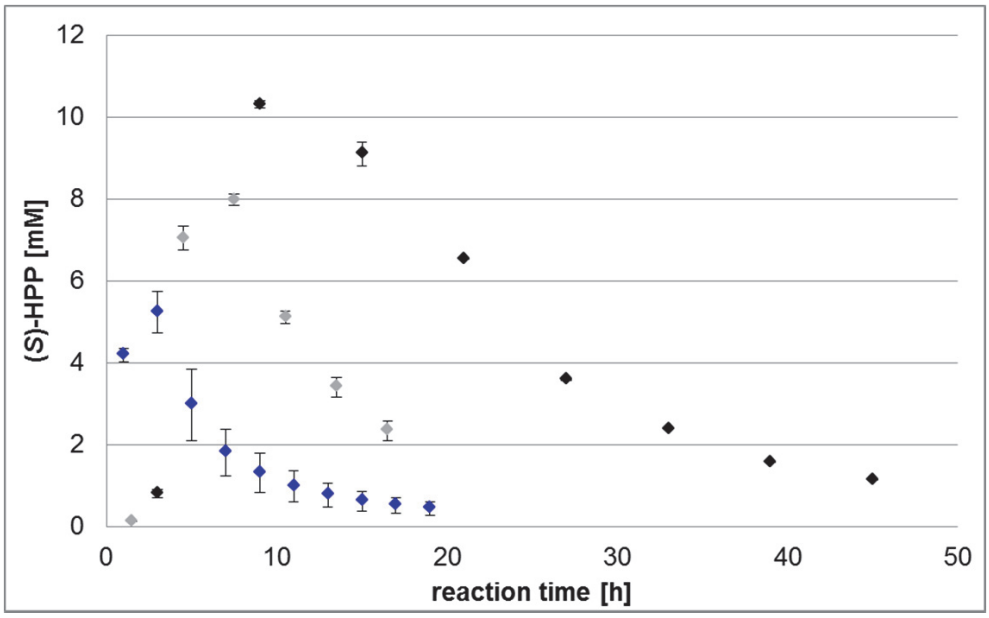


**Figure 45: (*S*)-HPP formation in the µMORE reactor at different residence times/flow rates:** ◆2.5 min /24 µL/h; ◆7.5 min /8 µL/h; ◆ 15 min /4 µL/h. Enzyme load: 1 µg on 0.5 µL beads; 50 mM TEA buffer, pH 7.5; 10 mM benzaldehyde; 200 mM acetaldehyde; 20°C. For detailed reaction parameters please refer to Table 7. Data are mean values of two independent reactor runs.

As demonstrated in Table 10, alteration of the residence time did not influence the *ee* of (*S*)-HPP significantly.

**Table 10: Effect of the residence time on the enantiomeric excess of (*S*)-HPP after 48 τ (equivalent to 3h reaction time in the previous sections).**
For detailed reaction parameters please refer to Table 7.

| Residence time [min] | Flow rate [µL/h] | *ee* (48 τ) [%] |
|---|---|---|
| **2.5** | 24 | 90.9± 0.3 |
| **7.5** | 8 | 91.7± 0.4 |
| **15** | 4 | 89.2± 0.7 |

In order to point out the effects of residence time optimization on the (*S*)-HPP production, the space-time-yield (STY) [mM/h] over the first 96 τ and the half-life of the enzyme were compared for all three reactor runs in Figure 46. It can clearly be seen that the STY decreased with increasing residence time even though higher

conversion could be reached with longer residence times. At the same time the half-life of BFD increased with increasing residence time. However, enzyme inactivation should be flow rate independent within an ideally mixed reactor at a given residual activity. As the conversion curves (Figure 45) do not show a uniform inactivation pattern at different residence times, this can be taken as a first indication for non-ideal mixing within the µMORE.

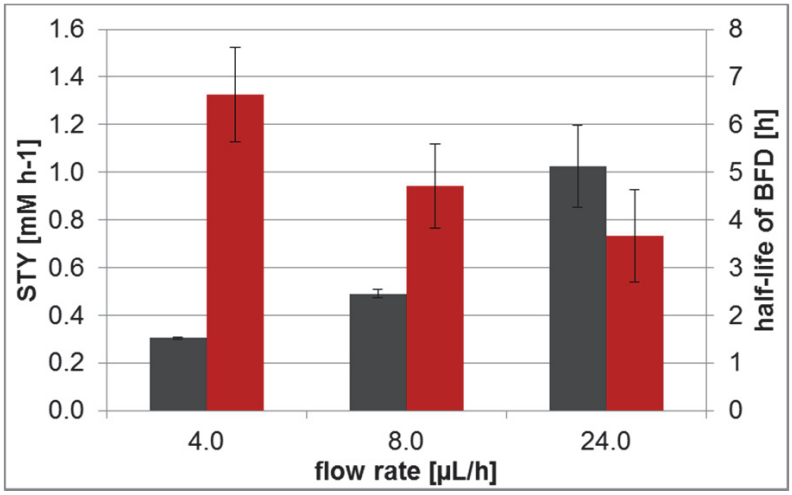


**Figure 46: ■ Half-life of the BFD and ■ space time yield of the µMORE for different flow rates during the first 96 τ.** For detailed reaction parameters please refer to Figure 45 and Table 7.

For a non-ideally mixed continuous reactor the inactivation constant is influenced by residence time-dependent and residence time-independent factors. The constant partition of the inactivation process is caused by all parameters which are constant within the reactor, while the residence time/flow rate-dependent partition is caused by parameters which are not constant during the course of the reaction, but appear to become more constant at lower flow rates/longer residence times. A concentration gradient along the length of the reactor would explain the increasing half-life of BFD at increasing residence time, because at a given oscillation frequency the beads oscillate more often per volumetric flow than at lower flow rates/longer residence times. Thus, a lower flow rate/longer residence time results in better mixing of the reactor.

First the flow rate-independent partition is discussed. The influence of temperature and pH on the BFD has been thoroughly investigated (chapter 3.10, Iding 2000). As

those factors are constant within the reactor runs, these parameters are constant for all reactor runs at different residence times. Additionally, flow rate-independent inactivation may be caused by shear stress or leaching of the enzyme from the beads.

The results of the optimization of the acetaldehyde concentration (3.10) show no significant influence of the acetaldehyde concentration between 100 mM and 200 mM acetaldehyde. Therefore, it can be assumed that the maximal change in acetaldehyde concentration of 5 % (10 mM) at 100% conversion cannot be the cause of increased inactivation at higher flow rates/lower residence times. While numerous different factors affect the constant partition of the inactivation, the only enzyme inactivating parameter changing over the course of the reaction is the benzaldehyde concentration. An influence of the increasing (S)-HPP accumulation in the reactor can be ruled out as no substrate surplus inhibition was detected for BFD (Iding et al., 2000). In a reactor with plug flow characteristics or a non-ideally mixed CSTR the substrate concentration changes depending on the position within the reactor (chapter 1.6.1). Therefore, a concentration gradient of the benzaldehyde is the most probable cause for the flow rate/residence time dependence of the enzyme inactivation. Further experiments with longer residence times are necessary to verify these findings. Thus, it may also be possible to achieve an almost ideal CSTR mode with the µMORE reactor.

### 3.11 Scale up of µMORE process to a 10 mL bench scale reactor

After having successfully optimized an exemplary process at microscale the obtained set of parameters was used to set up a continuous bench-scale process using a 10 mL EMR (Wandrey, 1979), which corresponds to a scale up by a factor of $10^4$. The enzyme load and the flow rate were increased by the same factor (10 mg/10 mL and 40 mL/h, respectively), whereas all other reaction parameters were maintained as optimized at microscale However the reduced activity of the BFD (chapter 3.9) results in 50% of the activity in the µMORE relative to the EMR. The scale up experiment in the EMR reactor was carried out two times. The respective conversion curve relative to the µMORE system is presented in Figure 47. While both reactors

exhibit almost full conversion in the beginning of the reaction, a 2.7 times faster enzyme inactivation is present in the µMORE reactor (black curve) relative to the EMR (red curve) (Figure 47). Additionally it can be seen that the initial lag phase of the µMORE is ca. six times longer compared to the EMR. This is caused by the larger dead volumes of reactor chip, outlet tubing and sampling needle relative to the reactor volume and the flow rate.

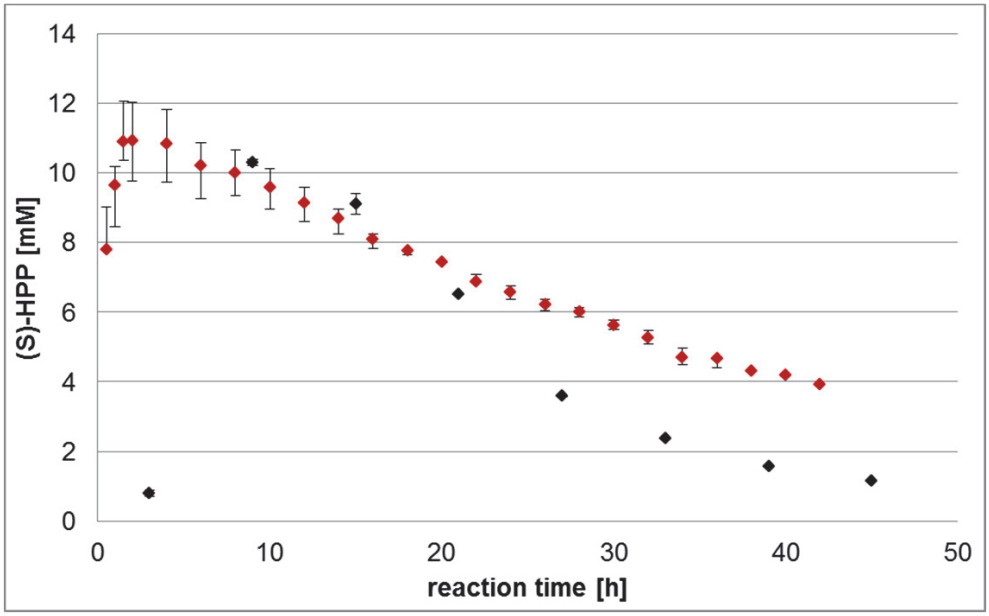


**Figure 47: (*S*)-HPP formation in the ◆ EMR and ◆ µMORE.** Residence time 15 min; Flowrate: 4µL/h (µMORE), 40 mL/h (EMR). Enzyme load: 1 µg on 0.5 µL beads (µMORE), 10 mg (EMR); 50 mM TEA buffer, pH 7.5; 10 mM benzaldehyde; 200 mM acetaldehyde; 20°C. For detailed reaction parameters please refer to Table 7. Data are mean values of two independent reactor runs.

This trend is underlined by the half-life of BFD of only 6.6 h ±1.0 (µMORE) versus 15.7 h ±2.4 (EMR). This relation further backs the assumption of the µMORE reactor's non ideal behavior, especially at higher flow rates stated in chapter 3.10.5. However it has to be taken into account that the increased enzyme inactivation may also be caused by washout or inactivation due to the immobilization process.

The lowerspace time yield of the µMORE system of 0.30 ±0.00 mM/h versus 0.34 ±0.02 mM/h obtained in the EMR over the first 96 τ after reaching maximum conversion is on the one hand caused by the lower activity of the immobilized

enzyme within the µMORE reactor relative to the free enzyme in the EMR. This results in a shorter steady state of the reactor. On the other hand the productivity in the EMR is positively affected by higher stability of the enzyme.

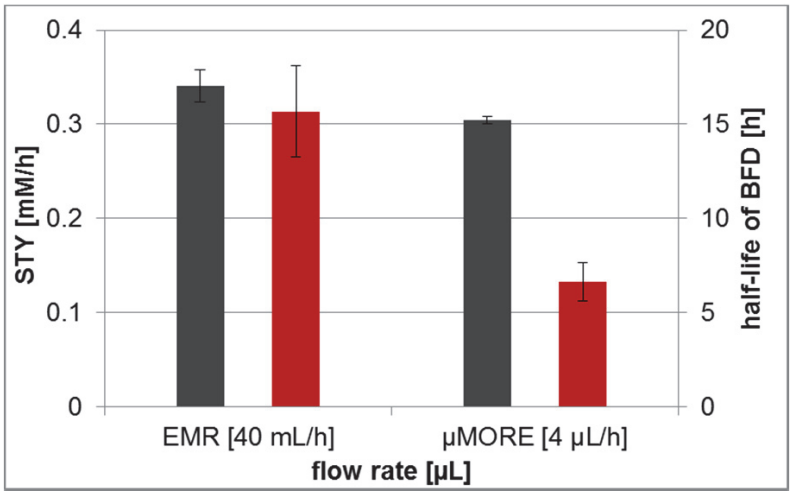


**Figure 48: Comparison of ■ half-life of the BFD and ■ space time yield for the µMORE and EMR.** For detailed reaction parameters please refer to Figure 47 and Table 7.

Despite the lower activity and the more rapid inactivation of the BFD in the µMORE the scale up experiment shows the potential as a process optimization tool as data in the same order of magnitude was generated. In comparison, the buffer volume used in single run of the µMORE for 200 residence times during process optimization used is only about 0.22% of the volume relative to equivalent studies in a 10 mL EMR. The volumetric downscale factor of $10^{-4}$ is not completely achieved due to the fact that small volume handling, especially for the volatile aldehydes limits minimum liquid handling volumes. Furthermore, taking the enzyme loss by immobilization into account, a reduction of the amount of enzyme to 0.8% was achieved when comparing the enzyme consumption of the µMORE and the 10 mL EMR system. While buffer and substrate costs are negligible for the current process, in case of highly valuable substrates the downscale to the µMORE may make development of an enzymatic process more attractive by reduction of the substrate and enzyme cost during process development. By using higher enzyme loads and even faster flow rates up to twelve experiments within one day are possible with only one six-fold µMORE system. Currently, instrumental analytics is the bottleneck for data

generation rather than the µMORE reactor. Thus, labour and laboratory cost can also be reduced.

The volumetric downscale in combination with a completely closed reaction system from buffer reservoir to sampling tube, as implemented in the µMORE system, is also especially advantageous for the work with toxic compounds.

# 4 Summary

The microfluidic magnetic oscillation reactor for enzymes (μMORE) based on magnetic bead mixing was developed, first characterized by dye distribution and optimized for its mixing characterization. Subsequently, the μMORE was parallelized to a six-fold microreactor system. Further, handling and setup of the reactor system were optimized in order to ensure reproducible reactor filling with magnetic beads and connection to the tubing. Proof of principle for its application as process optimization tool in biocatalysis was demonstrated using benzoylformate decarboxylase (BFD) from *Pseudomonas putida* as a model enzyme to catalyze the carboligation of benzaldehyde and acetaldehyde yielding (*S*)-2-hydroxypropiophenone (HPP). Reproducible and easy enzyme immobilization of BFD, carrying a C-terminal hexahistidine tag, on magnetic beads was achieved via Nickel-chelate binding to the magnetic beads. However, a complete characterization of the enzyme immobilization, especially with regards to leaching of bound enzyme under reaction conditions, could not be achieved due to additional unspecific binding of the enzyme to the beads. Despite this shortcoming all trends of the enzyme performance investigated in the μMORE with regards to conversion, stability and stereoselectivity with respect to variation of temperature, pH, and substrate concentrations could by reproduced relative to literature data (Iding et al., 2000). An upscale of the reaction, optimized at microscale to labscale was carried out using a 10 mL EMR with free enzyme.

Comparison of both reactor systems demonstrated that with the μMORE system we were able to determine all optimal process parameters using less than 1% of buffer, catalyst, and substrate, respectively, relative to a 10 mL EMR. It was not expected that both systems would yield fully comparable data, since the differences concerning reactor material, flow properties, mixing, and specifically the differences in enzyme preparation (free enzyme immobilized behind a membrane and immobilized on magnetic beads, respectively) must result in differences in enzyme stability and performance. Thus, the 2.7-fold higher stability and the 10% higher productivity of BFD during steady state observed in the EMR was not surprising. It is assumed that both effects are correlated with the immobilization of BFD on the magnetic beads in case of the μMORE. As immobilization resulted in an about 50% loss of activity, equal enzyme concentrations resulted in a higher active catalyst load

in case of the EMR. Further, enzyme leaching from the magnetic beads as a reason for the higher enzyme inactivation in the µMORE could not be ruled out. Additionally the problem of non-ideal mixing behavior of the reactor has to be regarded when using the µMORE for process optimization. Due to the accumulation of the effects mentioned above, the use of the µMORE for process development may be impaired in cases of rapid enzyme deactivation caused by the substrate(s) or even strong substrate surplus inhibition.

However, the advantages of volumetric downscale in combination with easy parallelization of the microfluidic reaction system, low enzyme loads and high flow rates allows for rapid process optimization and significantly decreasing raw materials and labour cost. Further, the potential of continuous microfluidic reactions at high flow rates and low enzyme loads was successfully demonstrated for parameter optimization of a continuous process using free enzyme in an EMR. For processes using immobilized enzyme, which are highly interesting for industrial application (chapter 1.11), the characterization of the immobilization effects on the enzyme at microscale provide another interesting application for our system.

# 5 Outlook

## 5.1 Characterization of the enzyme immobilization

Even though the capacity of the magnetic beads reported by the manufacturer for enzyme immobilization by far exceeds the amounts immobilized for the carboligation experiments (chapter 3.8), leaching of the enzyme from the beads has to be considered. Additionally the 50% reduced activity of the immobilized BFD calls for further investigation of the enzyme immobilization procedure and complete investigation of the kinetics of the immobilized enzyme. The investigation of enzyme leaching is currently limited by appropriate analytics. As common colorimetric assays as well as gel electrophoresis analysis cannot be used due to detection limits and interference, the only available option would be chromatography/MS based protein analytics (Domon and Aebersold, 2006) in order to quantify the leaching of the protein form the magnetic beads. When comparing EMR and µMORE for continuous carboligation it is necessary to further investigate leaching of the enzyme and sufficiently proof that this does not impair further application of the µMORE system for enzyme process optimization.

## 5.2 Reactor characterization

Currently, for each parameter setup only the maximum oscillation frequency of the µMORE magnetic oscillation system was tested. An optimization of the oscillation frequency and its influence on the carboligation results and enzyme inactivation may be of interest. However, due to the fact that the carboligation results indicate non optimal mixing along the length of the reaction compartment, it is likely that the fast oscillation frequency used during this thesis is the optimum operation setup for application of the actual µMORE setup. However higher oscillation frequencies could be achieved by further optimization of the magnetic layout or further decrease of the microfluidic channel width. Furthermore, additional studies on the residence time dependent enzyme inactivation should be carried out in order to verify the presented trends and to investigate whether an operating point can be reached where enzyme immobilization in the µMORE and EMR become identical. Complementary reactor simulations based on BFD reaction kinetics and benzaldehyde-induced inactivation of the BFD for the µMORE may provide further insights. An approximate model of a

non-ideal CSTR as a series of CSTR reactors may provide an adequate description of the μMORE (chapter 1.6.1).

## 5.3 Reactor chip optimization

Even though a functional microreactor system was developed and its applicability for research proven exemplarily, there is still room for further improvement of the microfluidic geometry. Further decrease in the flow cell width could be used to further increase the oscillation frequency (chapter 5.2). Additionally further optimization of the overall design concept is possible. In the current design (chip 2), the inner volume of the reaction chamber is 7.46 μL of which only 1 μL is used as actual reaction compartment in which the immobilized catalyst is moving (Figure 49a). However, especially for substrates with chemical side reactions the dead volume prior to the reaction volume plays an important role as intermixing and reaction between the two separate flows will favor any chemical side reaction. This problem could be solved by decreasing the effective reaction volume further and thus eliminate the dead volume (Figure 49b). Another possible approach is a three inlet chip, as depicted in (Figure 49c). It would allow for the connection of three syringes and features two substrate (upper and lower inlet) - and one buffer inlet in the middle. By adapting one or both substrate flows simultaneously with the buffer flow, a continuous flow rate with a controllable concentration change in one or both substrates is possible. This may enable testing of different substrate concentrations and their influence on the reaction rate in only one microreactor run. Even though this method will most likely not be useful to determine process parameters, it could be used to set first trends and determine a rough interval for further optimization. Additionally, the use of concentration profiles for process fine tuning to compensate for enzyme inactivation would be possible with this chip layout. The three inlet chip furthermore has the advantage that a buffer flow can be used to separate substrates which otherwise would react chemically before coming in contact with the enzyme retained within the mixing zone.

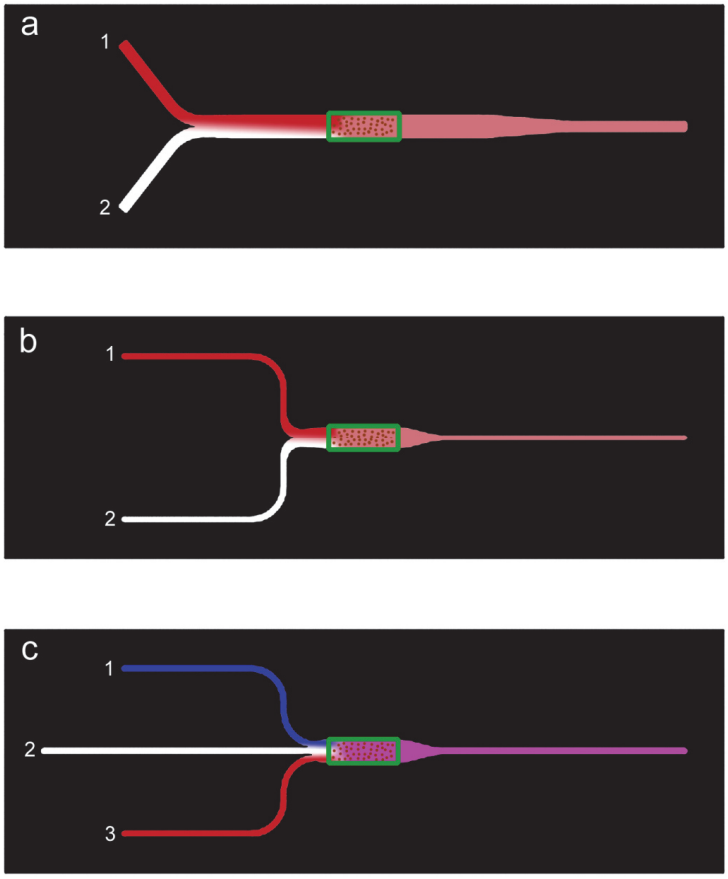


**Figure 49: Further proposed optimizations of a microfluidic chip for the µMORE. a:** Current chip design (chip 2); two substrate inlets (**1** and **2**); diffusion-based partial mixing of both inlets before fluids enter mixing zone; **b**: optimization 1: Two inlets (**1** and **2**) decreased dead volume before mixing zone results in less diffusion-based mixing of both substrate feeds before entering the mixing zone; **c**: Optimization 2: decreased dead volume as in optimization 1 but with three inlets (**1**, **2** and **3**); the flow from inlet 2 can be used to separate the substrates in inlet **1** and **3** prior to entering the mixing zone; flow rate can be maintained constant while one or both substrate flows (and thus the overall concentration of the respective substrate) can be adapted.

Novel manufacturing techniques such as foil welding and 3D printers, available for a fast number of thermoplastics, as well as micro machining have opened novel ways to manufacture microfluidic devices (Garst et al., 2005; Gerlach et al., 2002; Shallan et al., 2014). While glass serves as a gold standard for inertia and solvent resistance, the disadvantage of high cost and the fragility of glass chips have already been discussed earlier (chapter 3.5.1). An evaluation and the testing of the

resistance of different thermoplastics, which can be used to manufacture cheap disposable microfluidic chips, towards chemicals like aldehydes and organic solvents may provide an interesting alternative for glass as a substrate.

## 5.4 Analytics

Currently one of the bottlenecks of the μMORE is the HPLC analysis of the samples. On the one hand the, for microscale applications relatively large sample volume of 24 μL (24 residence times) limits the time/volume resolution of the samples as 24 μL the minimum required sample volume of the HPLC. On the other hand the analysis time of two times 20 min. per sample (multiple injection volumes to quantify products and substrates) is the main bottleneck for data generation. A second chip connected to the reactor, which incorporates the analytics, would therefore provide an interesting alternative. Different applications such as on-chip GC and on-chip HPLC and capillary gel electrophoresis have already been published (Mark et al., 2010), however the integration would result in significant costs and development time. Simple colorimetric tests for achiral analysis of α-2-hydroxyketones, such as a 2,3,5-triphenyltetrazolium chloride based colorimetric test, which enables the photometric detection (Sehl et al., 2012), provide a more realistic approach. In combination of a commercially available mixing chip (i.e. Micronit micro mixer chip) and a flow cell (i.e. Micronit microscope flow cell) with a photometric detector (i.e. a microscope with CCD camera as described in chapter 3.2 or an LED-based custom build device) achiral product analytics coupled to the microfluidic enzyme reactor could be achieved at least for the α-2-hydroxyketones. Furthermore, the use of an online microfluidic polarimeter (Rajan and Ghosh, 2012) could accomplish the data analysis by adding the stereoselective partition of the analytics. Thus, the step from a chip-in-a-lab to a-lab-on-a-chip(s) system can be achieved.

# 6 References

Abgrall, P., & Gue, A. (2007). Lab-on-chip technologies: making a microfluidic network and coupling it into a complete microsystem—a review. Journal of Micromechanics and Microengineering, 17(5), R15-R49.

Adam, W., Lazarus, M., Saha-Möller, C. R., & Schreier, P. (1999). Biocatalytic synthesis of optically active α-oxyfunctionalized carbonyl compounds. Accounts of chemical research, 837-845.

Adams, D. (1979). Hitchhiker's guide through galaxy. Pan Macmillan 2, 42.

Adrio, J. L., & Demain, A. L. (2014). Microbial Enzymes: Tools for Biotechnological Processes. Biomolecules, 4(1), 117-139.

Amelio, G. F., Tompsett M. F., & Smith G. E. (1970). Experimental verification of the charge coupled device concept. Bell System Technical Journal, 49(4), 593-600.

Ampére, A.-M. (1826). Théorie des phénomènes Électro-dynamiques. Paris: Méquinon-Marvis.

Asanomi, Y., Yamaguchi, H., Miyazaki, M., & Maeda, H. (2011). Enzyme-immobilized microfluidic process reactors. Molecules, 16(7), 6041-6059.

Baker, D. (1995). Capillary electrophoresis. Analytical Chemistry, 61(4), 292A-303A.

Baraibar, Á., Lieres, E. von, Wiechert, W., Pohl, M., & Rother, D. (2013). Effective Production of (S)-α-Hydroxy ketones: An Reaction Engineering Approach. Topics in Catalysis, 57(5), 401-411.

Barrowman, M. M., & Fewson, C. A. (1985). Phenylglyoxylate Decarboxylase and Phenylpyruvate Decarboxylase from. Current Microbiology, 12(1985), 235-240.

Barrowman, M. M., Harnett, W., Scott, A. J., Fewson, C. A., & Kusel, J. R. (1986). Immunological comparison of microbial TPP-dependent non-oxidative α-keto acid decarboxylases. FEMS Microbiology Letters, 34(1), 57-60.

Blom, M. T., Christian, M. M., Macleod Macinnes, J., & Kenneth Allen, R. W. (2010). Micromixing Chamber, Micromixer Comprising a Plurality of such Micromixing Chambers, Methods for Manufacturing thereof, and Methods for mixing. US Patent, US 2010 / 0067323 A1.

Bolivar, J., Wiesbauer, J., & Nidetzky, B. (2011). Biotransformations in microstructured reactors: more than flowing with the stream? Trends in Biotechnology, 29(7), 333-342.

Bornscheuer, U., Huisman, G., Kazlauskas, R., Lutz, S., Moore, J. C., & Robins, K. (2012). Engineering the third wave of biocatalysis. Nature, 485(7397), 185-194.

Breslow, R. (1957). Rapid Deuterium Exchange in Thiazolium Salts. Journal of the American Chemical Society, 79, 1762- 1763.

Brody, J., Yager, P., Goldstein, R., & Austin, R. (1996). Biotechnology at low Reynolds numbers. Biophysical Journal, 71(6), 3430-3441.

Bruning, M., Berheide, M., Meyer, D., Bartunik, H., Liese, A., Tittmann, K., & Golbik, R. (2009). Structural and Kinetic Studies on Native Intermediates and an Intermediate Analogue in Benzoylformate Decarboxylase Reveal a Least Motion Mechanism with an Unprecedented Short-Lived Predecarboxylation Intermediate. Biochemistry, 48(15), 3258-3268.

Buchner, E., & Rapp, R. (1897). Alkoholische Gährung ohne Hefezellen. Berichte der deutschen chemischen Gesellschaft, 30(3), 2668-2678.

Bunik, V., Tylicki, A., & Lukashev, N. (2013). Thiamin diphosphate-dependent enzymes: from enzymology to metabolic regulation, drug design and disease models. FEBS Journal, 280(24), 6412-6142.

Clouthier, C. M., & Pelletier, J. N. (2012). Expanding the organic toolbox: a guide to integrating biocatalysis in synthesis. Chemical Society Reviews, 41(4), 1585-1605.

Coughlin, R., & Charles, M. (1977). Method of carrying out enzyme catalyzed reactions. US Patent 4,048,018.

David, R. (2002). The Pyramid Builders of Acient Egypt: A Modern Investigation of Pharaoh's Workforce. Routledge 73, 148.

Demir, A. S., Pohl, M., Janzen, E., & Müller, M. (2001). Enantioselective synthesis of hydroxy ketones through cleavage and formation of acyloin linkage. Enzymatic kinetic resolution via C–C bond cleavage. Journal of the Chemical Society, Perkin Transactions 1, (7), 633-635.

Domon, B., & Aebersold, R. (2006). Mass spectrometry and protein analysis. science, 312(5771), 212-217.

Domínguez de María, P., Pohl, M., Gocke, D., Gröger, H., Trauthwein, H., Stillger, T., Walter, L., et al. (2007). Asymmetric Synthesis of Aliphatic 2-Hydroxy Ketones by Enzymatic Carboligation of Aldehydes. European Journal of Organic Chemistry, 2007(18), 2940-2944.

Dräger, G., Kiss, C., Kunz, U., & Kirschning, A. (2007). Enzyme-purification and catalytic transformations in a microstructured PASSflow reactor using a new tyrosine-based Ni-NTA linker system attached to a polyvinylpyrrolidinone-based matrix. Organic & Biomolecular Chemistry, 5(22), 3657-3664.

Dünkelmann, P., Kolter-Jung, D., Nitsch, A., Demir, A. S., Siegert, P., Lingen, B., Baumann, M., et al. (2002). Development of a Donor-Acceptor Concept for Enzymatic Cross-Coupling Reactions of Aldehydes: The First Asymmetric

Cross-Benzoin Condensation. Journal of the American Chemical Society, 124(41), 12084-12085.

Dünnwald, Thomas, Demir, A. S. S., Siegert, P., Pohl, M., & Müller, M. (2000). Enantioselective Synthesis of (S)-2-Hydroxypropanone Derivatives by Benzoylformate Decarboxylase Catalyzed C−C Bond Formation. European Journal of Organic Chemistry, 2000(11), 2161-2170.

Fagaschewski, J., Bohne, S., Kaufhold, D., Müller, J., & Hilterhaus, L. (2012). Modular micro reaction engineering for carboligation catalyzed by benzoylformate decarboxylase. Green Processing and Synthesis, 1(4), 337-344.

Fang, Q. K., Han, Z., Grover, P., Kessler, D., Senanayake, C. H., & Wald, S. A. (2000). Rapid access to enantiopure bupropion and its major metabolite by stereospecific nucleophilic substitution on an α-ketotriflate, 11, 3659-3663.

Ferreira-Torres, C., Micheletti, M., & Lye, G. J. (2005). Microscale process evaluation of recombinant biocatalyst libraries: application to Baeyer-Villiger monooxygenase catalysed lactone synthesis. Bioprocess and Biosystems Engineering, 28(2), 83-93.

Frank, H. (2004). RGB farbwuerfel.jpg. GNU Free Documentation License, Version 1.2. Retrieved from http://commons.wikimedia.org/wiki/File:RGB_farbwuerfel.jpg

Frank, R. A. W., Leeper, F. J., & Luisi, B. F. (2007). Review Structure, mechanism and catalytic duality of thiamine-dependent enzymes. Cellular and Molecular Life Sciences, 64, 892-905.

Gangolf, M., Czerniecki, J., Radermecker, M., Detry, O., Nisolle, M., Jouan, C., Martin, D., et al. (2010). Thiamine status in humans and content of phosphorylated thiamine derivatives in biopsies and cultured cells. PLoS One, 5(10), e13616.

Garst, S., Schuenemann, M., Solomon, M., Atkin, M., & Harvey, E. (2005). Fabrication of multilayered microfluidic 3D polymer packages. Proceedings Electronic Components and Technology, 1, 603-610.

Gendron, P.-O., Avaltroni, F., & Wilkinson, K. J. (2008). Diffusion coefficients of several rhodamine derivatives as determined by pulsed field gradient-nuclear magnetic resonance and fluorescence correlation spectroscopy. Journal of Fluorescence, 18(6), 1093-1101.

Gerhards, T. (2012). Einfluss unkonventioneller Medien auf die Selektivität ThDP-abhängiger Enzyme. Dissertation Heinrich Heine Universität Düsseldorf.

Gerhards, T., Mackfeld, U., Bocola, M., von Lieres, E., Wiechert, W., Pohl, M., & Rother, D. (2012). Influence of Organic Solvents on Enzymatic Asymmetric Carboligations. Advanced synthesis & catalysis, 354(14-15), 2805-2820.

Gerlach, A., Knebel, G., Guber, A. E., Heckele, M., Herrmann, A., Muslija, A., & Schaller, T. (2002). Microfabrication of single-use plastic microfluidic devices for high-throughput screening and DNA analysis. Microsystem Technologies, 7(5-6), 265-268.

Giorno, L., & Drioli, E. (2000). Biocatalytic membrane reactors: applications and perspectives. Trends in Biotechnology, 18(8), 339-349.

Gocke, D. (2010). New and optimised thiamine diphosphate ( ThDP ) -dependent enzymes for carboligation. Dissertation, Mathematisch Naturwissenschaftliche Fakultät,University Düsseldorf.

Gocke, D., Graf, T., Brosi, H., Frindi-wosch, I., Walter, L., Müller, M., & Pohl, M. (2009). Journal of Molecular Catalysis B : Enzymatic Comparative characterisation of thiamin diphosphate-dependent decarboxylases. Journal of Molecular Catalysis B: Enzymatic, 61, 30-35.

Gocke, D., Walter, L., Gauchenova, E., Kolter, G., Knoll, M., Berthold, C. L., Schneider, G., et al. (2008). Rational protein design of ThDP-dependent enzymes-engineering stereoselectivity. Chembiochem, 9(3), 406-412.

Ha, E.-J., Kim, K. K., Park, H. S., Lee, S.-G., Lee, J.-O., An, S. S. a., & Paik, H.-jong. (2012). One-step immobilization and purification of his-tagged enzyme using poly(2-acetamidoacrylic acid) hydrogel. Macromolecular Research, 21(1), 5-9.

Hailes, H. C., Rother, D., Müller, M., Westphal, R., Ward, J. M., Pleiss, J., Vogel, C., et al. (2013). Engineering stereoselectivity of ThDP-dependent enzymes. The FEBS Journal, 280(24), 6374-6394.

Hanefeld, U., Gardossi, L., & Magner, E. (2009). Understanding enzyme immobilisation. Chemical Society Reviews, 38(2), 453-468.

Hasson, M S, Muscate, a, Henehan, G. T., Guidinger, P. F., Petsko, G. a, Ringe, D., & Kenyon, G. L. (1995). Purification and crystallization of benzoylformate decarboxylase. Protein Science, 4(5), 955-959.

Hegeman, G. (1966). Synthesis of the Enzymes of the Mandelate Pathway by *Pseudomonas putida* I. Synthesis of Enzymes by the Wild Type. Journal of Bacteriology, 91(3), 1140-1154.

Helmholtz, H. (1909). Handbuch der physiologischen Optik. Hamburg: Voss. Hamburg: Leopold Voss.

Hilterhaus, L, Minow, B., Müller, J., Berheide, M., Quitmann, H., Katzer, M., Thum, O., et al. (2008). Practical application of different enzymes immobilized on sepabeads. Bioprocess and Biosystems Engineering, 31(3), 163-171.

Hochuli, E., Bannwarth, W., Döbeli, H., Gentz, R., & Stüber, D. (1988). Genetic approach to facilitate purification of recombinant proteins with a novel metal chelate adsorbent. Nature Biotechnology, 6, 1321-1325.

Hoyos, P., Sinisterra, J.-V., Molinari, F., Alcántara, A. R., & Domínguez de María, P. (2010). Biocatalytic strategies for the asymmetric synthesis of α-hydroxy ketones. Accounts of Chemical Research, 43(2), 288-299.

Hübner, G., Tittmann, K., Killenberg-Jabs, M., Schäffner, J., Spinka, M., Neef, H., Kern, D., et al. (1998). Activation of thiamin diphosphate in enzymes. Biochimica et Biophysica Acta, 1385, 221-228.

IUPAC. (2014). Compendium of Chemical Terminology 285.

Iding, H., Dünnwald, T., Greiner, L., Liese, A., Müller, M., Siegert, P., Grötzinger, J., et al. (2000). Benzoylformate decarboxylase from *Pseudomonas putida* as stable catalyst for the synthesis of chiral 2-hydroxy ketones. Chemistry, 6(8), 1483-1495.

Illanes, A. (2008). Enzyme Biocatalysis Principles and Applications. Principles and Applications, Springer Science 207-210.

Jackson, J. D., Müller, K., & Witte, C. (1999). Klassische Elektrodynamik (4th ed.). Berlin, New York: Walter de Gruyter.

Jiménez-González, C., Poechlauer, P., Broxterman, Q. B., Yang, B.-S., am Ende, D., Baird, J., Bertsch, C., et al. (2011). Key Green Engineering Research Areas for Sustainable Manufacturing: A Perspective from Pharmaceutical and Fine Chemicals Manufacturers. Organic Process Research & Development, 15(4), 900-911.

Johannes, T. W., & Zhao, H. (2006). Directed evolution of enzymes and biosynthetic pathways. Current Opinion in Microbiology, 9(3), 261-267.

Jordan, F. (2003). Current mechanistic understanding of thiamin diphosphate-dependent enzymatic reactions. Natural Product Reports, 20(2), 184-201.

Kihumbu, D. (2007). Stereoselektive Diolsynthese mit Lyasen und Oxidoreduktasen – Entwicklung eines kontinuierlichen Verfahrens. Rheinischen Friedrich-Wilhelms-Universität Bonn.

Kintses, B., van Vliet, L. D., Devenish, S. R. a, & Hollfelder, F. (2010). Microfluidic droplets: new integrated workflows for biological experiments. Current Opinion in Chemical Biology, 14(5), 548-555.

Knoll, M., Müller, M., Pleiss, J., & Pohl, M. (2006). Factors mediating activity, selectivity, and substrate specificity for the thiamin diphosphate-dependent enzymes benzaldehyde lyase and benzoylformate decarboxylase. Chembiochem, 7(12), 1928-1934.

Krampitz, L., & Greull, G. (1958). An active acetaldehyde-thiamine intermediate. Journal of the American Chemical Society, 188(3), 5893-5894.

Krenková, J., & Foret, F. (2004). Immobilized microfluidic enzymatic reactors. Electrophoresis, 25(21-22), 3550-3563.

Kuo, J. S., & Chiu, D. T. (2011). Controlling mass transport in microfluidic devices. Annual review of analytical chemistry (Palo Alto, Calif.), 4(1), 275-296.

Kurlemann, N., & Liese, A. (2004). Immobilization of benzaldehyde lyase and its application as a heterogeneous catalyst in the continuous synthesis of a chiral 2-hydroxy ketone. Tetrahedron: Asymmetry, 15(18), 2955-2958.

Lasance, C. J. M. (2001). The thermal conductivity of unfilled plastics. Electronics cooling, (7) 22-23.

Lee, S. H., van Noort, D., Lee, J. Y., Zhang, B.-T., & Park, T. H. (2009). Effective mixing in a microfluidic chip using magnetic particles. Lab on a chip, 9(3), 479-482.

Li, Y., Xu, X., Yan, B., Deng, C., Yu, W., Yang, P., & Zhang, X. (2007). Microchip reactor packed with metal-ion chelated magnetic silica microspheres for highly efficient proteolysis. Journal of proteome research, 6(6), 2367-2375.

Lim, Y., Kouzani, A., & Duan, W. (2010). Lab-on-a-chip : a component view. Microsystem Technologies, 16(12), 1995-2015.

Lima-Ramos, J., Neto, W., & Woodley, J. M. (2013). Engineering of Biocatalysts and Biocatalytic Processes. Topics in Catalysis, 57(5), 301-320.

Liu, Z. H., Li, J. P., Guan, W. H., & Yang, S. (2011). The Temperature Field Finite Element Analysis and Simulation of One Kind of Magnetic Agitation System. Advanced Materials Research, 422, 365-369.

Lloyd R. Snyder, Joseph J. Kirkland, J. W. D. (2010). Introduction to Modern Liquid Chromatography, Third Edition. John Wiley & Sons, Inc.

Lottspeich, Friedrich, Engels, J. W. (2006). Bioanalytik. Springer 257.

Lund-Olesen, T., Buus, B. B., Howalt, J. G., & Hansen, M. F. (2008). Magnetic bead micromixer: Influence of magnetic element geometry and field amplitude. Journal of Applied Physics, 103(7), 07E902.

Maraite, A., Schmidt, T., Ansörge-Schumacher, M. B., Brzozowski, A. M., & Grogan, G. (2007). Structure of the ThDP-dependent enzyme benzaldehyde lyase refined to 1.65 A resolution. Acta crystallographica. Section F, Structural Biology and Crystallization Communications, 63(Pt 7), 546-548.

Margulies, M., Egholm, M., Altman, W. E., Attiya, S., Bader, J. S., Bemben, L. A., Berka, J., et al. (2005). Genome sequencing in microfabricated high-density picolitre reactors. Nature, 437(September), 376-381.

Mark, D., Haeberle, S., Roth, G., von Stetten, F., & Zengerle, R. (2010). Microfluidic lab-on-a-chip platforms: requirements, characteristics and applications. Chemical Society reviews, 39(3), 1153-1182.

Matosevic, S., Lye, G. J., & Baganz, F. (2009). Design and characterization of a prototype enzyme microreactor: quantification of immobilized transketolase kinetics. Biotechnology progress, 26(1), 118-126.

McCalla, S. E., & Tripathi, A. (2011). Microfluidic reactors for diagnostics applications. Annual review of biomedical engineering, 13, 321-343.

Meyer, H., Eichhorn, E., Hanlon, S., Lütz, S., M, S., Wohlgemuth, R., & Coppolecchia, R. (2013). The use of enzymes in organic synthesis and the life sciences: perspectives from the Swiss Industrial Biocatalysis Consortium (SIBC). Catalysis Science & Technology, 3, 29-40.

Micheletti, M., & Lye, G. J. (2006). Microscale bioprocess optimisation. Current opinion in biotechnology, 17(6), 611-618.

Miyazaki, M., & Maeda, H. (2006). Microchannel enzyme reactors and their applications for processing. Trends in Biotechnology, 24(10), 463-470.

Mosbacher, T. G., Müller, M., & Schulz, G. E. (2005). Structure and mechanism of the ThDP-dependent benzaldehyde lyase from Pseudomonas fluorescens. The FEBS Journal, 272, 6067-6076.

Muller, Y. a, & Schulz, G. E. (1993). Structure of the thiamine- and flavin-dependent enzyme pyruvate oxidase. Science, 259(5097), 965-967.

Mullis, K. B. (1985). Process for amplifying nucleic acids. US Patent, 4,683,202.

Müller, M., Gocke, D., & Pohl, M. (2009). Thiamin diphosphate in biological chemistry: exploitation of diverse thiamin diphosphate-dependent enzymes for asymmetric chemoenzymatic synthesis. The FEBS Journal, 276(11), 2894-2904.

Müller, M, Sprenger, G. A, & Pohl, M. (2013). C-C bond formation using ThDP-dependent lyases. Current Opinion in Chemical Biology, 17(2), 261-270.

Neuži, P., Giselbrecht, S., Länge, K., Huang, T. J., & Manz, A. (2012). Revisiting lab-on-a-chip technology for drug discovery. Nature reviews. Drug discovery, 11(8), 620-632.

Nieba, L., Nieba-Axmann, S. E., Persson, a, Hämäläinen, M., Edebratt, F., Hansson, a, Lidholm, J., et al. (1997). BIACORE analysis of histidine-tagged proteins using a chelating NTA sensor chip. Analytical biochemistry, 252(2), 217-228.

Nomura, A., Shin, S., Mehdi, O. O., & Kauffmann, J.-M. (2004). Preparation, characterization, and application of an enzyme-immobilized magnetic microreactor for flow injection analysis. Analytical Chemistry, 76(18), 5498-5502.

Peper, S., Kara, S., Long, W. S., Liese, A., & Niemeyer, B. (2011). Immobilization and characterization of benzoylformate decarboxylase from *Pseudomonas putida* on spherical silica carrier. Bioprocess and Biosystems Engineering, 34(6), 671-680.

Pohar, A., Plazl, I., & Znidarsic-Plazl, P. (2009). Lipase-catalyzed synthesis of isoamyl acetate in an ionic liquid/n-heptane two-phase system at the microreactor scale. Lab on a chip, 9(23), 3385-3390.

Pohl M., Gocke D., Müller M., (2009)Thiamine-Based Enzymes for Biotransformations Anastas, P. T. & Crabtree, R. H. (ed.), Handbook of Green Chemistry-Green Catalysis Vol. 3. (3rd ed.). Weinheim: Wiley-VCH 75-114.

Pollard, D. J., & Woodley, J. M. (2007). Biocatalysis for pharmaceutical intermediates: the future is now. Trends in biotechnology, 25(2), 66-73.

Polovnikova, E. S., McLeish, M. J., Sergienko, E. a, Burgner, J. T., Anderson, N. L., Bera, A. K., Jordan, F., et al. (2003). Structural and kinetic analysis of catalysis by a thiamin diphosphate-dependent enzyme, benzoylformate decarboxylase. Biochemistry, 42(7), 1820-1830.

Rajan, R., & Ghosh, A. (2012). Demonstration of a microfluidic polarimeter. Measurement. Conference on Frontiers in Biological Detection - From Nanosensors to Systems IV, San Francisco, CA.

Rao, N. N., Lütz, S., Würges, K., & Minör, D. (2009). Continuous Biocatalytic Processes. Organic Process Research & Development, 13(3), 607-616.

Reynolds, O. (1883). An experimental investigation of the circumstances which determine whether the motion of water shall be direct or sinuous, and of the law of resistance in parallel. Proceedings of the Royal Society of London, 84-99.

Rios, G. M., Belleville, M. P., Paolucci, D., & Sanchez, J. (2004). Progress in enzymatic membrane reactors – a review. Journal of Membrane Science, 242(1-2), 189-196.

Robertson, C. W., & Box, P. O. (2003). Liquid Photometer Using Surface Tension to Contain Samples. US US6628382 B2.

Saehuan, C., Rojanarata, T., Wiyakrutta, S., McLeish, M. J., & Meevootisom, V. (2007). Isolation and characterization of a benzoylformate decarboxylase and a $NAD^+$/$NADP^+$-dependent benzaldehyde dehydrogenase involved in D-phenylglycine metabolism in *Pseudomonas stutzeri* ST-201. Biochimica et Biophysica Acta, 1770(11), 1585-1592.

Schmid, A., Dordick, J. S., Hauer, B., Kiener, A., Wubbolts, M., & Witholt, B. (2001). Industrial Biocatalysis Today and Tomorrow. Nature, 409(6817), 258-268.

Schäpper, D., Alam, M. N. H. Z., Szita, N., Eliasson Lantz, A., & Gernaey, K. V. (2009). Application of microbioreactors in fermentation process development: a review. Analytical and bioanalytical chemistry, 395(3), 679-695.

Sehl, T., Hailes, H. C., Ward, J. M., Wardenga, R., von Lieres, E., Offermann, H., Westphal, R., et al. (2013). Two Steps in One Pot: Enzyme Cascade for the Synthesis of Nor(pseudo)ephedrine from Inexpensive Starting Materials. Angewandte Chemie International Edition, 52(26), 6772-6775.

Sehl, T., Simon, R. C., Hailes, H. C., Ward, J. M., Schell, U., Pohl, M., & Rother, D. (2012). TTC-based screening assay for ω-transaminases: a rapid method to detect reduction of 2-hydroxy ketones. Journal of Biotechnology, 159(3), 188-194. Elsevier B.V.

Seong, G. H., & Crooks, R. M. (2002). Efficient mixing and reactions within microfluidic channels using microbead-supported catalysts. Journal of the American Chemical Society, 124(45), 13360-13361.

Shallan, A. I., Smejkal, P., Corban, M., Guijt, R. M., & Breadmore, M. C. (2014). Cost-Effective Three-Dimensional Printing of Visibly Transparent Microchips within Minutes. Analytical Chemistry, 86(6), 3124-3130.

Sheldon, R. A, & van Pelt, S. (2013). Enzyme immobilisation in biocatalysis: why, what and how. Chemical Society reviews, 42(15), 6223-6235.

Sheldon, R. A. (2007). Enzyme Immobilization: The Quest for Optimum Performance. Advanced Synthesis & Catalysis, 349(8-9), 1289-1307.

Sheldon, R. A., Schoevaart, R., & Van Langen, L. M. (2005). Cross-linked enzyme aggregates (CLEAs): A novel and versatile method for enzyme immobilization (a review). Biocatalysis and Biotransformation, 23(3-4), 141-147.

Shendure, J., & Ji, H. (2008). Next-generation DNA sequencing. Nature Biotechnology, 26(10), 1135-1145.

Sprenger, G. A., & Pohl, M. (1999). Synthetic potential of thiamin diphosphate-dependent enzymes. Journal of Molecular Catalysis B: Enzymatic, 6(3), 145-159.

Squires, T. M. (2005). Microfluidics : Fluid physics at the nanoliter scale. Reviews of Modern Physics, 77(3), 977-1026.

Srinivasan, A., Bach, H., Sherman, D. H., & Dordick, J. S. (2004). Bacterial P450-catalyzed polyketide hydroxylation on a microfluidic platform. Biotechnology and Bioengineering, 88(4), 528-535.

Stokes, G. (1851). On the effect of the internal friction of fluids on the motion of pendulums. Transactions of the Cambridge Philosophical Society (9) 8-94.

Stone, H. a., Stroock, A. D., & Ajdari, A. (2004). Engineering Flows in Small Devices. Annual Review of Fluid Mechanics, 36(1), 381-411.

Sumner, J. B. (1926). The isolation and characterization of the enzyme urease. Journal of Biological Chemistry, 69, 435-441.

Sun, T., & Morgan, H. (2010). Single-cell microfluidic impedance cytometry: a review. Microfluidics and Nanofluidics, 8(4), 423-443.

Tables of Physical & Chemical Constants 2.6.6 Magnetic properties of materials. (1995). Online, Kaye & Laby. Retrieved from www.kyelaby-npl.co.uk

Tanaka, T., Kawase, M., & Tani, S. (2004). α-Hydroxyketones as inhibitors of urease. Bioorganic & Medicinal Chemistry, 12(2), 501-505.

Tischer, W., & Kasche, V. (1999). Immobilized enzymes: crystals or carriers? Trends in Biotechnology, 17(8), 326-335.

Tufvesson, P., Lima-Ramos, J., Haque, N. A., Gernaey, K. V., & Woodley, J. M. (2013). Advances in the Process Development of Biocatalytic Processes. Organic Process Research & Development, 17(10), 1233-1238.

Tural, B., Tural, S., & Demir, A. S. (2013). Carboligation reactions mediated by benzoylformate decarboxylase immobilized on a magnetic solid support. Chirality, 25(7), 415-421.

Urban, P. L., Goodall, D. M., & Bruce, N. C. (2006). Enzymatic microreactors in chemical analysis and kinetic studies. Biotechnology advances, 24(1), 42-57.

Valinger, D., Presečki, A. V., Kurtanjek, Ž., Pohl, M., Blažević, Z. F., & Vasić-Rački, Đ. (2014). Continuous enzymatic carboligation of benzaldehyde and acetaldehyde in an enzyme ultrafiltration membrane reactor and laminar flow microreactors. Journal of Molecular Catalysis B: Enzymatic (102) 132-137.

Van Erdeghem, P., Logist, F., Dittrich, C., & Van Impe, J. (2011). Detailed steady-state simulation of tubular reactors for LDPE production: plug flow versus cascaded CSTR model. Proceedings of the 18th IFAC World Congress, 477-482.

Verbarg, J., Kamgar-Parsi, K., Shields, A. R., Howell, P. B., & Ligler, F. S. (2012). Spinning magnetic trap for automated microfluidic assay systems. Lab on a chip, 12(10), 1793-1799.

Wallace, O. B., Smith, D. W., Deshpande, M. S., Polson, C., & Felsenstein, K. M. (2003). Inhibitors of Aβ production: Solid-Phase Synthesis and SAR of α-Hydroxycarbonyl Derivatives. Bioorganic & Medicinal Chemistry Letters, 13(6), 1203-1206.

Wandrey, C. (1979). Continuous Homogeneous Catalysis in Enzyme Engineering. Annals of the New York Academy of Sciences, 326, 87-95.

Wang, C. Y. (1991). Exact Solutions of the Steady-State Navier-Stokes Equations. Annual Review of Fluid Mechanics, 23(1), 159-177.

Wang, L., & Li, P. C. H. (2011). Microfluidic DNA microarray analysis: a review. Analytica chimica acta, 687(1), 12-27.

Wang, Y., Zhe, J., Chung, B. T. F., & Dutta, P. (2007). A rapid magnetic particle driven micromixer. Microfluidics and Nanofluidics, 4(5), 375-389.

Watson, J., & Crick, F. (1953). Molecular structure of nucleic acids. Nature, 171, 737-738.

Wendorff, M. (2006). Neue Benzoylformiatdecarboxylasen für die Biokatalyse. Dissertation, Mathematisch- Naturwissenschaftliche Fakultät, Heinrich-Heine-Universität Düsseldorf.

Werts, M. H. V., Raimbault, V., Texier-Picard, R., Poizat, R., Français, O., Griscom, L., & Navarro, J. R. G. (2012). Quantitative full-colour transmitted light microscopy and dyes for concentration mapping and measurement of diffusion coefficients in microfluidic architectures. Lab on a chip, 12(4), 808-820.

Westphal, R., Waltzer, S., Mackfeld, U., Widmann, M., Pleiss, J., Beigi, M., Müller, M., et al. (2013). (*S*)-Selective MenD variants from *Escherichia coli* provide access to new functionalized chiral α-hydroxy ketones. Chemical communications (Cambridge, England), 49(20), 2061-2063.

Whitesides, G. M. (2006). The origins and the future of microfluidics. Nature, 442(7101), 368-373.

Wilcocks, R., Ward, O. P., Collins, S., Dewdney, N. J., Hong, Y., & Prosen, E. (1992). Acyloin formation by benzoylformate decarboxylase from *Pseudomonas putida*.Applied and Envinronmental Microbiology., 58(5), 1699-1704.

Woodley, J. M. (2012). Reaction and process engineering. In K. Drauz, H. Gröger, & O. May (Eds.), Enzyme Catalysis in Organic Chemistry; (3rd ed.). Weinheim: Wiley-VCH 217-242.

Woodley, J. M., Breuer, M., & Mink, D. (2013). A future perspective on the role of industrial biotechnology for chemicals production. Chemical Engineering Research and Design, 91(10), 2029-2036. Institution of Chemical Engineers.

Yep, A., & McLeish, M. J. (2009). Engineering the substrate binding site of benzoylformate decarboxylase. Biochemistry, 48(35), 8387-8395.

Zhang, Y., Yang, Y., Ma, W., Guo, J., Lin, Y., & Wang, C. (2013). Uniform Magnetic Core / Shell Microspheres Functionalized with $Ni^{2+}$ − Iminodiacetic Acid for One Step Puri fi cation and Immobilization of His-Tagged Enzymes, 5(7), 2626-2633.

Zhang, Z., Boccazzi, P., Choi, H.-G., Perozziello, G., Sinskey, A. J., & Jensen, K. F. (2006). Microchemostat-microbial continuous culture in a polymer-based, instrumented microbioreactor. Lab on a Chip, 6(7), 906-913.

van Pelt, Stijn, Derks, R., Matteucci, M., Hansen, M. F., & Dietzel, A. (2011). Flow-orthogonal bead oscillation in a microfluidic chip with a magnetic anisotropic flux-guide array. Biomedical Microdevices, 13(2), 353-359.

Šalić, A., Ivanković, M., Ferk, E., & Zelić, B. (2013). ADH based $NAD^+$ regeneration in a microreactor. Journal of Chemical Technology & Biotechnology, 88(9), 1721-1729.

# 7 Appendix

## 7.1 Python scripts for image analysis

```
#Combined Script
#!/usr/bin/env python
#ALL PICTURES IN SOURCE FOLDER WILL BE DELETED WHILE RUNNING THIS SCRIPT!
                                                    #report current processing step
import re
import os
from PIL import Image
print "Processing filewalker!"
SOURCE_PATH = "G:\\Python\\source\\"                          #define source folder
OUTPUT_PATH = "g:\\Python\\cache_1"                           #define cache folder 1
for file_name in os.listdir(SOURCE_PATH):                     #loop for all directories in source
   IMG_PATH = (os.path.join(SOURCE_PATH, file_name)           #define path of images in current image directory
   print "Walking folder " + file_name + "!"                  #print processing status current folder
   new_basename = file_name                  #define basename of renamed pictures as name of parent directory
   a=0                                                        #define number of picture in directory
   for file_name in os.listdir(IMG_PATH):                     #loop for all files in directory
        a += 1                                                #increase number of picture in directory
        file_name_split = os.path.splitext(file_name)         #get file type
        new_filename = (new_basename + str(a).zfill(2) + file_name_split[1])      #define new picture filename as directory
name + picture number + filetype
        os.rename(os.path.join(IMG_PATH, file_name), (os.path.join(OUTPUT_PATH, new_filename))          #perform
renaming operation
size = 200, 133
for infile in os.listdir(SOURCE_PATH)("*.jpg"):
   file, ext = os.path.splitext(infile)
   im = Image.open(infile)
   im.thumbnail(size, Image.ANTIALIAS)
   im.save(file, "JPEG")
print "Processing greyscale reduction"
IMG_PATH = "g:\\Python\\cache_1"
OUTPUT_PATH_GREYSCALE = "g:\\Python\\cache_2\\greyscale"      #define output path greyscale
WIDTH = 4608
HEIGHT = 3072
import os
import sys
import Image
for filename in os.listdir(IMG_PATH):                         #apply for all files in folder
   im = Image.open(os.path.join(IMG_PATH, filename)           #open file
   im = im.rotate(1)                                          #rotate file by 1°
   im = im.convert("L")                                       #convert file to greyscale
   im.save (os.path.join(OUTPUT_PATH_GREYSCALE, filename), "JPEG")   #save file in OUTPUT_PATH
print "reduction to greyscale completed"
IMG_PATH = "g:\\Python\\cache_1"
OUTPUT_PATH_R = "g:\\Python\\cache_2\\R"                      #define output path red
OUTPUT_PATH_G = "g:\\Python\\cache_2\\G"                      #define output path green
```

```
OUTPUT_PATH_B = "g:\\Python\\cache_2\\B"                    #define output path blue

print "Processing red channel seperation!"
for filename in os.listdir(IMG_PATH):                       #apply for all files in folder
   im = Image.open(os.path.join(IMG_PATH, filename)         #open image
   im.load()                                                #load image
   r,g,b = im.split()                                       #split image to individual color bands
   r.rotate(1)                                              #rotate red channel by 1°
   r.save (os.path.join(OUTPUT_PATH_R, filename), "JPEG")   #save red channel in OUTPUT_PATH_R
print "Red channel seperation completed!"
print "Processing green channel seperation!"
for filename in os.listdir(IMG_PATH):                       #apply for all files in folder
   im = Image.open(os.path.join(IMG_PATH, filename)          #open image
   im.load()                                                #load image
   r,g,b = im.split()                                       #split image to individual color bands
   g.rotate(1)                                              #rotate green channel by 1°
   g.save (os.path.join(OUTPUT_PATH_G, filename), "JPEG")   #save red channel in OUTPUT_PATH_R
print "Green channel seperation completed!"
print "Processing blue channel seperation!"
for filename in os.listdir(IMG_PATH):                       #apply for all files in folder
   im = Image.open(os.path.join(IMG_PATH, filename)         #open image
   im.load()                                                #load image
   r,g,b = im.split()                                       #split image to individual color bands
   b.rotate(1)                                              #rotate blue channel by 1°
   b.save (os.path.join(OUTPUT_PATH_B, filename), "JPEG")   #save red channel in OUTPUT_PATH_R
print "Blue channel seperation completed!"
IMG_PATH_GREYSCALE = "g:\\Python\\cache_2\\greyscale"       #define processing input path
IMG_PATH_R = "g:\\Python\\cache_2\\R"
IMG_PATH_G = "g:\\Python\\cache_2\\G"
IMG_PATH_B = "g:\\Python\\cache_2\\B"
OUTPUT_CSV_GREYSCALE = "g:\\Python\\output_greyscale.csv"   #define processing output files
OUTPUT_CSV_R = "g:\\Python\\output_R.csv"
OUTPUT_CSV_G = "g:\\Python\\output_G.csv"
OUTPUT_CSV_B = "g:\\Python\\output_B.csv"
MARGIN_WIDTH = 0                                            #define margin width
MARGIN_HEIGTH = 0                                           #define margin heigth
WIDTH = 200 - MARGIN_WIDTH                                  #define width
HEIGHT = 133 - MARGIN_HEIGTH                                #define heigth
print "Processing pixel readout greyscale!"
out_file = open(OUTPUT_CSV_GREYSCALE, "w")                  #open output file
for filename in os.listdir(IMG_PATH_GREYSCALE):
   im = Image.open(os.path.join(IMG_PATH_GREYSCALE, filename)#open image
   values = [filename]
   for x in range(MARGIN_WIDTH, WIDTH):                     #readout pixel data
      c = 0
      for y in range(MARGIN_HEIGTH, HEIGHT):
         c += im.getpixel(x, y)
      values.append(str(float(c) / HEIGHT-MARGIN_HEIGTH)
   out_file.write(";".join(values) + "\n")                  #safe data to file
out_file.close()
```

```
print "Pixel readout greyscale completed!"
print "Processing pixel readout red channel!"
out_file = open(OUTPUT_CSV_R, "w")                    #open output file
for filename in os.listdir(IMG_PATH_R):
    im = Image.open(os.path.join(IMG_PATH_R, filename)    #open image
    values = [filename]
    for x in range(MARGIN_WIDTH, WIDTH):              #readout pixel data
        c = 0
        for y in range(MARGIN_HEIGTH, HEIGHT):
            c += im.getpixel(x, y)
        values.append(str(float(c) / HEIGHT-MARGIN_HEIGTH)
    out_file.write(";".join(values) + "\n")           #safe data to file
out_file.close()
print "Pixel readout red channel completed!"
print "Processing pixel green channel!"
out_file = open(OUTPUT_CSV_G, "w")                    #open output file
for filename in os.listdir(IMG_PATH_G):
    im = Image.open(os.path.join(IMG_PATH_G, filename)    #open image
    values = [filename]
    for x in range(MARGIN_WIDTH, WIDTH):              #readout pixel data
        c = 0
        for y in range(MARGIN_HEIGTH, HEIGHT):
            c += im.getpixel(x, y)
        values.append(str(float(c) / HEIGHT-MARGIN_HEIGTH)
    out_file.write(";".join(values) + "\n")           #safe data to file
out_file.close()
out_file = open(OUTPUT_CSV_B, "w")
print "Pixel readout green channel completed!"
print "Processing pixel blue channel!"
out_file = open(OUTPUT_CSV_B, "w")                    #open output file
for filename in os.listdir(IMG_PATH_B):
    im = Image.open(os.path.join(IMG_PATH_B, filename)    #open image
    values = [filename]
    for x in range(MARGIN_WIDTH, WIDTH):              #readout pixel data
        c = 0
        for y in range(MARGIN_HEIGTH, HEIGHT):
            c += im.getpixel(x, y)
        values.append(str(float(c) / HEIGHT-MARGIN_HEIGTH)
    out_file.write(";".join(values) + "\n")           #safe data to file
out_file.close()
print "Pixel readout blue channel completed!"
print "DON'T PANIC, THE ANSWER IS 42!"  # (Adams, 1979)
```

## 7.2 Detailed carboligation reaction data

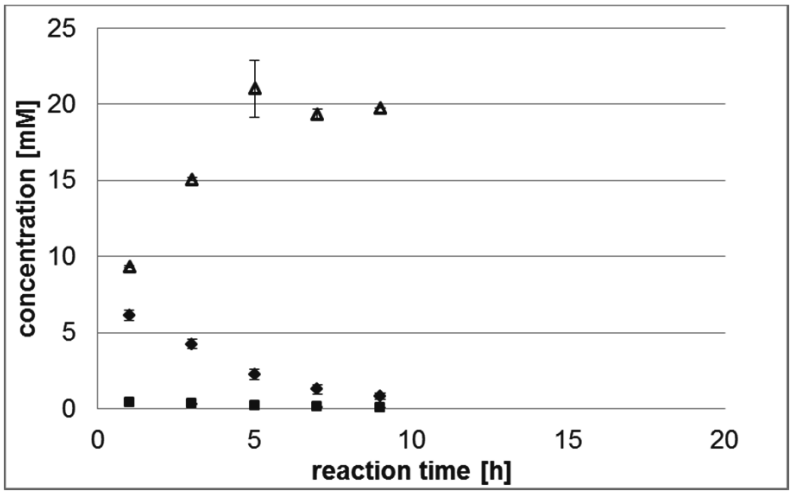


**Figure 50: Reaction data for the µMORE at pH 6.5; 250 mM acetaldehyde; 25 mM benzaldehyde 30°C (◆ (*S*)-HPP; ■ (*R*)-HPP ▲ benzaldehyde). Enzyme load: 1 µg on 0.5 µL beads; Flow rate 24 µL/h. For detailed reaction parameters please refer to Table 7.**

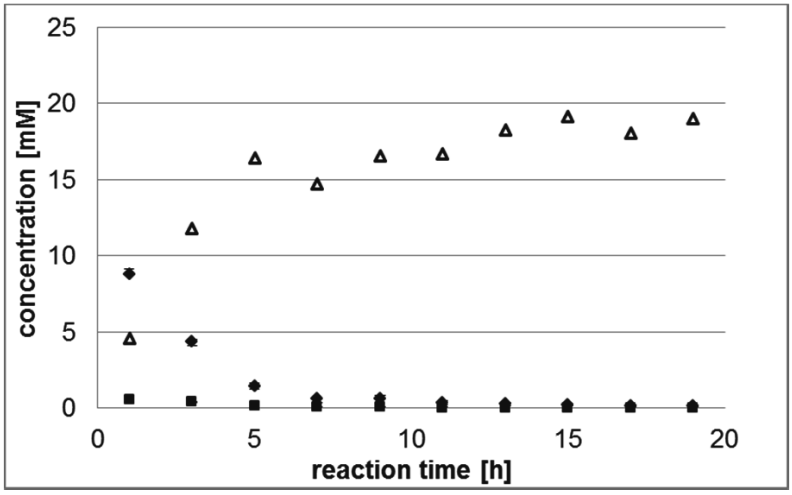


**Figure 51: Reaction data for the µMORE at pH 7.0; 250 mM acetaldehyde; 25 mM benzaldehyde 30°C (◆ (*S*)-HPP; ■ (*R*)-HPP ▲ benzaldehyde). Enzyme load: 1 µg on 0.5 µL beads; flow rate 24 µL/h. For detailed reaction parameters please refer to Table 7.**

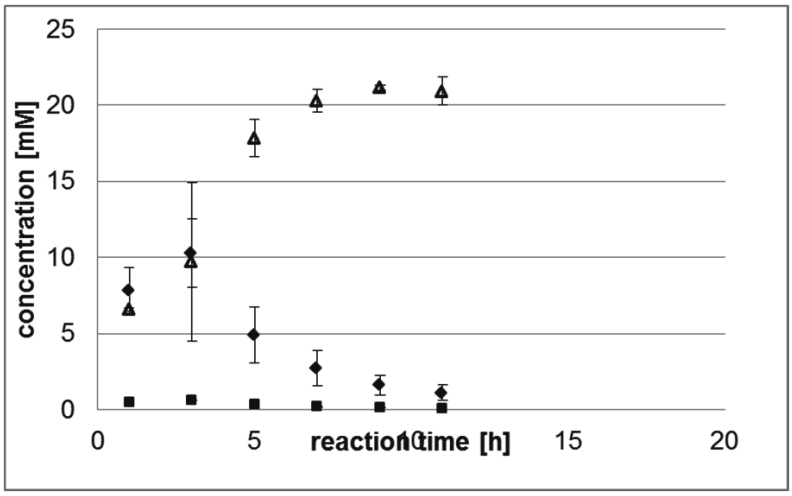


**Figure 52: Reaction data for the µMORE at pH 7.5; 250 mM acetaldehyde; 25 mM benzaldehyde 30°C (◆ (*S*)-HPP; ■ (*R*)-HPP ▲ benzaldehyde). Enzyme load: 1 µg on 0.5 µL beads; flow rate 24 µL/h. For detailed reaction parameters please refer to Table 7.**

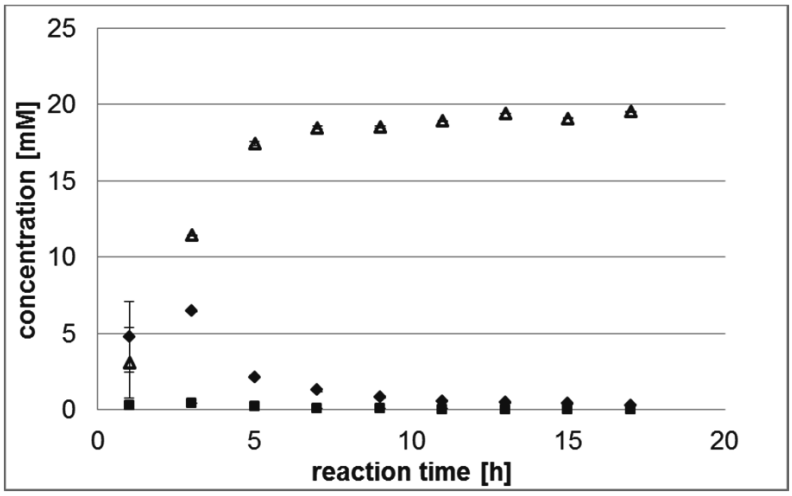


**Figure 53: Reaction data for the µMORE at pH 8.0; 250 mM acetaldehyde; 25 mM benzaldehyde 30°C (◆ (*S*)-HPP; ■ (*R*)-HPP ▲ benzaldehyde). Enzyme load: 1 µg on 0.5 µL beads; Flow rate 24 µL/h. For detailed reaction parameters please refer to Table 7.**

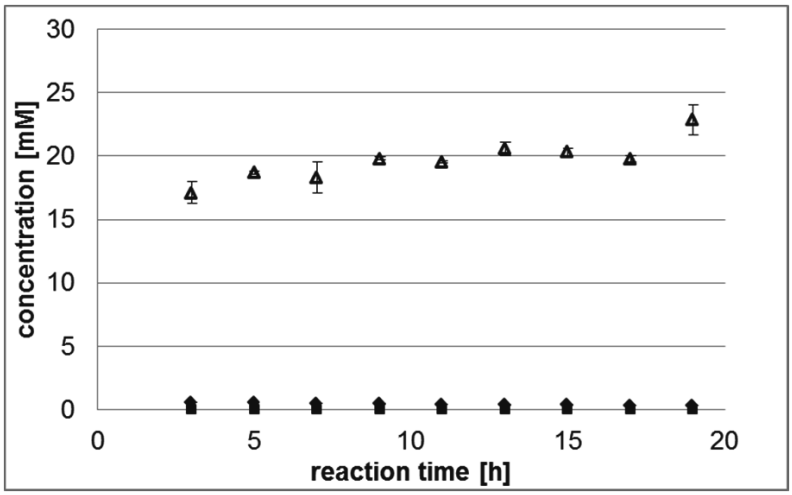


**Figure 54: Reaction data for the µMORE at pH 6.5; 250 mM acetaldehyde; 25 mM benzaldehyde 10°C (◆ (*S*)-HPP; ■ (*R*)-HPP ▲ benzaldehyde). Enzyme load: 1 µg on 0.5 µL beads; Flow rate 24 µL/h. For detailed reaction parameters please refer to Table 7.**

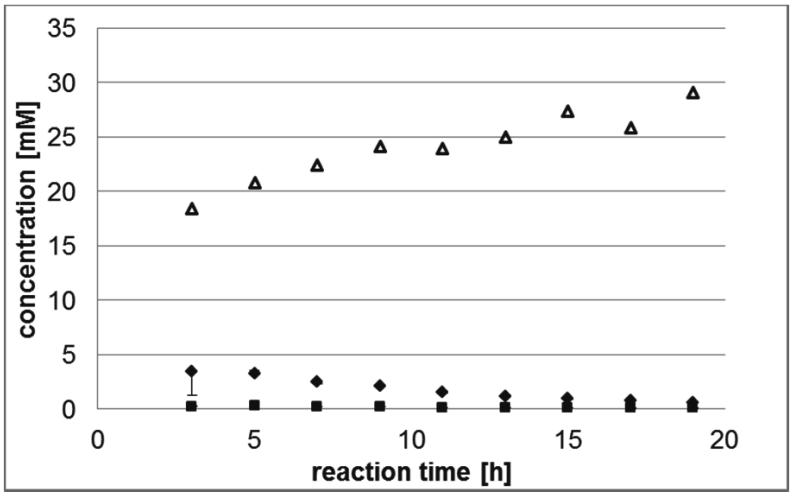


**Figure 55: Reaction data for the µMORE at pH 6.5; 250 mM acetaldehyde; 25 mM benzaldehyde 20°C (◆ (*S*)-HPP; ■ (*R*)-HPP ▲ benzaldehyde). Enzyme load: 1 µg on 0.5 µL beads; Flow rate 24 µL/h. For detailed reaction parameters please refer to Table 7.**

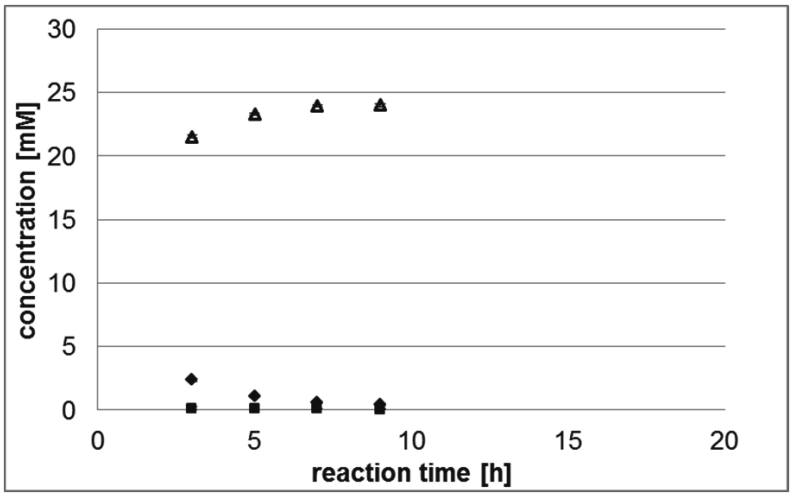


**Figure 56: Reaction data for the µMORE at pH 6.5; 250 mM acetaldehyde; 25 mM benzaldehyde 40°C (◆ (*S*)-HPP; ■ (*R*)-HPP ▲ benzaldehyde). Enzyme load: 1 µg on 0.5 µL beads; Flow rate 24 µL/h. For detailed reaction parameters please refer to Table 7.**

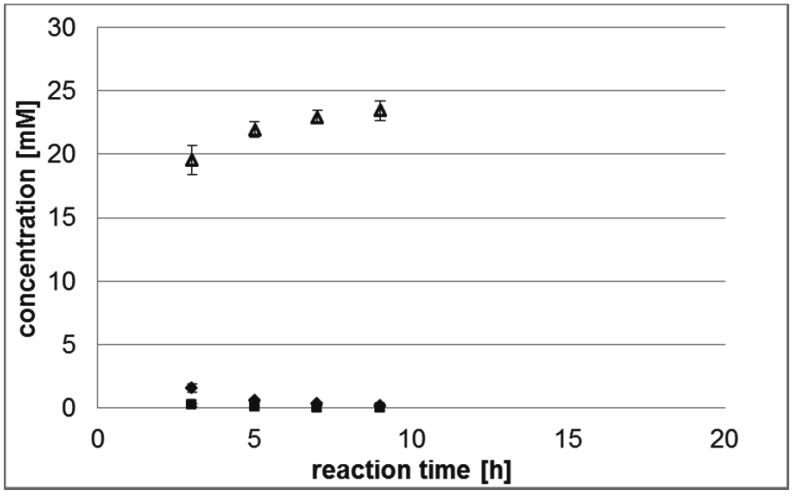


**Figure 57: Reaction data for the µMORE at pH 6.5; 250 mM acetaldehyde; 25 mM benzaldehyde 50°C (◆ (*S*)-HPP; ■ (*R*)-HPP ▲ benzaldehyde). Enzyme load: 1 µg on 0.5 µL beads; Flow rate 24 µL/h. For detailed reaction parameters please refer to Table 7.**

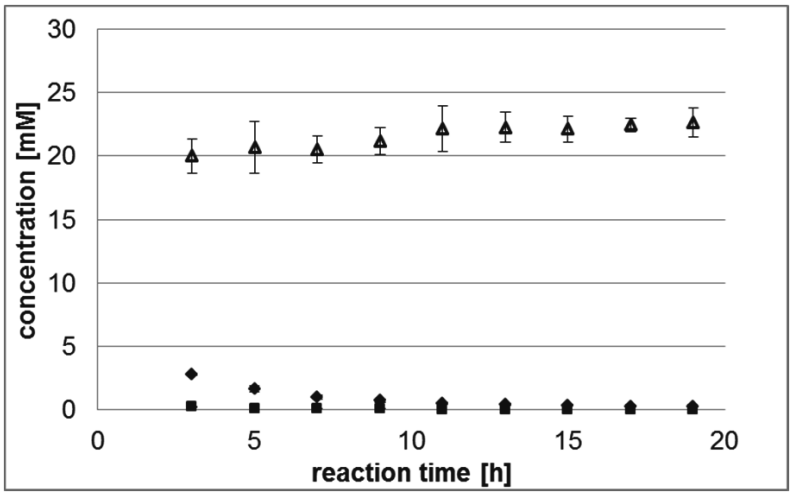


**Figure 58: Reaction data for the µMORE at pH 7.5; 50 mM acetaldehyde; 25 mM benzaldehyde 20°C (◆ (*S*)-HPP; ■ (*R*)-HPP ▲ benzaldehyde). Enzyme load: 1 µg on 0.5 µL beads; Flow rate 24 µL/h. For detailed reaction parameters please refer to Table 7.**

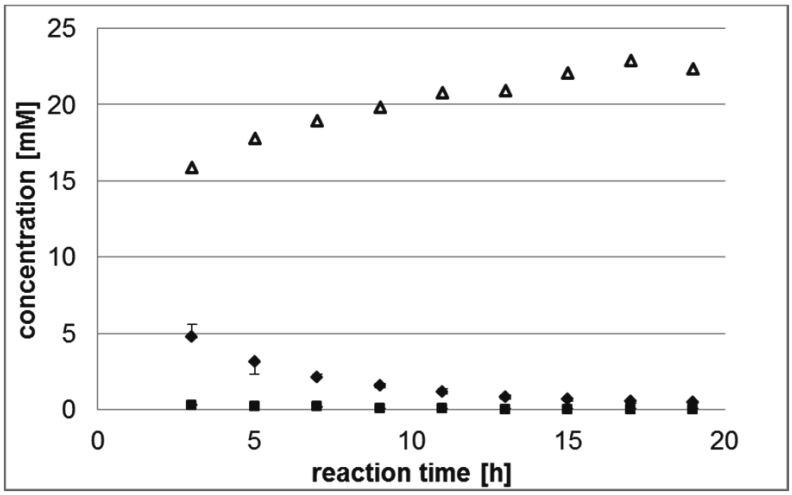


**Figure 59: Reaction data for the µMORE at pH 7.5; 100 mM acetaldehyde; 25 mM benzaldehyde 20°C (◆ (*S*)-HPP; ■ (*R*)-HPP ▲ benzaldehyde). Enzyme load: 1 µg on 0.5 µL beads; Flow rate 24 µL/h. For detailed reaction parameters please refer to Table 7.**

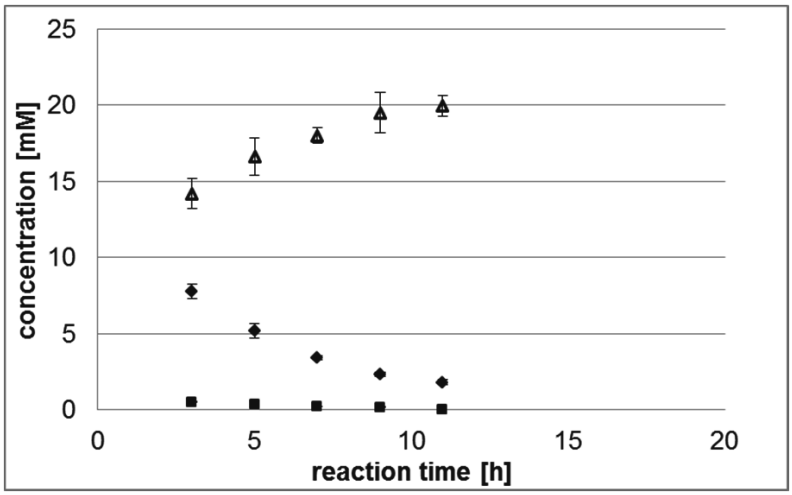


**Figure 60: Reaction data for the µMORE at pH 7.5; 200 mM acetaldehyde; 25 mM benzaldehyde 20°C (◆ (*S*)-HPP; ■ (*R*)-HPP ▲ benzaldehyde). Enzyme load: 1 µg on 0.5 µL beads; Flow rate 24 µL/h. For detailed reaction parameters please refer to Table 7.**

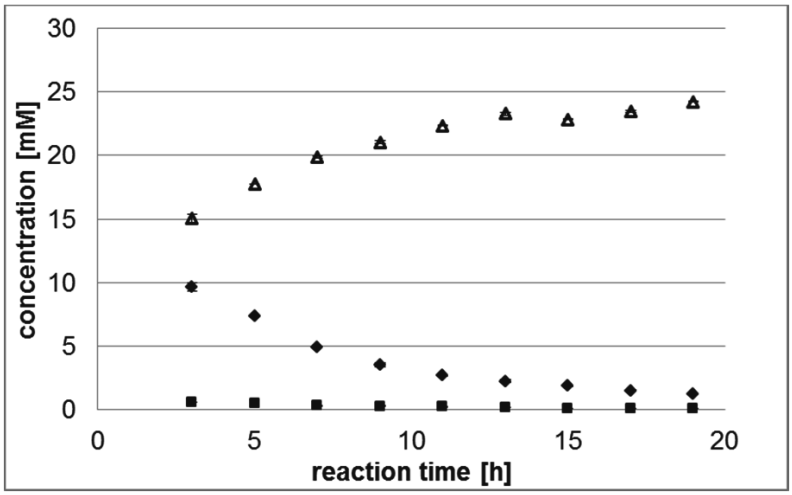


**Figure 61: Reaction data for the µMORE at pH 7.5; 250 mM acetaldehyde; 25 mM benzaldehyde 20°C (◆ (*S*)-HPP; ■ (*R*)-HPP ▲ benzaldehyde). Enzyme load: 1 µg on 0.5 µL beads; Flow rate 24 µL/h. For detailed reaction parameters please refer to Table 7.**

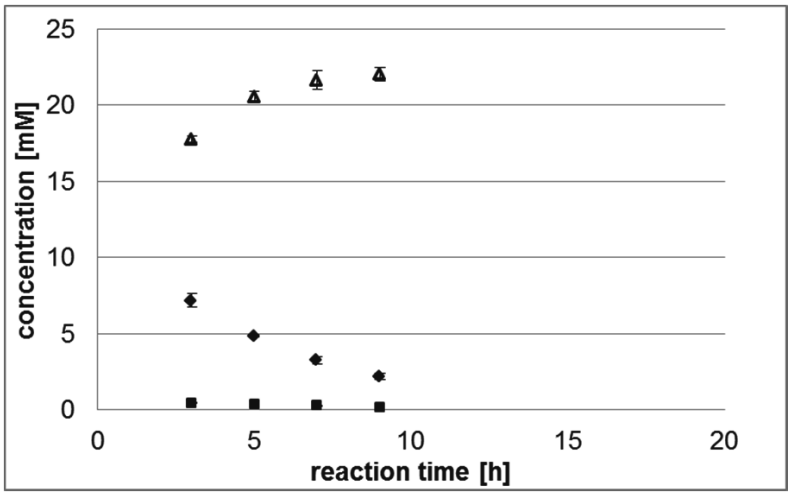


**Figure 62: Reaction data for the µMORE at pH 7.5; 300 mM acetaldehyde; 25 mM benzaldehyde 20°C (◆ (*S*)-HPP; ■ (*R*)-HPP ▲ benzaldehyde). Enzyme load: 1 µg on 0.5 µL beads; Flow rate 24 µL/h. For detailed reaction parameters please refer to Table 7.**

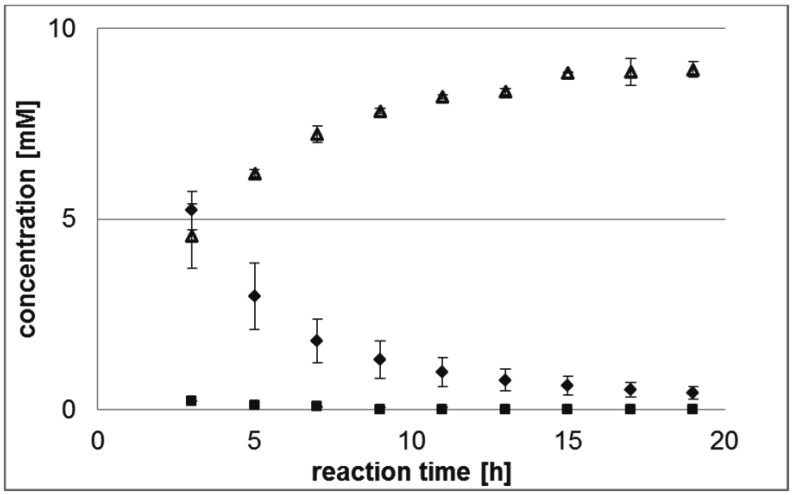


**Figure 63: Reaction data for the µMORE at pH 7.5; 200 mM acetaldehyde; 10 mM benzaldehyde 20°C (◆ (*S*)-HPP; ■ (*R*)-HPP ▲ benzaldehyde). Enzyme load: 1 µg on 0.5 µL beads; Flow rate 24 µL/h. For detailed reaction parameters please refer to Table 7.**

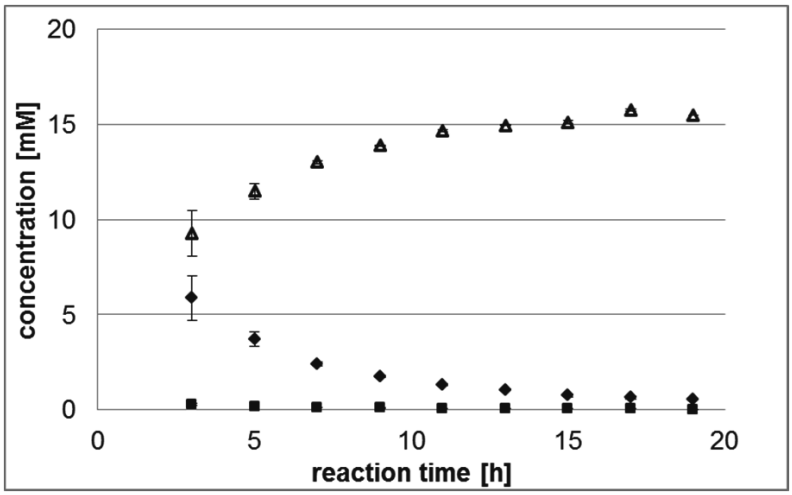


**Figure 64: Reaction data for the µMORE at pH 7.5; 200 mM acetaldehyde; 15 mM benzaldehyde 20°C (◆ (*S*)-HPP; ■ (*R*)-HPP ▲ benzaldehyde). Enzyme load: 1 µg on 0.5 µL beads; Flow rate 24 µL/h. For detailed reaction parameters please refer to Table 7.**

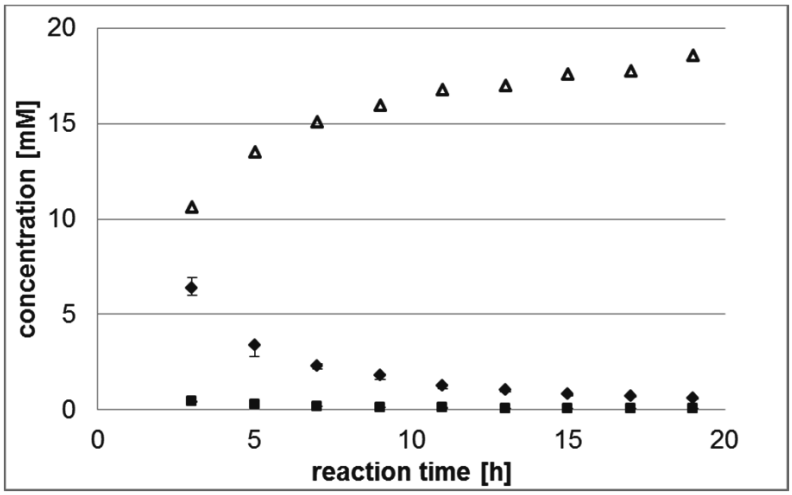


**Figure 65: Reaction data for the µMORE at pH 7.5; 200 mM acetaldehyde; 20 mM benzaldehyde 20°C (◆ (*S*)-HPP; ■ (*R*)-HPP ▲ benzaldehyde). Enzyme load: 1 µg on 0.5 µL beads; Flow rate 24 µL/h. For detailed reaction parameters please refer to Table 7.**

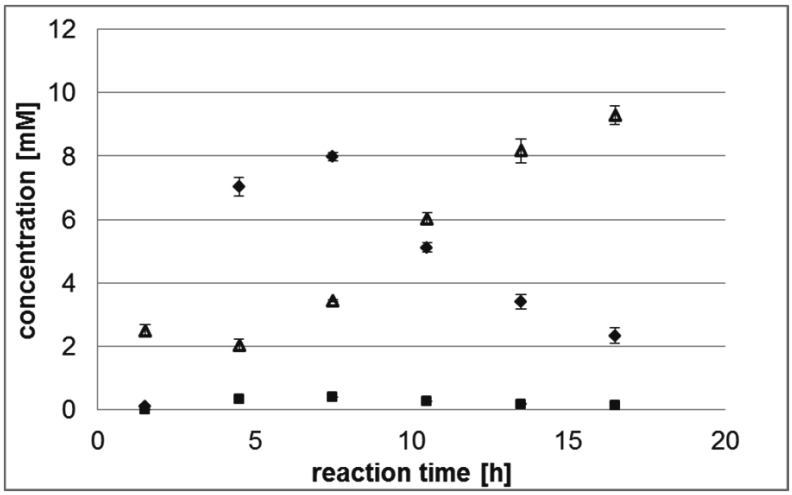


**Figure 66: Reaction data for the µMORE at pH 7.5; 200 mM acetaldehyde; 10 mM benzaldehyde 20°C (◆ (*S*)-HPP; ■ (*R*)-HPP ▲ benzaldehyde). Enzyme load: 1 µg on 0.5 µL beads; Flow rate 8 µL/h. For detailed reaction parameters please refer to Table 7.**

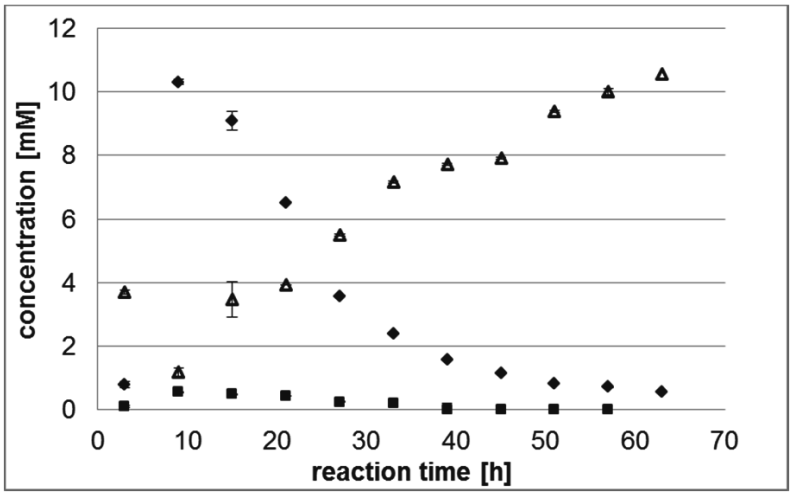


**Figure 67: Reaction data for the µMORE at pH 7.5; 200 mM acetaldehyde; 10 mM benzaldehyde 20°C (◆ (*S*)-HPP; ■ (*R*)-HPP ▲ benzaldehyde). Enzyme load: 1 µg on 0.5 µL beads; Flow rate 4 µL/h. For detailed reaction parameters please refer to Table 7.**

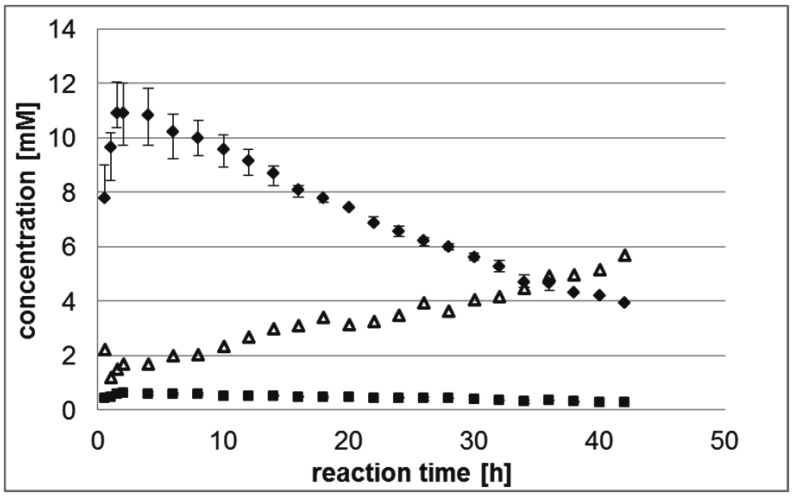


**Figure 68: Reaction data for the EMR at pH 7.5; 200 mM acetaldehyde; 10 mM benzaldehyde 20°C (◆ (*S*)-HPP; ■ (*R*)-HPP △ benzaldehyde). Enzyme load: 10 mg; Flow rate 40 mL/h. For detailed reaction parameters please refer to Table 7.**

## 7.3 Construction drawings

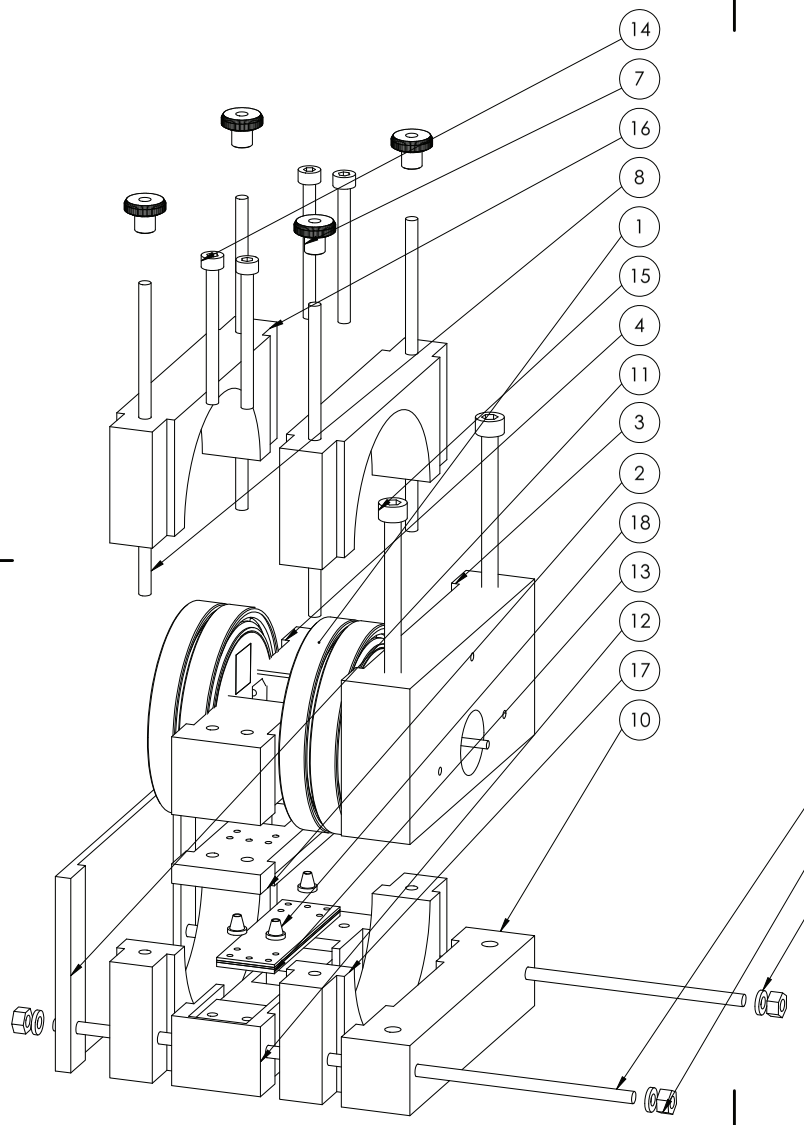


| POS-NR. | NAME | DESCRIPTION | QUANTITY |
|---|---|---|---|
| 1 | axle with magnet mountings | brass, please refer to magnet mounting assembly | 1 |
| 2 | chipholder lid | ABS | 1 |
| 3 | motor mounting | aluminum | 1 |
| 4 | spacer | ABS | 2 |
| 5 | M3 threaded bolt | stainless steel | 2 |
| 6 | M3 nut | stainless steel | 4 |
| 7 | M3 thumbscrew | steel nickel-plated | 4 |
| 8 | m3 threaded bolt | stainless steel | 4 |
| 9 | washer | stainless steel | 4 |
| 10 | chipholder mainframe part 1 | aluminum | 1 |
| 11 | chipholder mainframe part 2 | aluminum | 1 |
| 12 | chipholder mainframe part 3 | aluminum | 1 |
| 13 | microfluidic chip | micronit custom build | 1 |
| 14 | M3X35 screw | stainless steel | 4 |
| 15 | M4X50 screw | stainless steel | 2 |
| 16 | upper bearing mounting | brass | 2 |
| 17 | lower bearing mounting | brass | 2 |
| 18 | mircornit pro ferrule | FFKM | 3 |

Werkstoff:

| | | | | |
|---|---|---|---|---|
| responsible department<br>biocat | technical reference | created by | approved by | 1:1 |
| | | document type | document status<br>FINAL | |
| | | title, additional title<br>µMORE prototype assembly | | |
| | | | date | lan.<br>ENG |
| | | | | sheet<br>/ |

Toleranzen ISO 8015 | Werkstückkanten nach DIN ISO 13715
Allgemeintoleranz DIN 2768-mH | Angaben zu Oberflächenbeschaffenheit nach DIN EN ISO 1302
Allgemeintol. DIN EN ISO 13920-AR

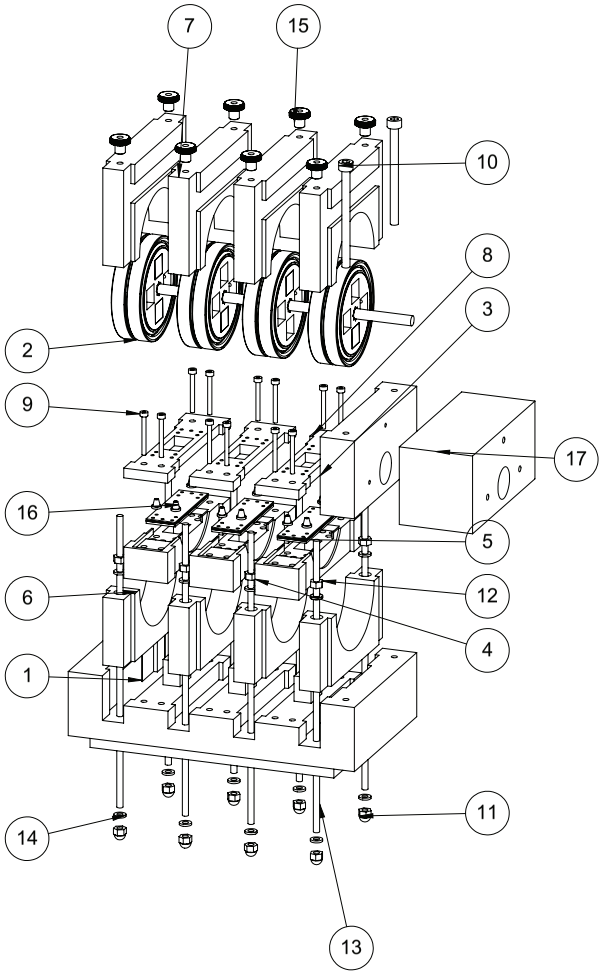


| POS-NR. | NAME | DESCRIPTION | QUANTITY |
|---|---|---|---|
| 1 | reactor mainframe | aluminum | 1 |
| 2 | axle with magnet mountings | please refer to "magnetic mounting assembly" | 1 |
| 3 | motor mounting | ABS | 1 |
| 4 | bottom chipholder | aluminum | 3 |
| 5 | microfluidic chip | micronit custom build | 3 |
| 6 | bottom bearing mounting | brass | 4 |
| 7 | top bearing mounting | brass | 4 |
| 8 | chipholder lid | aluminum | 3 |
| 9 | screw M1x20 | stainless steel | 12 |
| 10 | screw M4X50 | stainless steel | 2 |
| 11 | domed nut M3 | brass | 8 |
| 12 | nut M3 | stainless steel | 8 |
| 13 | threaded bolt M3 | stainless steel | 8 |
| 14 | washer M3 | stainless steel | 17 |
| 15 | thumbscrew M3 | steel nickel-plated | 8 |
| 16 | mircronit pro ferrule | FFKM | 9 |
| 17 | motor adapter | ABS | 1 |

toleration ISO 8015
general tolerance DIN 2768-mH
general tol. DIN EN ISO 13920-AF
workpiece edges according to DIN ISO 13715
information on surface texture according to DIN EN ISO 1302

| responsible department | technical reference | created by | approved by | |
|---|---|---|---|---|
| biocat | | | | |
| | | document type | document status | |
| | | | FINAL | |
| | | title, additional title | | |
| | | µMORE assembly | | |
| | | | date | lan. ENG / sheet / |

| POS-NR. | NAME | DESCRIPTION | QUANTITY |
|---|---|---|---|
| 1 | magnet mounting | brass | 1 |
| 2 | magnet | NdFeB N50 (ChenYang Technologies GmbH & Co. KG) | 1 |
| 3 | bearing 61808 | plastic with glass balls (Haku GmbH) | 2 |
| 4 | slug m2 | stainless steel | 2 |

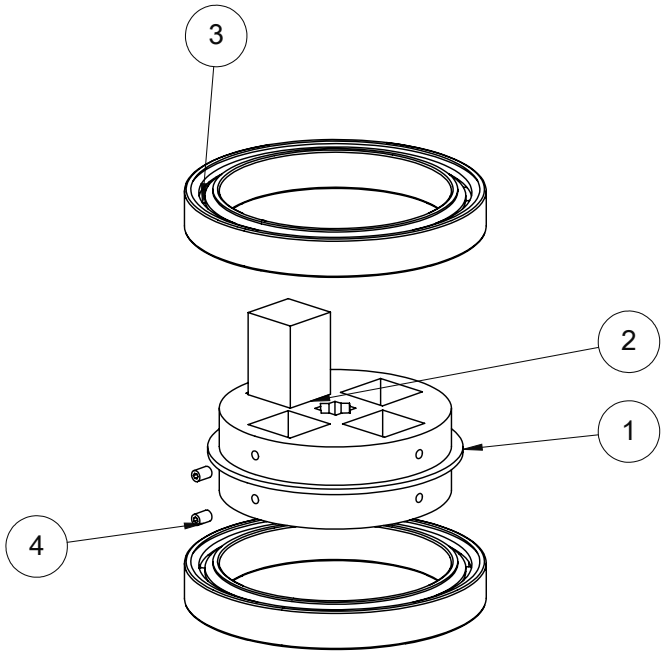


| resposible department | technical reference | created by | approved by | scale |
|---|---|---|---|---|
| biokat | | Daniel Jussen | | 1:1 |

| document type | document status |
|---|---|
| | FINAL |

title additional title: magnet mounting

| date | date | lan. | sheet |
|---|---|---|---|
| | | ENG | / |

workpiece edges according to DIN ISO 13715

information on surface texture according to DIN EN ISO 1302

toleration ISO 8015

general tolerance DIN 2768-mH
general tol. DIN EN ISO 13920-AF

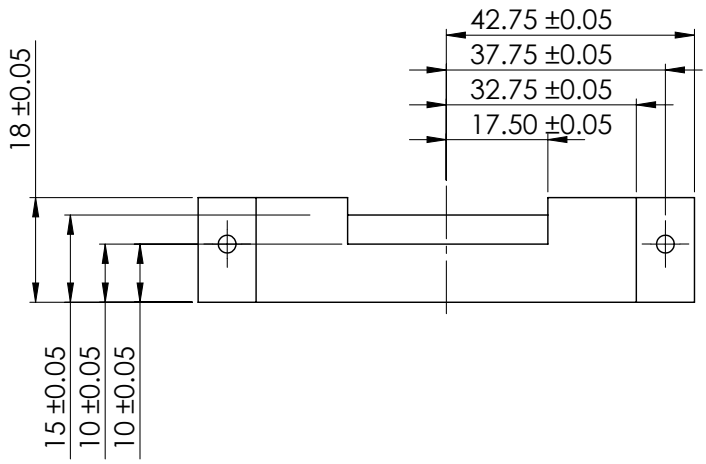


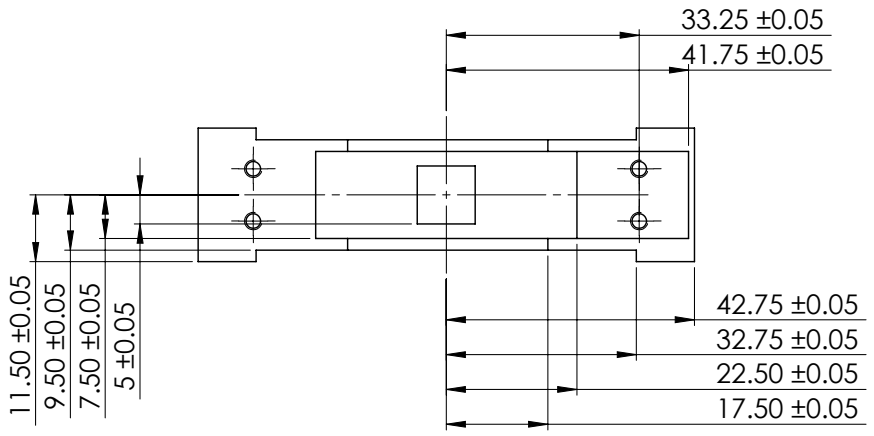


| | | | | |
|---|---|---|---|---|
| resposible department: biokat | technical reference: | created by: Daniel Jussen | approved by: | scale: |
| | | document type: | document status: FINAL | |
| | | title additional title: reactor mainfram part 1 | | |
| | | | date: | lan.: ENG / sheet: / |

toleration ISO 8015

general tolerance DIN 2768-mH
general tol. DIN EN ISO 13920-AF

information on surface texture
according to DIN EN ISO 1302

workpiece edges according to DIN ISO 13715

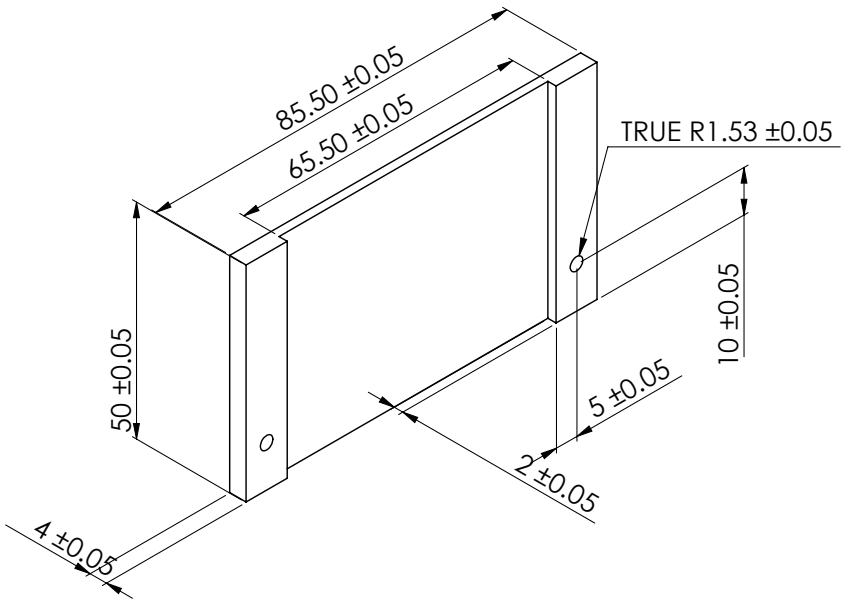


| | | | | |
|---|---|---|---|---|
| resposible department: biokat | technical reference: | created by: Daniel Jussen | approved by: | scale: |
| | | document type: | | document status: FINAL |
| | | title additional title: reactor mainframe part 2 | | |
| | | | date: | lan.: ENG / sheet: / |

workpiece edges according to DIN ISO 13715

information on surface texture according to DIN EN ISO 1302

toleration ISO 8015

general tolerance DIN 2768-mH
general tol. DIN EN ISO 13920-AF

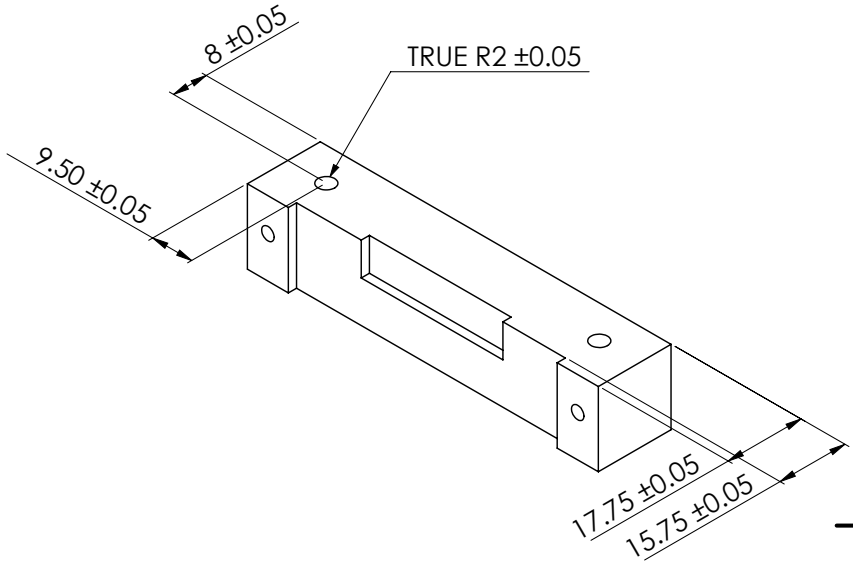


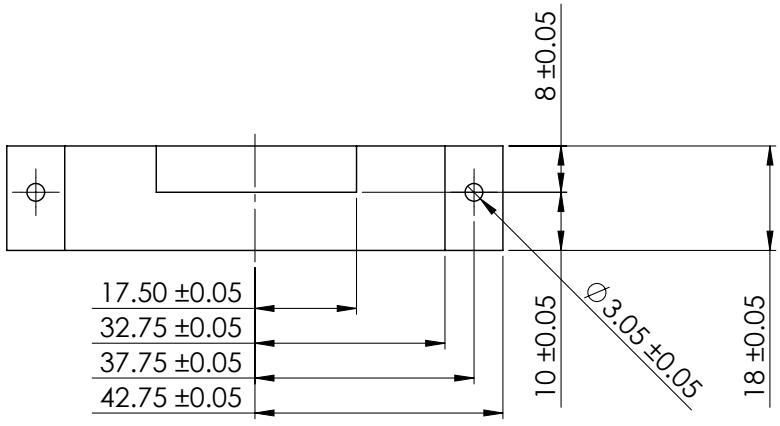


| | | | | |
|---|---|---|---|---|
| resposible department: biokat | technical reference: | created by: Daniel Jussen | approved by: | scale: |
| | | document type: | | document status: FINAL |
| | | title additional title: reactor mainframe part 3 | | date: / lan.: ENG / sheet: / |

toleration ISO 8015
general tolerance DIN 2768-mH
general tol. DIN EN ISO 13920-AF
workpiece edges according to DIN ISO 13715
information on surface texture according to DIN EN ISO 1302

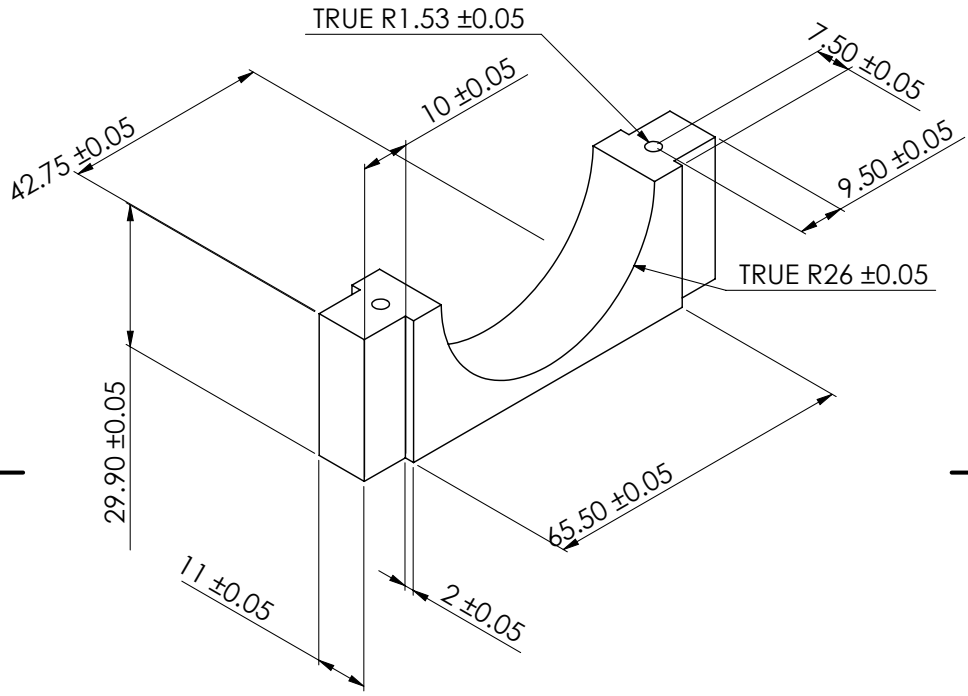


| | | | | |
|---|---|---|---|---|
| resposible department: biokat | technical reference: | created by: Daniel Jussen | approved by: | scale: |
| | | document type: | document status: FINAL | |
| | | title additional title: lower bearing mounting | date: | lan.: ENG / sheet: / |

workpiece edges according to DIN ISO 13715

information on surface texture according to DIN EN ISO 1302

toleration ISO 8015

general tolerance DIN 2768-mH
general tol. DIN EN ISO 13920-AF

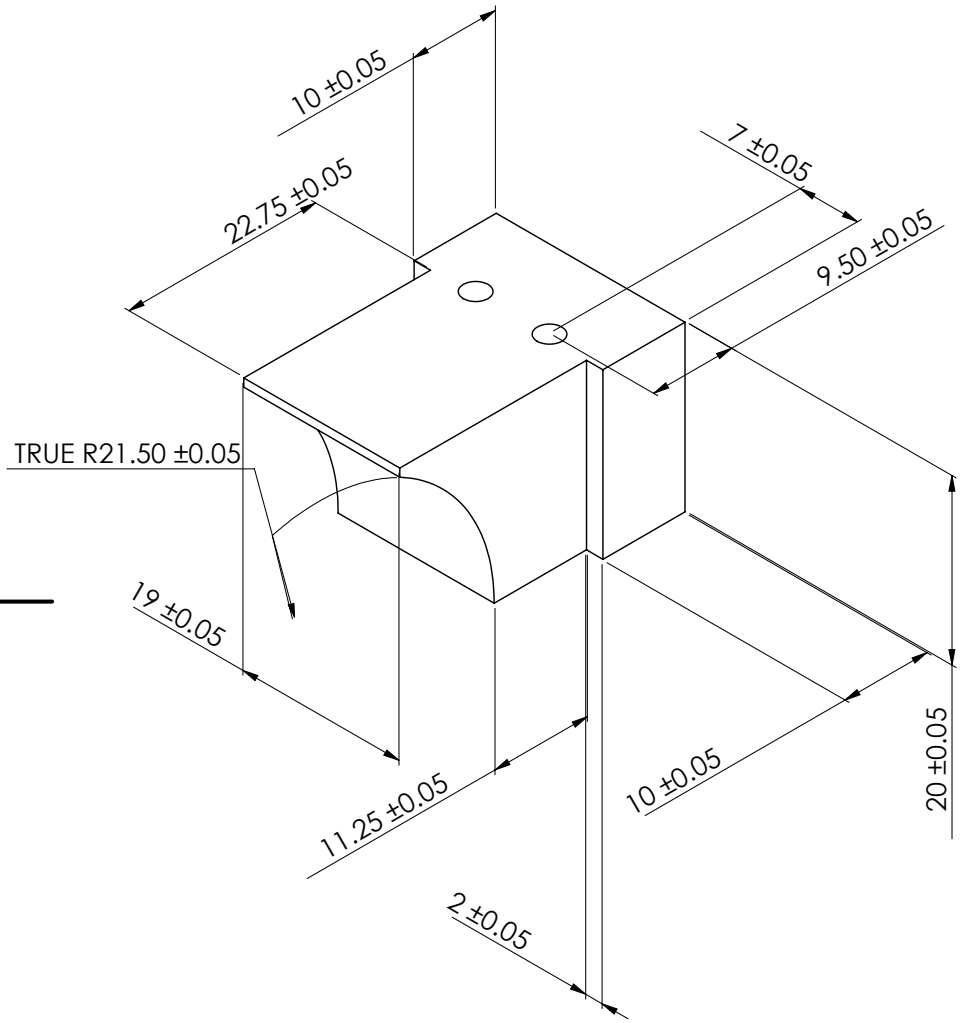


| | | | | |
|---|---|---|---|---|
| resposible department: biokat | technical reference: | created by: Daniel Jussen | approved by: | scale: |
| | | document type: | document status: FINAL | |
| | | title additional title: chipholder lid spacer | | |
| | | | date: | lan.: ENG / sheet: / |

workpiece edges according to DIN ISO 13715

information on surface texture according to DIN EN ISO 1302

toleration ISO 8015

general tolerance DIN 2768-mH
general tol. DIN EN ISO 13920-AF

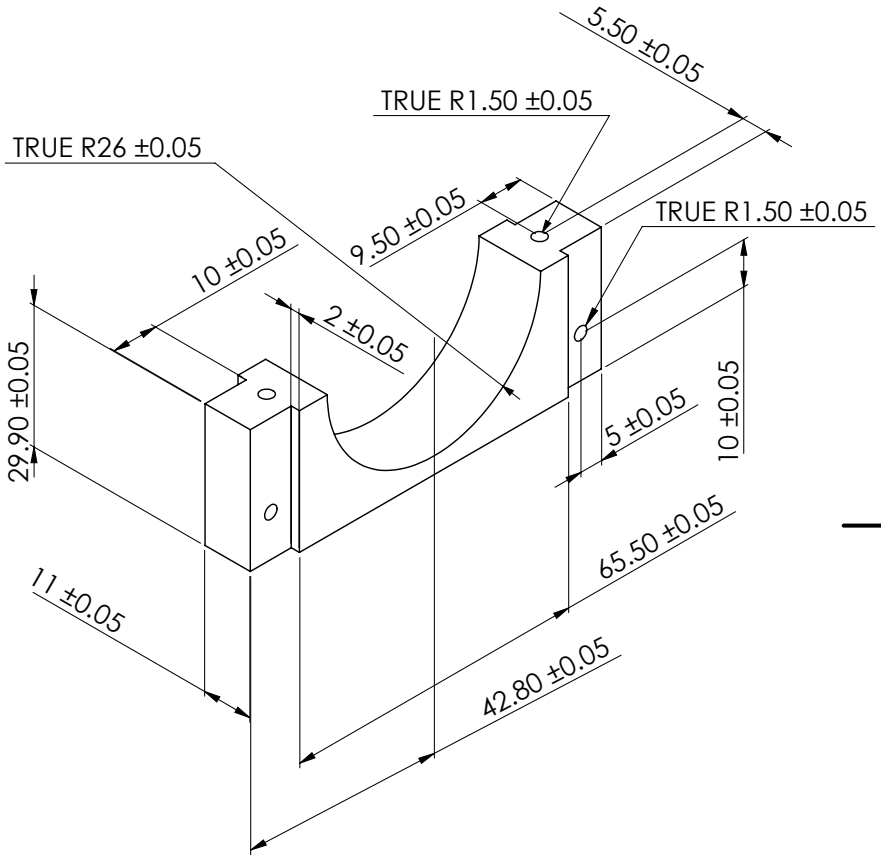


| | | | | |
|---|---|---|---|---|
| resposible department: biokat | technical reference: | created by: Daniel Jussen | approved by: | scale: |
| | | document type: | document status: FINAL | |
| | | title additional title: upper bearing mounting | date: | lan.: ENG / sheet: / |

workpiece edges according to DIN ISO 13715

information on surface texture according to DIN EN ISO 1302

toleration ISO 8015

general tolerance DIN 2768-mH
general tol. DIN EN ISO 13920-AF

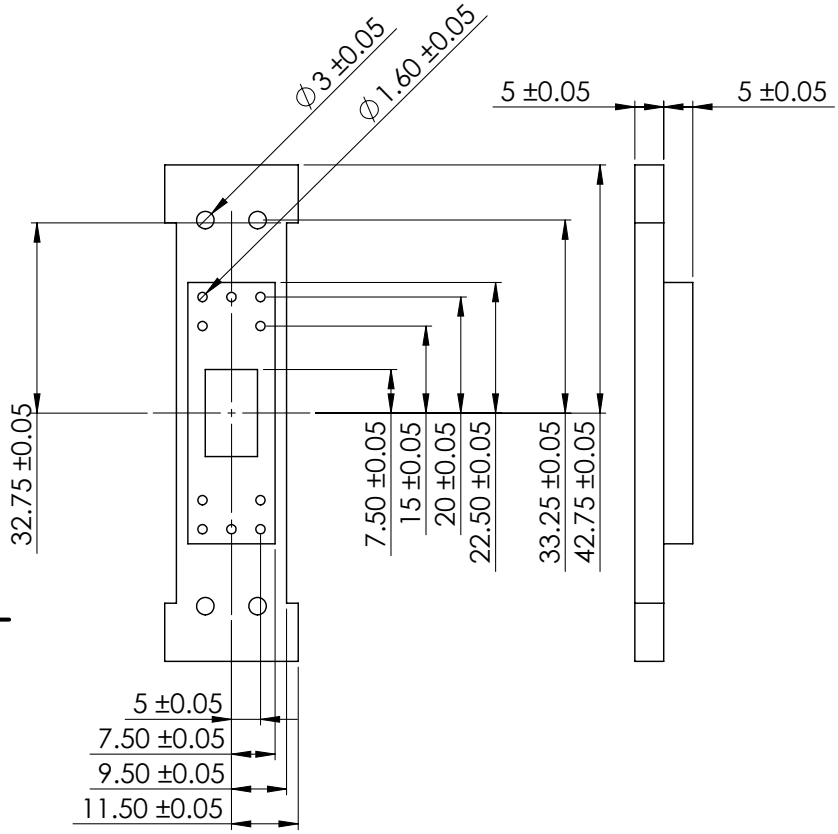


| | | | | |
|---|---|---|---|---|
| resposible department: biokat | technical reference: | created by: Daniel Jussen | approved by: | scale: |
| | | document type: | document status: FINAL | |
| | | title additional title: chipholder lid | date: | lan.: ENG / sheet: |

workpiece edges according to DIN ISO 13715

information on surface texture according to DIN EN ISO 1302

toleration ISO 8015

general tolerance DIN 2768-mH
general tol. DIN EN ISO 13920-AF

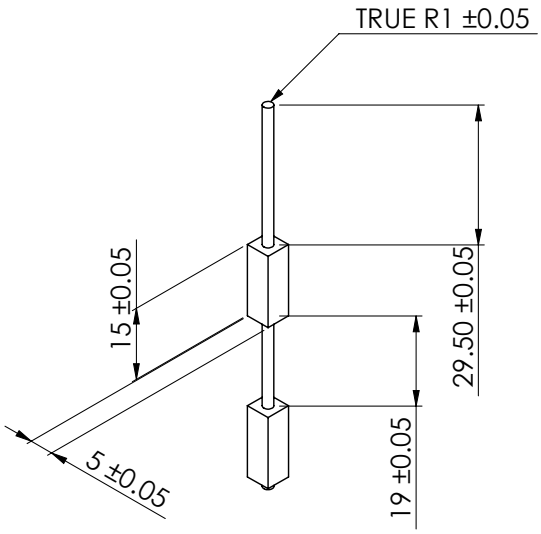


| | | | | |
|---|---|---|---|---|
| resposible department: biokat | technical reference: | created by: Daniel Jussen | approved by: | scale: |
| | | document type: | document status: FINAL | |
| | | title additional title: axle | | |
| | | | date: | lan.: ENG / sheet: / |

workpiece edges according to DIN ISO 13715

information on surface texture according to DIN EN ISO 1302

toleration ISO 8015

general tolerance DIN 2768-mH
general tol. DIN EN ISO 13920-AF

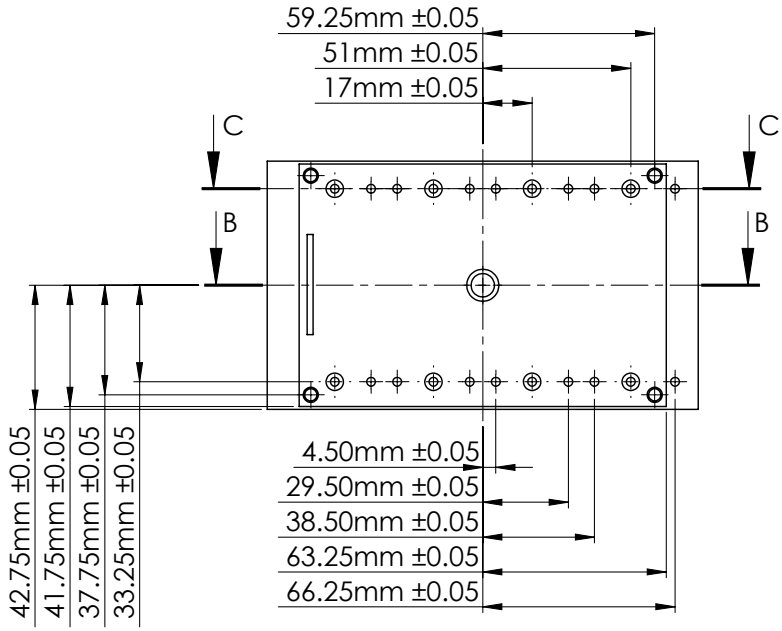


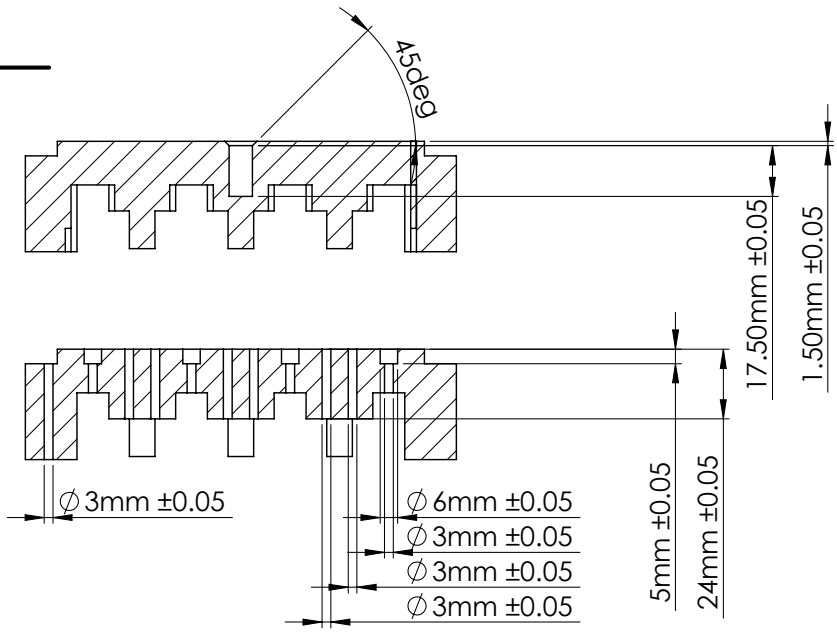


| | | | | |
|---|---|---|---|---|
| resposible department: biokat | technical reference: | created by: Daniel Jussen | approved by: | scale: 1:1 |
| | | document type: | | document status: FINAL |
| | | title additional title: reactor mainframe | | |
| | | | date | lan.: ENG / sheet: / |

workpiece edges according to DIN ISO 13715

information on surface texture according to DIN EN ISO 1302

toleration ISO 8015

general tolerance DIN 2768-mH
general tol. DIN EN ISO 13920-AF

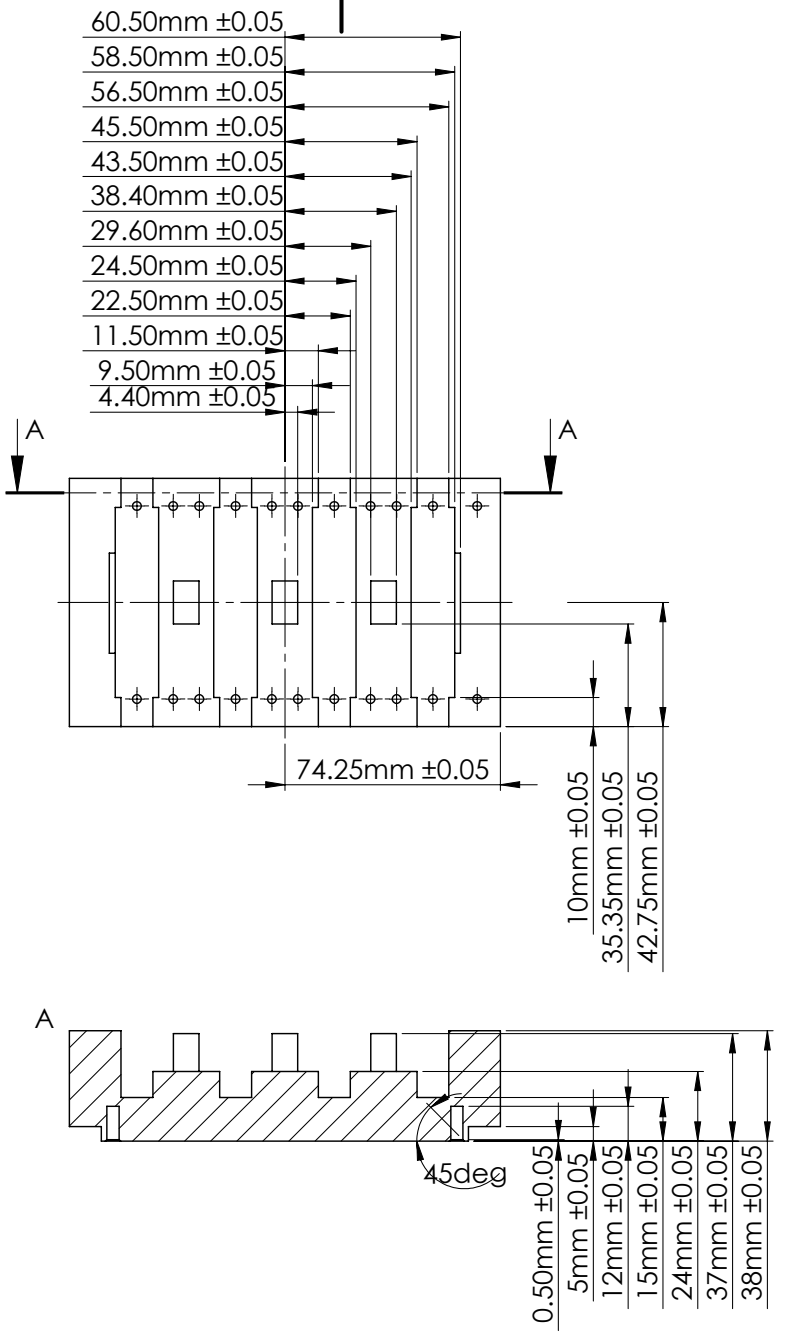


| | | | | |
|---|---|---|---|---|
| resposible department: biokat | technical reference | created by: Daniel Jussen | approved by | scale: 1:1 |
| | | document type | | document status: FINAL |
| | | title additional title: reactor mainframe | | |
| | | | date | lan.: ENG / sheet |

workpiece edges according to DIN ISO 13715

information on surface texture according to DIN EN ISO 1302

toleration ISO 8015

general tolerance DIN 2768-mH
general tol. DIN EN ISO 13920-AF

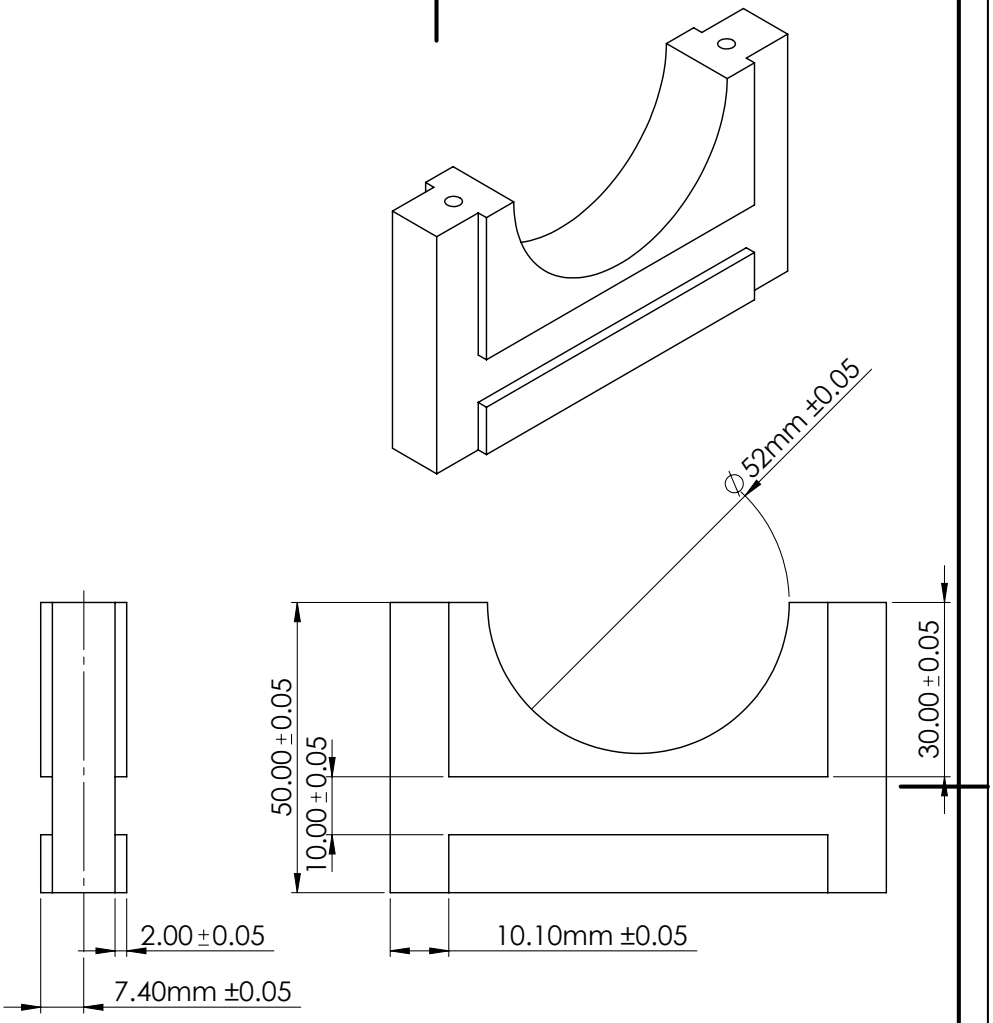


| | | | | |
|---|---|---|---|---|
| resposible department: microscale | technical reference: | created by: Daniel Jussen | approved by: | scale: 1:1 |
| | | document type: | | document status: FINAL |
| | | title additional title: top bearing mounting | | top bearing mounting |
| | | | date: | lan.: ENG / sheet: / |

workpiece edges according to DIN ISO 13715

information on surface texture according to DIN EN ISO 1302

toleration ISO 8015

general tolerance DIN 2768-mH
general tol. DIN EN ISO 13920-AF

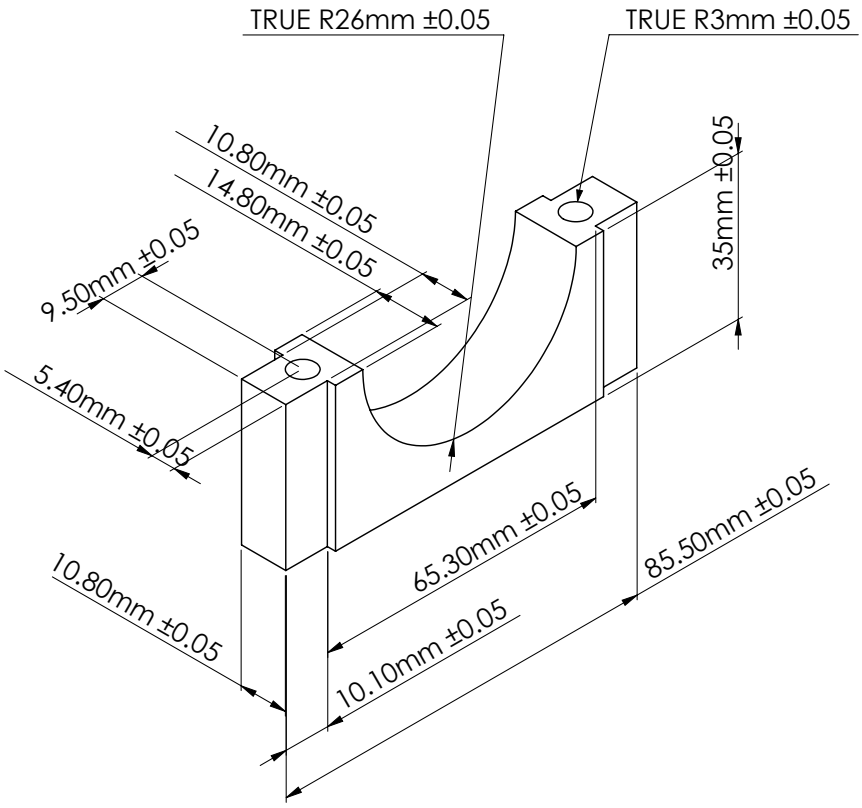


| | | | | |
|---|---|---|---|---|
| resposible department: microscale | technical reference: | created by: Daniel Jussen | approved by: | scale: 1:1 |
| | | document type: | | document status: FINAL |
| | | title additional title: bottom bearing mounting | | |
| | | | date: | lan.: ENG / sheet: / |

workpiece edges according to DIN ISO 13715

information on surface texture according to DIN EN ISO 1302

toleration ISO 8015

general tolerance DIN 2768-mH
general tol. DIN EN ISO 13920-AF

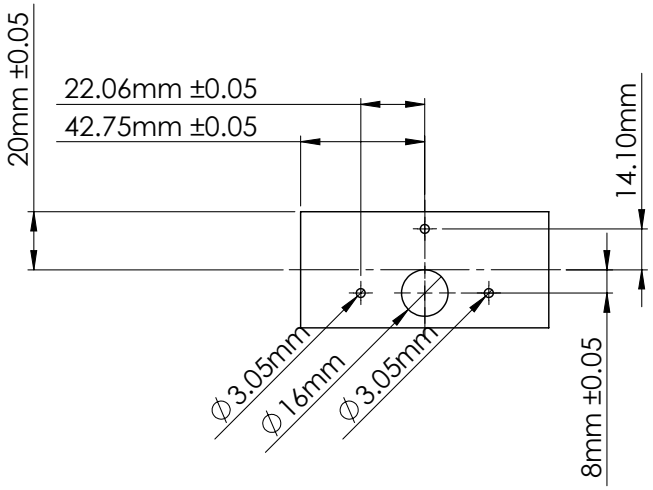


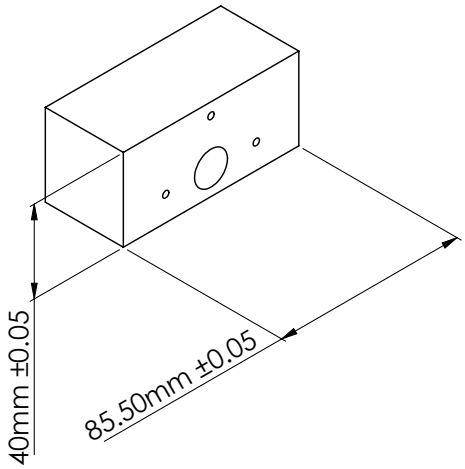


| | | | | |
|---|---|---|---|---|
| resposible department: microscale | technical reference: | created by: Daniel Jussen | approved by: | scale: 1:1 |
| | | document type: | | document status: FINAL |
| | | title additional title: motor spacer | | |
| | | | date: | lan.: ENG / sheet: / |

toleration ISO 8015
general tolerance DIN 2768-mH
general tol. DIN EN ISO 13920-AF
workpiece edges according to DIN ISO 13715
information on surface texture
according to DIN EN ISO 1302

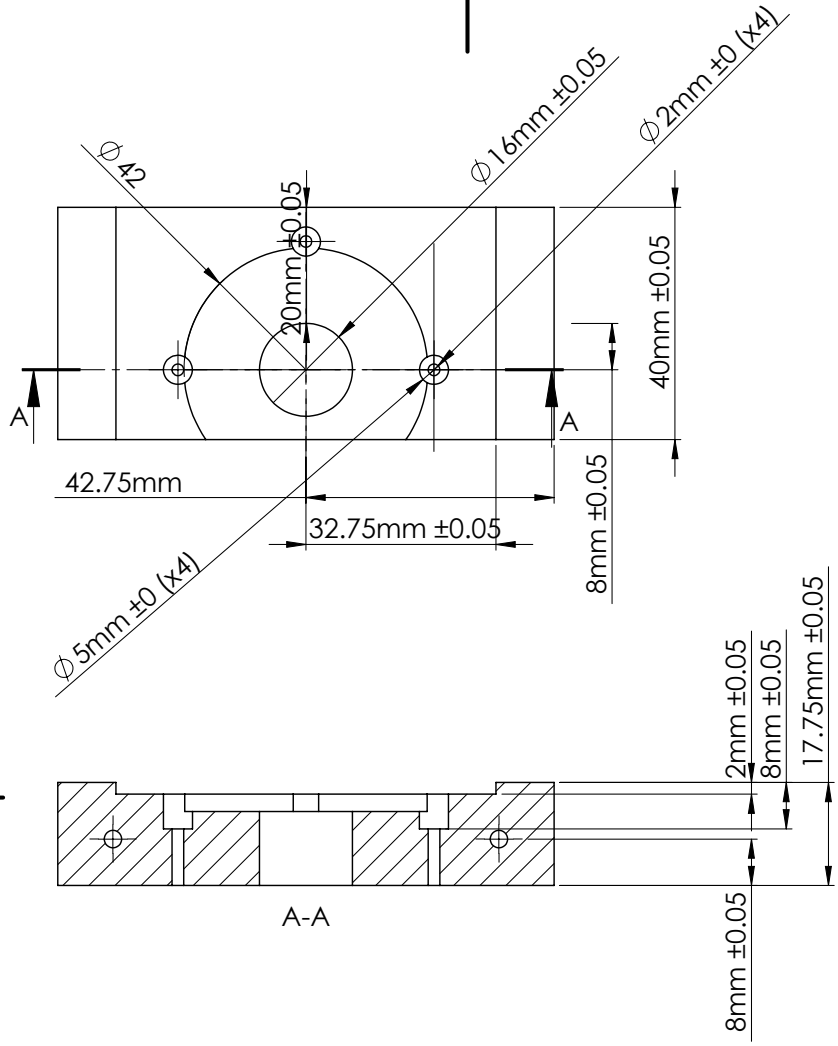


| | | | | |
|---|---|---|---|---|
| resposible department: microscale | technical reference: | created by: Daniel Jussen | approved by: | scale: 1:1 |
| | | document type: | document status: FINAL | |
| | | title additional title: motor mounting | | |
| | | | date: | lan.: ENG / sheet: / |

workpiece edges according to DIN ISO 13715
information on surface texture according to DIN EN ISO 1302
toleration ISO 8015
general tolerance DIN 2768-mH
general tol. DIN EN ISO 13920-AF

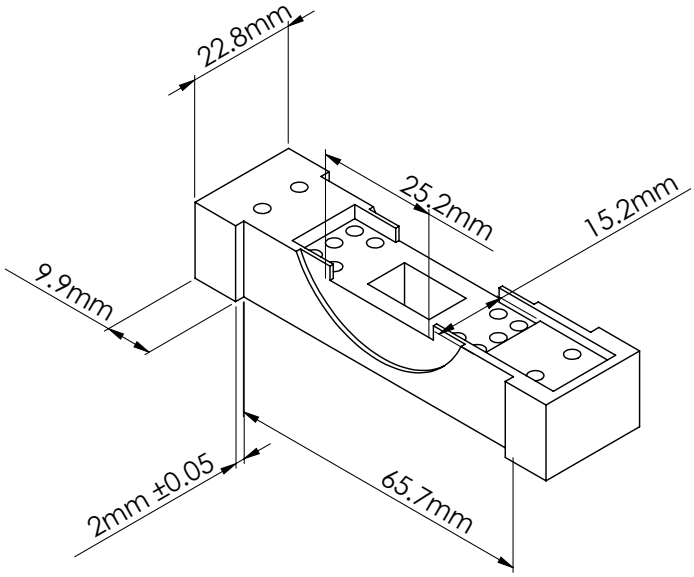


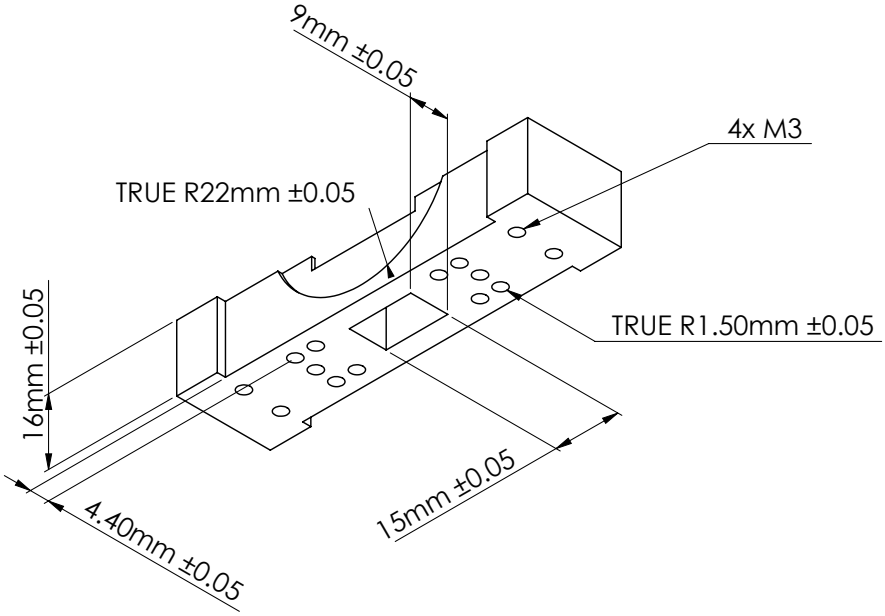


| | | | | |
|---|---|---|---|---|
| resposible department: microscale | technical reference: | created by: Daniel Jussen | approved by: | scale: 1:1 |
| | | document type: | | document status: FINAL |
| | | title additional title: chip holder bottom | | |
| | | | date: | lan.: ENG / sheet: / |

workpiece edges according to DIN ISO 13715

information on surface texture according to DIN EN ISO 1302

toleration ISO 8015

general tolerance DIN 2768-mH
general tol. DIN EN ISO 13920-AF

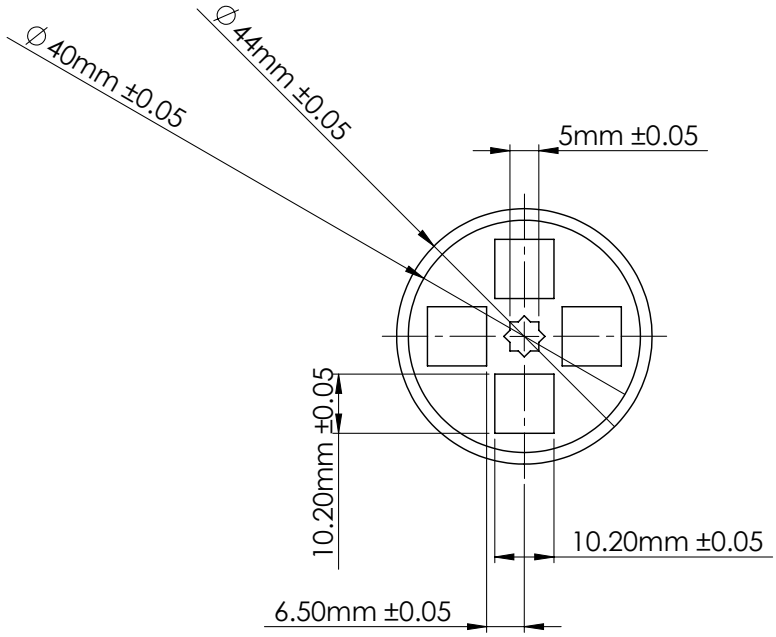


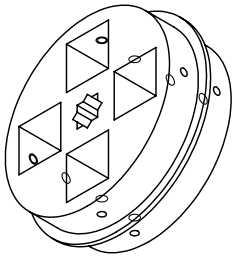

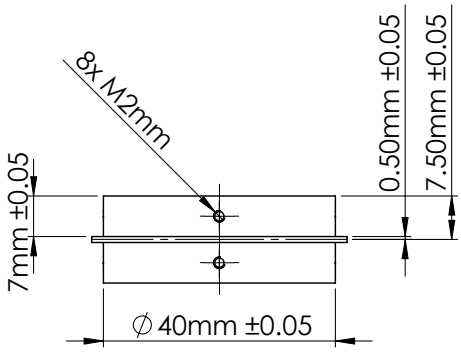


| | | | | |
|---|---|---|---|---|
| resposible department: microscale | technical reference: | created by: Daniel Jussen | approved by: | scale: 1:1 |
| | | document type: | | document status: FINAL |
| | | title additional title: magnet mounting | | |
| | | | date: | lan.: ENG / sheet: / |

toleration ISO 8015
general tolerance DIN 2768-mH
general tol. DIN EN ISO 13920-AF
workpiece edges according to DIN ISO 13715
information on surface texture according to DIN EN ISO 1302

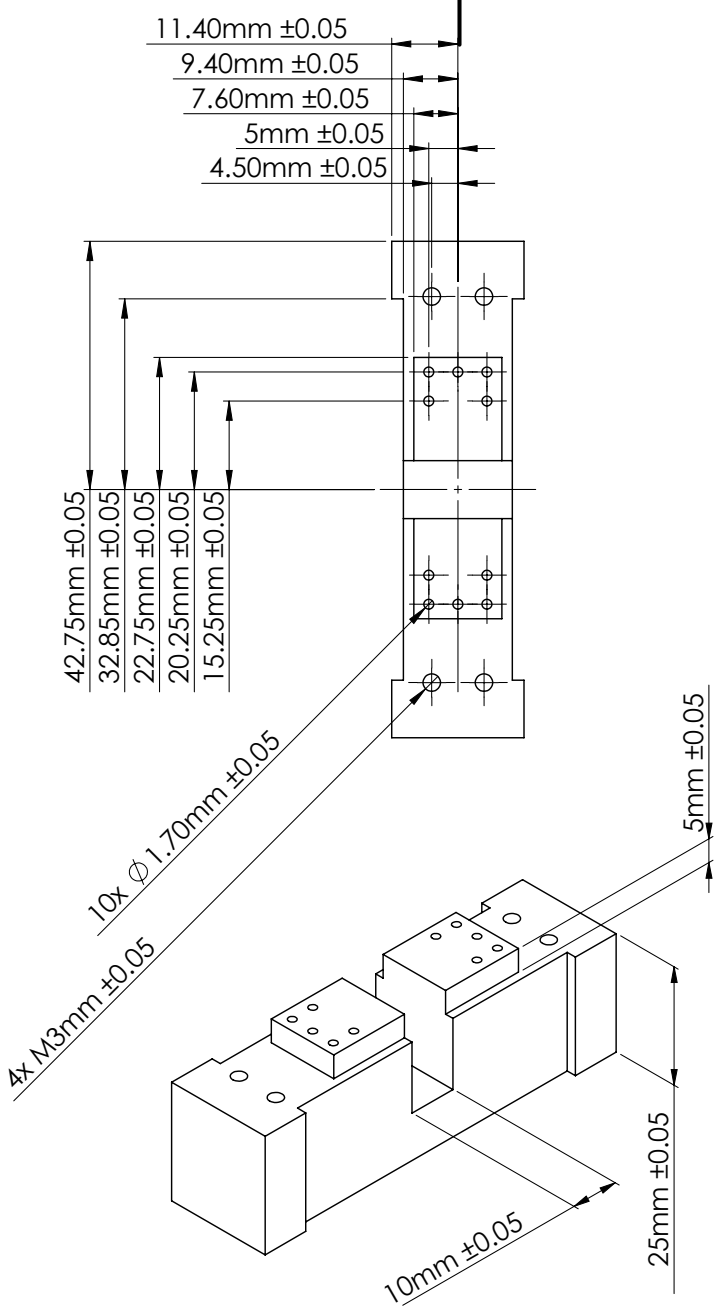


| | | | | |
|---|---|---|---|---|
| resposible department: biokat | technical reference: | created by: Daniel Jussen | approved by: | scale: 1:1 |
| | | document type: | | document status: FINAL |
| | | title additional title: chipholder lid prototype 1 | | |
| | | | date: | lan.: ENG / sheet: / |

toleration ISO 8015

general tolerance DIN 2768-mH
general tol. DIN EN ISO 13920-AF

workpiece edges according to DIN ISO 13715

information on surface texture
according to DIN EN ISO 1302

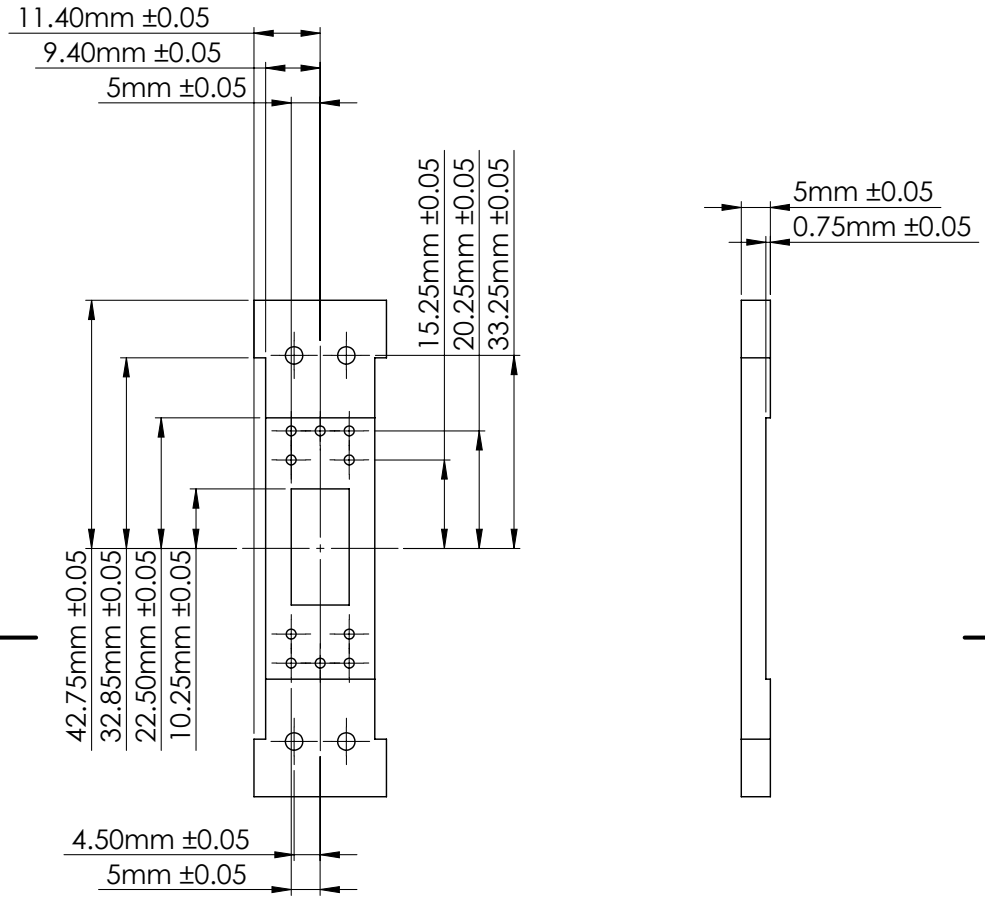


| | | | | |
|---|---|---|---|---|
| resposible department: microscale | technical reference: | created by: Daniel Jussen | approved by: | scale: 1:1 |
| | | document type: | document status: FINAL | |
| | | title additional title: chipholder lid prototype 2 | | |
| | | | date: | lan.: ENG / sheet: / |

workpiece edges according to DIN ISO 13715

information on surface texture according to DIN EN ISO 1302

toleration ISO 8015

general tolerance DIN 2768-mH
general tol. DIN EN ISO 13920-AF

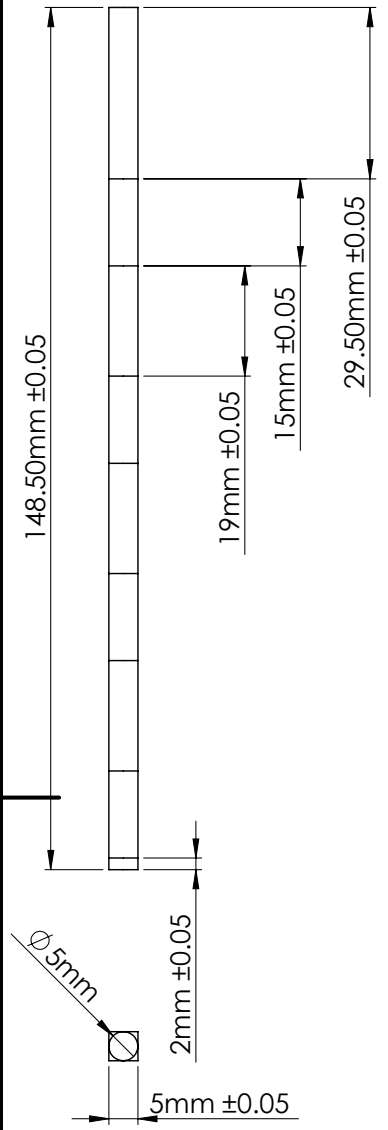


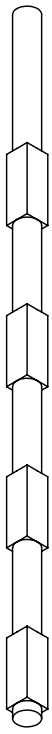

| | | | | |
|---|---|---|---|---|
| resposible department: biokat | technical reference: | created by: Daniel Jussen | approved by: | scale: 1:1 |
| | | document type: | document status: FINAL | |
| | | title additional title: axle | | |
| | | | date: | lan.: ENG / sheet: / |

toleration ISO 8015
general tolerance DIN 2768-mH
general tol. DIN EN ISO 13920-AF
workpiece edges according to DIN ISO 13715
information on surface texture according to DIN EN ISO 1302

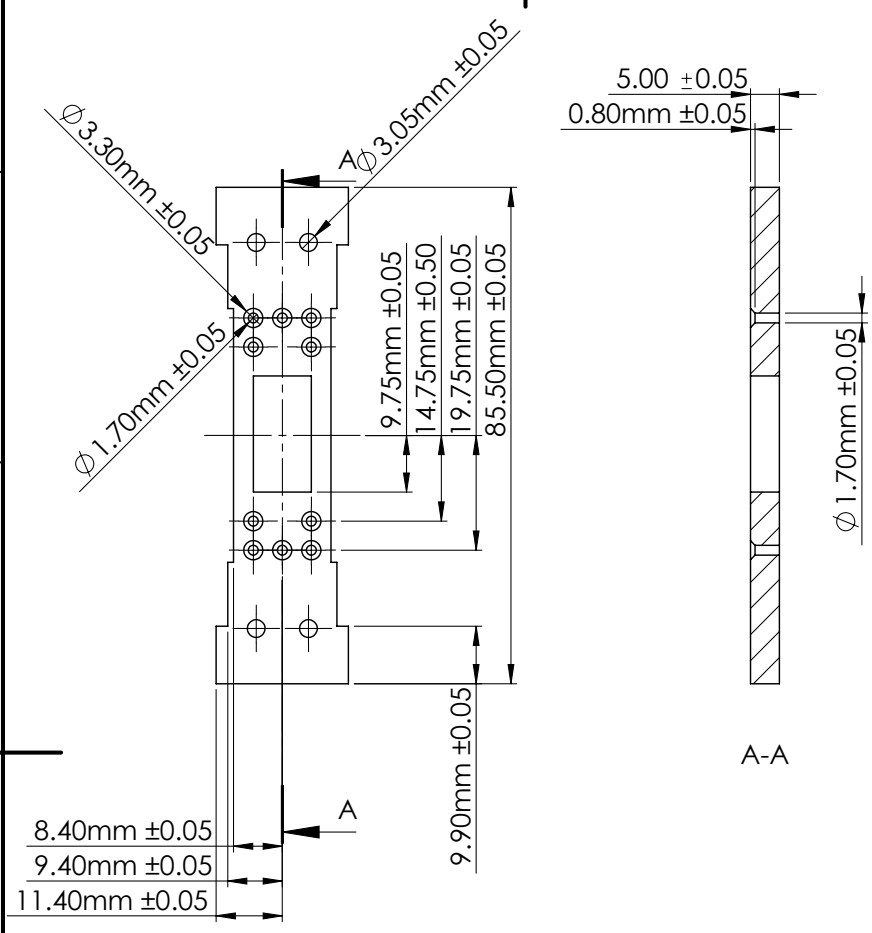


| | | | | |
|---|---|---|---|---|
| resposible department: biokat | technical reference: | created by: Daniel Jussen | approved by: | scale: 1:1 |
| | | document type: | | document status: FINAL |
| | | title additional title: chipholder lid | | |
| | | | date: | lan.: ENG / sheet: / |

workpiece edges according to DIN ISO 13715

information on surface texture according to DIN EN ISO 1302

toleration ISO 8015

general tolerance DIN 2768-mH
general tol. DIN EN ISO 13920-AF

Band / Volume 73
**Stereoselective synthesis of vicinal diols with enzymatic cascade reactions**
J. Kulig (2013), XV, 177 pp
ISBN: 978-3-89336-911-9

Band / Volume 74
**Computing Solids**
**Models, ab-initio methods and supercomputing**
Lecture Notes of the 45th IFF Spring School 2014
March 10 – 21, 2014 Jülich, Germany
ed. by S. Blügel, N. Helbig, V. Meden, D. Wortmann (2014), ca. 1000 pp
ISBN: 978-3-89336-912-6

Band / Volume 75
**Aberrationskorrigierte Photoemissionsmikroskopie an magnetischen Systemen: Von statischer Charakterisierung zu zeitaufgelöster Abbildung**
F. Nickel (2013), x, 99 pp
ISBN: 978-3-89336-913-3

Band / Volume 76
**Temperature-Induced Metamagnetic Transition and Domain Structures of Single-Crystalline FeRh Thin Films on MgO(100)**
X. Zhou (2013), xi, 104 pp
ISBN: 978-3-89336-919-5

Band / Volume 77
**Interplay between Magnetism and Superconductivity in Iron Based High Temperature Superconductors**
S. Price (2013), 196 pp
ISBN: 978-3-89336-921-8

Band / Volume 78
**Magnetoresistance and transport in carbon nanotube-based devices**
C. Morgan (2013), viii, 131 pp
ISBN: 978-3-89336-926-3

Band / Volume 79
**Development of a relativistic full-potential first-principles multiple scattering Green function method applied to complex magnetic textures of nano structures at surfaces**
D. Bauer (2014), 193 pp
ISBN: 978-3-89336-934-8

Band / Volume 80
**Identifizierung von artifiziellen Liganden eines in Nanodiscs inkorporierten integralen Membranproteins**
M. Pavlidou (2014), 106 pp
ISBN: 978-3-89336-942-3

Band / Volume 81
**Interdomain Functional Dynamics of Phosphoglycerate Kinase Studied by Single-Molecule FRET**
M. Gabba (2014), v, 179 pp
ISBN: 978-3-89336-943-0

Band / Volume 82
**Silizium Nanoribbon Feld-Effekt Transistoren zur Kopplung an elektroaktive Zellen**
M. Jansen (2014), xvi, 181 pp
ISBN: 978-3-89336-944-7

Band / Volume 83
**Microscopic description of the inverse Faraday effect at subpicosecond time scales**
D. Popova (2014), 183 pp
ISBN: 978-3-89336-962-1

Band / Volume 84
**Neutron Scattering**
Lectures of the JCNS Laboratory Course held at Forschungszentrum Jülich and at the Heinz Maier-Leibnitz Zentrum Garching
edited by Th. Brückel, G. Heger, D. Richter, G. Roth and R. Zorn (2014), ca. 360 pp
ISBN: 978-3-89336-965-2

Band / Volume 85
**Neutron Scattering**
Experiment Manuals of the JCNS Laboratory Course held at Forschungszentrum Jülich and at the Heinz Maier-Leibnitz Zentrum Garching
edited by Th. Brückel, G. Heger, D. Richter, G. Roth and R. Zorn (2014), ca. 195 pp
ISBN: 978-3-89336-966-9

Band / Volume 86
**Development and Characterization of a Microfluidic Magnetic Oscillation Reactor for Enzymes**
D. Jussen (2014), xx, 131 pp
ISBN: 978-3-89336-974-4

Weitere ***Schriften des Verlags im Forschungszentrum Jülich*** unter
http://wwwzb1.fz-juelich.de/verlagextern1/index.asp

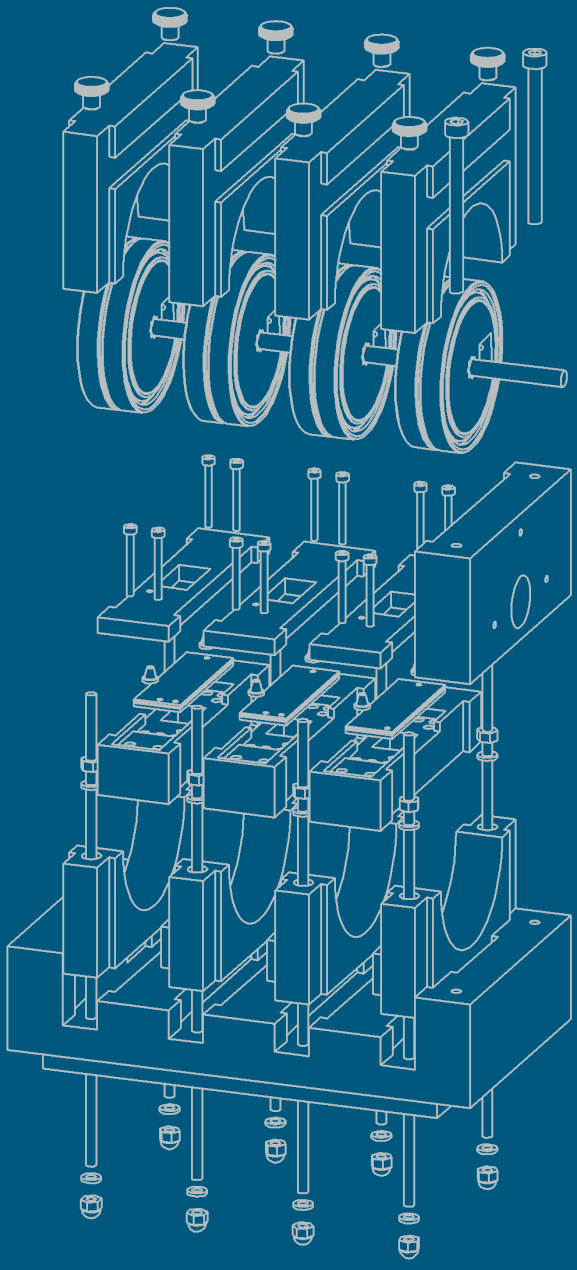

Schlüsseltechnologien / Key Technologies
Band / Volume 86
ISBN 978-3-89336-974-4

JÜLICH
FORSCHUNGSZENTRUM